Studies on Two Classes of Positive Electrode Materials for Lithium-Ion Batteries

by

James Douglas Wilcox

B.S. (Bates College) 2003
M.S. (University of California, Berkeley) 2006

A dissertation submitted in partial satisfaction of the

requirements for the degree of

Doctor of Philosophy

in

Engineering-Materials Science and Engineering

and the Designated Emphasis

in

Energy Science and Technology

in the

Graduate Division

of the

University of California, Berkeley

Committee in charge:

Professor Lutgard C. De Jonghe, Chair
Professor Oscar D. Dubon
Professor Nitash P. Balsara

Fall 2008

This dissertation of James Douglas Wilcox is approved:

Chair _____ Date _____

_____ Date _____

_____ Date _____

University of California, Berkeley

Fall 2008

Studies on Two Classes of Positive Electrode Materials for Lithium-Ion Batteries

by James Douglas Wilcox

Abstract

Studies on Two Classes of Positive Electrode Materials for Lithium-Ion Batteries

by

James Douglas Wilcox

Doctor of Philosophy in

Engineering-Materials Science and Engineering

and the Designated Emphasis

in

Energy Science and Technology

University of California, Berkeley

Professor Lutgard C. De Jonghe, Chair

The development of advanced lithium-ion batteries is key to the success of many technologies, and in particular, hybrid electric vehicles. In addition to finding materials with higher energy and power densities, improvements in other factors such as cost, toxicity, lifetime, and safety are also required. Lithium transition metal oxide and $LiFePO_4$/C composite materials offer several distinct advantages in achieving many of these goals and are the focus of this report.

Two series of layered lithium transition metal oxides, namely $LiNi_{1/3}Co_{1/3-y}M_yMn_{1/3}O_2$ (M=Al, Co, Fe, Ti) and $LiNi_{0.4}Co_{0.2-y}M_yMn_{0.4}O_2$ (M=Al, Co, Fe), have been synthesized. The effect of substitution on the crystal structure is related to shifts in transport properties and ultimately to the electrochemical performance. Partial aluminum substitution creates a high-rate positive electrode material capable of delivering twice the discharge capacity of unsubstituted materials. Iron substituted materials suffer from limited electrochemical performance and poor cycling stability due to the degradation of the layered structure. Titanium substitution creates a very high rate positive electrode

material due to a decrease in the anti-site defect concentration.

$LiFePO_4$ is a very promising electrode material but suffers from poor electronic and ionic conductivity. To overcome this, two new techniques have been developed to synthesize high performance $LiFePO_4$/C composite materials. The use of graphitization catalysts in conjunction with pyromellitic acid leads to a highly graphitic carbon coating on the surface of $LiFePO_4$ particles. Under the proper conditions, the room temperature electronic conductivity can be improved by nearly five orders of magnitude over untreated materials. Using Raman spectroscopy, the improvement in conductivity and rate performance of such materials has been related to the underlying structure of the carbon films. The combustion synthesis of $LiFePO_4$ materials allows for the formation of nanoscale active material particles with high-quality carbon coatings in a quick and inexpensive fashion. The carbon coating is formed during the initial combustion process at temperatures that exceed the thermal stability limit of $LiFePO_4$. The olivine structure is then formed after a brief calcination at lower temperatures in a controlled environment. The carbon coating produced in this manner has an improved graphitic character and results in superior electrochemical performance. The potential co-synthesis of conductive carbon entities, such as carbon nanotubes and fibers, is also briefly discussed.

_____

Professor Lutgard C. De Jonghe, Chair

This dissertation is dedicated to my family.

Table of Contents

List of Constants, Symbols, and Abbreviations

A_s	Surface area, cm^2 or m^2
a_i	Relative activity of species *i*
C_R	C-rate, h^{-1}
c_i	Concentration of species *i*, mol/L
D_i	Diffusion coefficient of species *i*, cm^2/s
d_{grain}	Grain size (nm)
E	Potential, V
E°	Standard state potential, V
E_{sp}	Specific energy density, Wh/kg
E_s	Stationary potential, V
E_v	Volumetric energy density, Wh/L
E_τ	Transient potential, V
F	Faraday's constant, 96,487 C/equivalent
G	Gibbs free energy, J
G°	Standard state Gibbs free energy, J
H	Magnetic field, Oe
I	Current, A
I	Interslab or lithium slab dimension, Å
i	Current density, A/cm^2
i°	Exchange current density, A/cm^2
M	Magnetization, emu/cm^3
M_B	Molecular weight of active material, g/mol
M_i	Molecular weight of species *i*, g/mol
m	Transition metal valance
m_i	Mass of species *i*, g
m_B	Mass of active material, g
N_i	Flux density of species *i*, mol/cm^2 s
n	Number of electrons transferred
n_i	Moles of species *i*
P	Pressure, atm
P_s	Specific power density, W/kg
P_v	Volumetric power density, W/L
Q	Charge, C
Q_c	Charge capacity, Ah
q	Heat transferred, J
q_{th}	Theoretical specific capacity, Ah/kg
R	Universal gas constant, J/mol K
R_B	Bragg factor

R_c	Critical separation distance, Å
S	Entropy, J/K
S	Slab dimension, Å
s	Effective spin
s_i	Stoichiometric coefficient of species *i*
T	Absolute temperature, K
t	Time, s
U	Internal energy, J
V	Voltage, V
V	Volume, cm^3
V_s	Volume of system, L
v	Fluid velocity, cm/s
w	Work, J
W_s	Mass of system, kg
Z	Atomic number
z_i	Charge number of species *i*
α_a,α_c	Anodic and cathodic transfer coefficients
γ	Surface energy, J/m^2
Γ_i	Activity coefficient independent of electrical state of species *i*
δ_{gb}	Grain boundary thickness (nm)
η_s	Surface overpotential, V
λ_i^θ	Property consistent with secondary reference state, kg/mol
μ_i	Chemical potential of species *i*, J/mol
$\tilde{\mu}_i$	Electrochemical potential of species *i*, J/mol
$\tilde{\mu}_i^\circ$	Electrochemical potential of species *i* in the standard state, J/mol
σ_{bulk}	Bulk conductivity (S/cm)
$\sigma_{gb}^{\parallel}$	Parallel grain boundary conductivity (S/cm)
$\sigma_{gb}^{\perp}$	Perpendicular grain boundary conductivity (S/cm)
σ_m	Composite conductivity (S/cm)
τ	Step time, s
Φ	Electrostatic potential, V

Acknowledgments

I would like acknowledge and extend my heartfelt appreciation to my advisor, Lutgard De Jonghe, for giving me the opportunity to come to Berkeley and pursue my interests in alternative energy technology. I also would like to express the deepest gratitude to my 'other' advisor, Marca Doeff, for her never ending patience and support. In particular, I've appreciated her willingness to let me find my own path through this work with the aid of her timely guidance and encouragement.

I have benefited tremendously from the numerous discussions with scientists, staff, post-docs, and graduate students at both UC Berkeley and Lawrence Berkeley National Laboratory. In particular, the interactions with Sébastien Patoux, Juliete Saint, Charles Delacourt, Venkat Srinivasan, and James Wu have been both constructive and memorable. I would like to thank Alex Farrell for reminding me that the impact and value of science extends well beyond the lab. I owe a debt of gratitude to all of my collaborators on this work, Robert Kostecki, Marek Marcinek, Heike Gabrisch, and Efrain Rodriguez, for sharing their knowledge and time with me. Special thanks to my undergraduate assistant, Albert Aumentado, for making me constantly rethink concepts that I thought I already understood.

I would like to thank Jason Nicholas, Daan Hein Alsem, Becca Jones, Paul Albertus, Aaron Kueck, and Gabe Harley for their friendship, my time at Cal would not have been what it was without it.

I will forever be indebted to my family for their endless support in all of my endeavors. I'm keenly aware and appreciative of the sacrifices they've made to allow me the opportunities I've enjoyed. In particular, I would like to thank my wife, Kari, whose smile will always provide me with infinite comfort and inspiration.

Funding for this work was provided by the Assistant Secretary for Energy Efficiency and Renewable Energy, Office of Vehicle Technologies of the U.S. Department of Energy under Contract No. DE-AC02-05CH11231. This work benefited from the use of the Lujan Center at the Los Alamos Neutron Science Center, funded by the DOE Office of Basic Energy Sciences and Los Alamos National Laboratory funded by the Department of Energy under contract W-7405-ENG-36. Additionally, part of this work was made possible through the use of the National Center for Electron Microscopy at Lawrence Berkeley National Laboratory.

1. Introduction

1.1 Motivation: Why Hybrid Electric Vehicles?

Over the past twenty years there has been growing concern over the potential impact of human activities on the global ecosystem. Recently, the Intergovernmental Panel on Climate Change (IPCC) concluded that the evidence for global warming is unequivocal and stated with "very high confidence" that the most likely source is increases in anthropogenic green house gas concentrations.[1] Therefore, confronting the underlying causes of global warming in the context of a burgeoning world population and expected economic growth must be a central focus of global leaders in the immediate future if a climate disaster is to be mitigated.

Historically, global climate conditions have changed periodically in response to the prevailing atmospheric conditions. By analyzing the oxygen isotopic composition of Antarctic ice cores as a function of depth, a record of average surface temperature has been created covering the last 800,000 years.[2, 3] The concurrent analysis of carbon dioxide (CO_2) and methane (CH_4) trapped in voids in the ice cores has established a direct correlation between increased average surface temperature and elevated greenhouse gas (GHG) concentrations. Of primary concern is the abrupt increase in CO_2 concentrations observed over the last century. While the average atmospheric CO_2 concentration in pre-industrial times oscillated below 280 ppm, present day concentrations are approaching 380 ppm, a level unprecedented in the historical record. Similar trends have been established for methane and nitrous oxide concentrations.[1] These recent trends have been associated with an increase in average global temperature of 0.74° C in the time frame of 1906-2005.[4] While the exact impact of such atmospheric changes in terms of ultimate temperature shifts remains unclear, a change in global weather patterns has already been observed. These include, but are not limited to, increases in sea level, the frequency of heat waves, intense cyclone activity, decreases in snow and ice coverage, as well as shifts

in precipitation patterns.[1] It is important to remember that the rate of GHG accumulation in the atmosphere is accelerating, adding increased pressure to numerous ecosystems already at risk.[5]

The main source of CO_2 emissions over the last two centuries has been the use of fossil fuels for energy, transportation, and industry.[1, 6] In 2004 alone, the United States emitted an estimated 1,617 megatons of carbon, 22 percent of the total global carbon emissions.[7] United States CO_2 emissions are roughly divided by thirds, with one third derived from transportation (20 percent from highway fuel consumption), and the remaining two thirds from industry and energy generation.[8] Therefore, eliminating GHG emissions from any one sector will not solve the problem alone. Instead, improvements in all forms of material, land, and energy use must be pursued if the United States is to seriously reduce its emissions of GHG's.

Further complicating the use of fossil fuels in the United States, in particular oil, is the political and economic implications of importing such massive amounts of resources. The United States is by far the world's largest consumer of oil, consuming 20.6 million barrels of oil a day in 2007 of which 58 percent was imported (44 percent being imported from the Organization of the Petroleum Exporting Countries (OPEC) alone).[9] When broken down into its end-use sectors, transportation accounted for 69 percent of petroleum use in the United States, 43 percent derived from motor vehicles.[9]

The simplest means by which to lower oil consumption and GHG emissions in the short term is to develop technologies that allow for the use of such resources more efficiently. One key step in this process has been achieved with the recent commercialization of hybrid electric vehicles (HEV's). Due to the success of these vehicles there has been a strong push to extend the technology to plug-in hybrid electric vehicles (PHEV's) and revisit electric vehicles (EV's). Both of these technologies would allow for at least a portion of vehicle miles to be powered by electricity alone, displacing energy consumption to the electric grid. When one considers the fact that the average daily commute distance (one way) in

the United States is approximately 28-30 miles (with 50 percent of trips below 20 miles), the potential impact of PHEV technology becomes apparent.[10-12] A recent study by the Pacific Northwest National Laboratory (PNNL) has concluded that there is enough excess capacity in the national electric grid to power 73 percent of the light duty vehicles in the United States (of which there are 217 million) with a daily commute of 33 miles.[12] This equates to a drop in gasoline use of 6.5 million barrels per day, or roughly 52 percent of all petroleum imports. Understandably, the impact on emissions of PHEV's is dependent on the regional power mix in which the PHEV is deployed. This is an important aspect for policy makers to consider in the future, but historically such point source emitters have been easier to regulate than dispersed sources.

Furthermore, such technologies must be deployed in the market place with the proper policies and oversight if they are to succeed in lowering GHG emissions and oil consumption. For example, under the present conditions the improvements in gas mileage of hybrid electric vehicles may lead to an increase in total miles driven, negating the potential benefits. It is also important to understand that the environmental and energy issues facing the global community at the present time will not be solved by any single technology. Instead, a plethora of solutions will be required if the transformation to cleaner, carbon-neutral energy sources is to be accomplished on a time scale sufficient to avoid catastrophic climate change.

1.2 Battery Fundamentals

1.2.1 Thermodynamics

By definition, a battery is a device that converts the chemical energy stored in its active materials into electrical energy through a combination of electrochemical oxidation and reduction (redox) reactions. In contrast to a corrosion reaction, the redox reactions are physically separated so as to allow useful work to be extracted from the system. During

discharge oxidation occurs at the anode (negative electrode) and reduction is located at the cathode (positive electrode). Separating the positive and negative electrodes is an electrolyte through which only ions may pass, forcing the accompanying electrons through the external circuit before recombining in the positive electrode during discharge.

The redox reactions undertaken during battery operation can be highly varied in nature depending on both the active materials being utilized and the conditions under which the cell is being operated. In general, all electrochemical reactions can be broken down into separate oxidation and reduction reactions and represented as shown in Equations 1.1-3, where *n* denotes the number of electrons transferred during the reaction.

$$aA + ne^- \leftrightarrow cC \qquad \text{Reduction} \qquad \text{Eq. 1.1}$$

$$bB - ne^- \leftrightarrow dD \qquad \text{Oxidation} \qquad \text{Eq. 1.2}$$

$$\mathrm{aA} + \mathrm{bB} \leftrightarrow cC + dD \qquad \text{Overall} \qquad \text{Eq. 1.3}$$

From the first law of thermodynamics, we can relate the change in the internal energy of a system, *dU*, to the heat added to the system, *q*, and the work done by the system, *w* (Equation 1.4).[13] The work term can be further broken down into the various types of work performed by or on the system such as magnetic, surface, pressure/volume,

$$dU = \delta q - \delta w \qquad \text{Eq. 1.4}$$

chemical, and electrical work (Equation 1.5). Under most conditions the only work that is of interest is that of electrical work, EdQ. The amount of charge, *Q*, can be expressed in terms of the charge number, z_i, Faraday's constant F (96487 C) and n_i, the

$$\delta w = HdM + \gamma dA_s + PdV + \sum_{i=1}^{N} \mu_i dn_i + EdQ \qquad \text{Eq. 1.5}$$

number of charged species *i* as shown in Equation 1.6. Using the second law of thermodynamics, relating the heat exchanged to the entropy for a reversible process

(Equation 1.7), combining equations 1.4-7, and ignoring all work terms not associated

$$dQ = z_i F dn_i \qquad \text{Eq. 1.6}$$

with electrical or pressure/volume work, we can derive Equation 1.8 describing the internal energy, *U*.

$$\delta q = TdS \qquad \text{Eq. 1.7}$$

$$dU = TdS - PdV - z_i FEdn_i \qquad \text{Eq. 1.8}$$

When operating under constant temperature and pressure conditions, the proper thermodynamic state variable is the Gibbs energy, G (Equation 1.9). Taking the

$$G = U - TS + PV \qquad \text{Eq. 1.9}$$

complete differential of Equation 1.9, combining with Equation 1.8, and assuming a closed system, the change in Gibbs free energy can be related to the negative of the electrical work performed by the system (Equation 1.10). Integration reveals that the maximum electrical work obtained from a closed system operating isobarically and

$$dG = VdP - SdT - z_i FEdn_i \qquad \text{Eq. 1.10}$$

isothermally is related to the change in Gibbs free energy of the system (Equation 1.11). The superscript signifies that the reaction was undertaken in the standard state and E° is the equilibrium potential difference between the two electrodes.

$$\Delta G^\circ = -nFE^\circ \qquad \text{Eq. 1.11}$$

The potential that is measured in Equation 1.11 is the difference in the electrochemical potential of electrons in equilibrium with both the reactant and product phases. The electrochemical potential, $\tilde{\mu}_i$, is defined by Equation 1.12, and is utilized due to the fact that we are referring to the equilibration of charged species.

The electrochemical potential is dependent on temperature, pressure, composition, and electrical state and is often arbitrarily broken down into chemical and electrostatic contributions (Equation 1.13).[14] It in this context, the activity coefficient, Γ_i, must be

$$\tilde{\mu}_i = \tilde{\mu}_i^\circ + RT \ln a_i \qquad \text{Eq. 1.12}$$

$$\tilde{\mu}_i = \mu_i + z_i F\Phi = RT \ln \lambda_i^\theta m_i \Gamma_i + z_i F\Phi \qquad \text{Eq. 1.13}$$

defined such that it is independent of the electrical state of the system. It is important to note, that depending on how Γ_i and Φ are established, the breakdown of the electrochemical potential may have no physical meaning.

For reactions taking place under non-standard state conditions changes in the chemical activity, a_i, must be accounted for. The observed potential can be calculated by combining Equations 1.1, 1.12 and the fact the change in the Gibbs free energy corresponds to the difference in electrochemical potential of reactants and products. Equation 1.14, known as the Nernst equation, results where R is the ideal gas constant, T is the absolute temperature, and s_i is the stoichiometric coefficient of species i.

$$E = E^\circ - \frac{RT}{nF} \ln \prod_i a_i^{s_i} \qquad \text{Eq. 1.14}$$

1.2.2 Kinetics and Transport

Thus far our discussion has been limited to cells in equilibrium in which there is no net flow of current. As soon as a current comes to pass, whether in a galvanic or electrolytic cell, losses begin to build up in the cell. These losses are often expressed in the form of a departure from the equilibrium potential and are termed overpotentials. Overpotential losses arise due to both kinetic limitations at the electrode interfaces and the transport of reactants in both the electrolyte and electrode phases.

For any reaction, whether chemical or electrochemical, there is an activation energy that must be overcome for the reaction to proceed. In electrochemical systems

the reaction rate, as measured by the current density, depends on numerous parameters including the electrode surface chemistry, electrolyte composition at the boundary, and the potential of the electrode. The Butler-Volmer equation (Equation 1.15) relates the observed current density to the independent oxidation and reduction reaction rates as

$$i = i_0\left[\exp\left(\frac{\alpha_a F\eta_s}{RT}\right) - \exp\left(\frac{-\alpha_c F\eta_s}{RT}\right)\right] \qquad \text{Eq. 1.15}$$

determined by the surface overpotential, η_s. The exchange current density, i_0, is a measure of the inherent kinetics of a system. The transfer coefficients, α_a and α_c, are indicative of how the applied potential partitions between the anodic and cathodic reactions.

In addition to the surface overpotential to drive the reaction, ions and electrons must be transported to (and/or away from) the reaction zone at the interface between electrode and electrolyte. Mass transport through the electrolyte can be described by a combination of species motion due to migration, diffusion, and convection (Equation 1.16). The flux density of a charged species in response to an electric field is

$$N_i = -z_i u_i F c_i \nabla\Phi - D_i \nabla c_i + c_i v \qquad \text{Eq. 1.16}$$

defined by the conductivity and is proportional to the charge number, z_i, concentration, c_i, and mobility, u_i. During the operation of a cell, concentration gradients, ∇c_i, may develop and species will diffuse according to Fick's first law of diffusion at steady state. Finally, bulk solvent motion with velocity, v, can equilibrate concentration profiles across a cell and deliver reactants to the electrode.

If the cell is operated such that one of the reactants becomes depleted at the electrode/electrolyte interface, the transport of that species may become rate limiting. The difference in concentration between the electrode surface and the bulk electrolyte combined with any diffusion potentials gives rise to concentration overpotentials. It is important to note that the removal of species from the electrode surface through solid

state diffusion can also represent a concentration overpotential. Given the fact that the conductivities of many electrolytes are 3-5 orders of magnitude greater than in the solid state, these effects can become limiting in some systems.

1.3 Battery Performance Metrics

Depending on the application, it is generally desirable for a battery to have a high energy capacity and to deliver the greatest amount of power per unit mass or volume. Practically, this is achieved by finding materials capable of storing large amounts of charge at high potentials with favorable kinetic and transport characteristics. These requirements are extremely important for the emerging vehicular applications where factors such as driving range and acceleration are directly impacted by the amount of charge stored in a battery and the rate at which it can be extracted.

The theoretical charge capacity of a battery, Q_c (Ah), is given by Faraday's Law (Equation 1.17). Faraday's Law relates the mass of species i, m_i, produced during a reaction to the molecular weight, M_i, the number of electrons transferred, n, Faraday's constant,

$$Q_c = \int_{t_1}^{t_2} I(t)dt = \frac{m_i nF}{s_i M_i} \qquad \text{Eq. 1.17}$$

and the stoichiometric coefficient of species i, s_i, to the current passed during the reaction, I, and the time of the reaction, t.[14] The theoretical specific capacity, q_{th} (Ah/kg), is the amount of charge stored per unit mass of reactants (Equation 1.18). The theoretical specific capacity is determined by the maximum number of electrons transferred during the reaction and the molecular weight of the reactants. By convention the specific capacity is generally reported in units of mAh/g, with one mAh equivalent to 3.6 Coulombs of charge.

$$q_{th} = \frac{nF}{\sum_i m_i} \ (C/kg) = \frac{26.8n}{M_i} \ (Ah/kg) \qquad \text{Eq. 1.18}$$

For a battery operating under constant current conditions the energy stored per unit mass is given by the specific energy, E_s (Wh/kg) (Equation 1.19).

$$E_s = \frac{\int_0^{t_{Cutoff}} V(t)Idt}{3600W_S}(Wh/kg) \qquad \text{Eq. 1.19}$$

Alternatively, the energy stored per unit volume is given by the volumetric energy density E_v (Wh/L) (Equation 1.20).

$$E_v = \frac{\int_0^{t_{Cutoff}} V(t)Idt}{3600V_S}(Wh/L) \qquad \text{Eq. 1.20}$$

The average amount of power a battery is capable of delivering per unit mass is termed the specific power density, P_s (W/kg) (Equation 1.21, written for constant current operation).

$$P_s = \frac{\int_0^{t_{Cutoff}} V(t)Idt}{W_S \int_0^{t_{Cutoff}} dt}(W/kg) \qquad \text{Eq. 1.21}$$

The average volumetric power density, $P_{v,}$ (W/L) is the average amount of power a battery is capable of delivering per unit volume (Equation 1.22, written for constant current operation).

$$P_v = \frac{\int_0^{t_{Cutoff}} V(t)Idt}{V_S \int_0^{t_{Cutoff}} dt}(W/L) \qquad 1.22$$

Owing to variations in electrode parameters such as active material loading, electrode composition, thickness, and porosity, the rate at which a battery is operated is often defined in terms of a C-rate (C_R) (Equation 1.23).[15] The C-rate methodology

$$I = C_R \, x \, Q_c \qquad \text{Eq. 1.23}$$

normalizes the charge or discharge current, expressed in amperes, as a fraction or multiple of the rated capacity. For example, a 1C rate fully charges or discharges a cells capacity in one hour while a C/25 rate takes 25 hours.

1.4 Lithium Ion Batteries

Lithium battery technology has developed tremendously over the last twenty years, enabling the commercialization of whole new sectors of portable technology.[16] Owing to the high electronegativity and low molecular weight of lithium (6.94 g/mol), lithium batteries have been developed with energy and power densities that vastly outperform lead acid, nickel-cadmium, and nickel metal hydride based systems. However, concerns over the safety characteristics as well as limited cycle life and high costs have limited the use of lithium ion batteries to relatively small applications.

Modern rechargeable lithium ion batteries, first introduced by Sony in 1990, are based on transition metal oxide positive electrodes (e.g. $LiCoO_2$) paired with a graphitic carbon negative electrode (Li_xC) (Equations 1.24-26).[17, 18] Upon charge, lithium ions and electrons are removed from the lattice of the positive electrode creating an electron hole and lithium vacancy. The lithium ions are transported through the electrolyte to the anode where they are incorporated into the interlayer space of the graphite sheets. At

Negative Electrode Reaction:	$Li_xC \leftrightarrow xLi^+ + xe^- + C$	Eq, 1.24
Positive Electrode Reaction:	$MO_2 + xLi^+ + xe^- \leftrightarrow Li_xMO_2$	Eq. 1.25
Overall Reaction:	$Li_xC + MO_2 \leftrightarrow C + Li_xMO_2$	Eq. 1.26

the same time, electrons pass through the external circuit where they can perform useful work before being simultaneously incorporated into the anode lattice with the lithium ions from the electrolyte. During charge, the lithium and electron pathway is reversed and these cells are often termed "rocking chair" batteries as lithium ions are simply shuttled between the positive and negative electrode during operation (Figure 1.1).

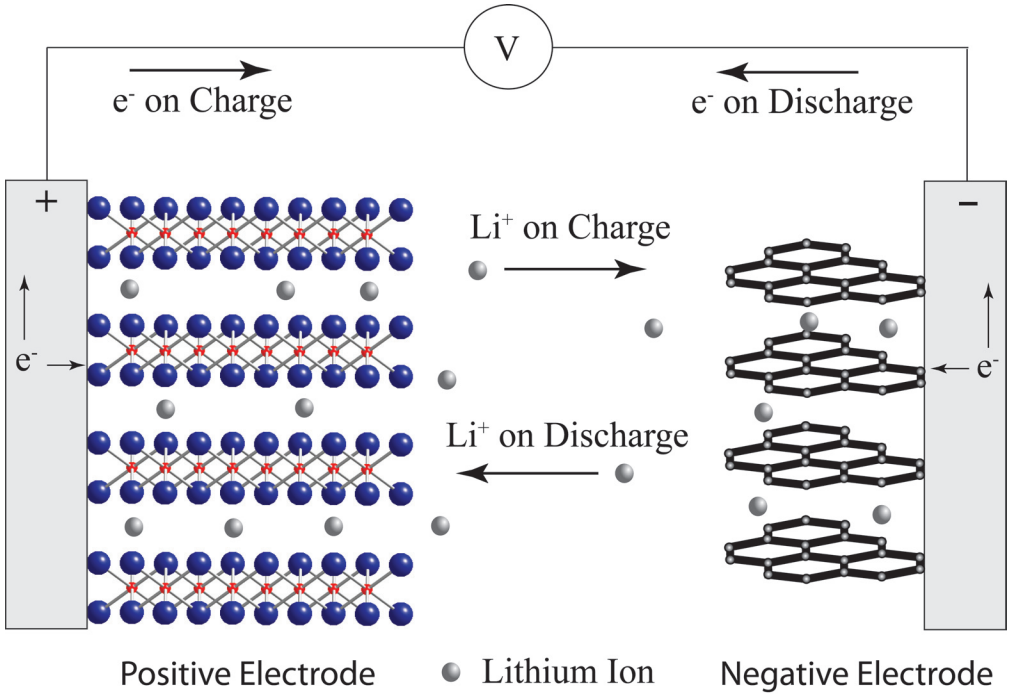

Figure 1.1: Schematic diagram of a lithium-ion or "rocking chair" battery in which lithium ions are shuttled between two intercalation electrode materials during operation.

Positive electrode development in particular has been limited over the last twenty years. $LiCoO_2$ continues to be the dominant positive electrode material in commercial cells even though its practical capacity (~140 mAh/g) is limited to half of its theoretical capacity (280 mAh/g) due to safety and lifetime issues. Novel oxide and phosphate materials are slowly coming to market and promise to improve the performance and safety of lithium ion batteries substantially, but problems such as high cost and low energy density persist.

1.5 Batteries for Vehicular Applications:

While the exact battery specifications for HEV, PHEV, and EV applications will vary depending on the duty cycle and the balance of systems, all require battery packs with high energy and power densities on both a specific and volumetric basis. In an effort to better define the requirements for these emerging technologies, the Department of Energy (DOE) through the United States Advanced Battery Consortium (USABC) has developed a set of battery specific goals for end of life battery performance.[19] The goals for HEV's, PHEV's, and EV's are presented in Table 1.1. While no known battery technology can come close to achieving the energy density of gasoline (~12,000 Wh/kg), lithium battery technologies already exceed the DOE goals for energy and power density for HEV and PHEV applications.

Table 1.1: USABC end-of-life battery goals by vehicular application.

Criteria	Units	HEV[a]	PHEV(10)[b]	PHEV(40)[b]	EV[a]
Pulse Power	W	2,500	4,500	3,800	Not Stated
Specific Power Density	W/kg	62.5	75	31.7	300
Volumetric Power Density	W/l	78.1	112.5	47.5	460
Energy	Wh	300	3,400 (CD)[c] 500 (CS)[d]	11,600 (CD)[c] 300 (CS)[d]	4,000
Specific Energy Density	Wh/kg	7.5	57 (CD)[c] 8.3 (CS)[d]	97 (CD)[c] 2.5 (CS)[d]	150
Volumetric Energy Density	Wh/l	9.4	85 (CD)[c] 12.5 (CS)[d]	145 (CD)[c] 3.75 (CS)[d]	230
Cycle Life	Cycles	300,000	5,000 (CD)[c] 300,000 (CS)[d]	5,000 (CD)[c] 300,000 (CS)[d]	1,000
Calendar Life	Years	15	15	15	10
Temperature Range	°C	-30 to 52	-46 to 66	-46 to 66	-40 to 50
Price	$	500	1,700	3,400	<6,000

[a]Values reflect minimum value for commercialization.
[b]PHEV(10) and PHEV(40) refer to a PHEV with an all electric range of 10 and 40 miles respectively.
[c]CD refers to a PHEV operating under charge depleting conditions.
[d]CS refers to a PHEV operating under charge sustaining conditions.

1.6 Scope

This dissertation focuses on the discovery of novel materials and processing techniques that will enable the future generation of high energy, high power positive electrode materials. The dissertation can loosely be divided into two sections based on the materials being studied, i.e., layered transition metal oxides and transition metal phosphates. The first section describes the synthesis and characterization of several novel layered transition metal oxide compounds. Shifts in electrochemical performance are explained on the basis of changes in the underlying crystal structure and the related transport processes induced upon selected substitution. The second section focuses on the synthesis of lithium transition metal phosphate positive electrode materials with a high quality carbon coating. Two unique methods of creating carbon coatings with a highly graphitic, and therefore, highly conductive nature are described. The characterization of both the active material and carbon coating is presented and related to the ultimate electrochemical performance. In both sections, the relevant literature is outlined so as to give a greater context to work described herein.

1.7 References

1. IPCC, *Climate Change 2007: Synthesis Report*. 2007.

2. Lambert, F., et al., *Dust-climate couplings over the past 800,000 years from the EPICA Dome C ice core.* Nature, 2008. **452**(7187): p. 616-619.

3. Petit, J.R., et al., *Climate and atmospheric history of the past 420,000 years from the Vostok ice core, Antarctica.* Nature, 1999. **399**(6735): p. 429-436.

4. IPCC, *Climate Change 2007: Synthesis Report, Summary for Policymakers*. 2007.

5. Canadell, J.G., et al., *Contributions to accelerating atmospheric CO(2) growth from economic activity, carbon intensity, and efficiency of natural sinks.* Proceedings of the National Academy of Sciences of the United States of America, 2007. **104**: p. 18866-18870.

6. IPCC, *Historical Overview of Climate Change Science*. 2007.

7. Raupach, M.R., et al., *Global and regional drivers of accelerating CO(2) emissions.* Proceedings of the National Academy of Sciences of the United States of America, 2007. **104**(24): p. 10288-10293.

8. Gallagher, K.S., et al., *Policy Options for Reducing Oil Consumption and Greenhouse-Gas Emissions from the U.S. Transportation Sector*. 2007, Energy Technology Innovation Policy research group, Belfer Center for Science and International Affairs: Cambridge, Mass.

9. *Monthly Energy Review*. 2008, EIA/DOE.

10. Vyas, A., et al., *Plug-In Hybrid Electric Vehicles: How Does One Determine Their Potential for Reducing U.S. Oil Dependence?*, in *Electric Vehicle Symposium-23*. 2007: Anaheim, CA.

11. Gaines, L., et al., *Sorting Through the Many Total-Energy-Cycle Pathways Possible with Early Plug-In Hybrids*, in *Electric Vehicle Symposium-23*. 2007: Anaheim, CA.

12. Kintner-Meyer, M., K. Schneider, and R. Pratt, *Impacts Assessment of Plug-In Hybrid Vehicles on Electric Utilities and Regional U.S. Power Grids. Part 1: Technical Analysis*. 2006, Pacific Northwest National Laboratory.

13. Prentice, G., *Electrochemical Engineering Principles*. Prentice Hall International Series in the Physical and Chemical Engineering Sciences. 1991, Englewood Cliffs, N.J.: Prentice-Hall.

14. Newman, J. and K. Thomas-Alyea, *Electrochemical Systems*. 2004, Hoboken, NJ: John Wiley & Sons, Inc.

15. Linden, D., *Handbook of Batteries*. 2nd ed. 1995, New York: McGraw-Hill Inc.

16. Tarascon, J.M. and M. Armand, *Issues and challenges facing rechargeable lithium batteries.* Nature, 2001. **414**(6861): p. 359-367.

17. Nagaura, T., *Development of rechargeable lithium batteries, I. Lithium manganese oxide rechargeable batteries.* Progress in Batteries & Battery Materials, 1991. **10**: p. 209-217.

18. Nagaura, T., *Development of rechargeable lithium batteries, II. Lithium ion rechargeable batteries.* Progress in Batteries & Battery Materials, 1991. **10**: p. 218-226.

19. United States Council for Automotive Research. *US Advanced Battery Consortium (USABC)*. [cited November 2008]; Available from: http://www.uscar.org/guest/view_team.php?teams_id=12.

2. Physical Properties of Layered Lithium Transition Metal Oxides

2.1 Abstract

This chapter is included as a basic introduction to the layered oxide positive electrode materials used in lithium battery applications. Due to the massive amount of published work on these materials it is by no means complete and is only meant to highlight the pertinent areas for the substitution work described in later chapters. For more in-depth information on any particular material, the review articles by Whittingham[1] and Ohzuku[2] are recommended as starting locations.

2.2 Introduction

Layered oxide materials have represented the state of the art positive electrode materials for high-energy lithium ion batteries for nearly two decades.[5, 6] Building on breakthroughs pioneered by Whitingham in the 1970's on layered chalcogenides,[9-12] the prototypical layered oxide material, $LiCoO_2$, was first introduced in 1980 by the Goodenough group.[13, 14] The initial work on the chalcogenide systems led to an increased understanding of intercalation electrodes operating under topotactic conditions that would provide the basis for future battery active materials. In contrast to electrodes based on soluble electrodes or disproportionation reactions, topotactic intercalation reactions occur with a minimal rearrangement of the host lattice.[8, 15] These reactions, therefore, avoid the energetic losses associated with the nucleation and growth of product phases or significant structural rearrangement.[1, 4] As only minimal numbers of bonds are broken and reformed, electrodes of a highly reversible and stable nature can be created.

Commercial lithium ion batteries based on $LiCoO_2$ cathode materials have obtained unprecedented energy densities compared to the previous generation nickel-cadmium (Ni-Cd) and nickel metal hydride (Ni-MH) chemistries. However, only approximately half

(~140 mAh/g) of the theoretical capacity (280 mAh/g) of the cathode material can be used reversibly. When cycled to lithium contents below $x \leq 0.5$ in Li_xCoO_2, several phase changes can occur, degrading the crystal structure and strongly impacting the lifetime and abuse tolerance of such cathodes.[16] These limitations, coupled with the high cost and toxicity of cobalt, have driven battery researchers to search for new materials that combine both improved safety factors and electrochemical performance.

2.3 Crystal Structure of the Layered Oxides

Materials of the composition, AMO_2, where A is an alkali metal and M is typically a transition metal cation in the 3+ oxidation state, are known to crystallize into a variety of structural polytypes. These include, but are not limited to, α-$NaFeO_2$, γ-$NaFeO_2$, α-$LiFeO_2$, β-$LiFeO_2$, γ-$LiFeO_2$, orthorhombic $LiMnO_2$, and the spinel related low temperature (LT)-$LiCoO_2$.[4, 7] Almost all of the polytypes are based on a cubic close packed (fcc) or nearly close packed array of anions in which the cations are dispersed in the octahedral and tetrahedral vacancies of the anion lattice. Of particular interest for lithium batteries is the α-$NaFeO_2$ structure (space group $R\bar{3}m$) (Figure 2.1) that is characteristic of both $LiCoO_2$ and $LiTiS_2$.[1, 12] The structure is comprised of layers of edge sharing, octahedrally coordinated transition metals with alternating planes of lithium ions residing in the Van der Waals gaps between transition metal layers. The structure is a rock salt (NaCl) derivative with lithium and transition metal ions occupying alternating (111) planes normal to one of the cubic $\langle 111 \rangle$ directions. In order to function as a reversible cathode material at least some of the transition metal ions must be electrochemically active. The unit cell consists of three alternating layers of lithium and transition metals and is often described as O3 using the Delmas nomenclature.[17]

From inspection of the α-$NaFeO_2$ structure, it is possible to define two structural parameters that are of key importance when discussing the electrochemical activity of such materials (Figure 2.2). The first is often termed "slab" thickness, (*S*) (Equation 2.1),

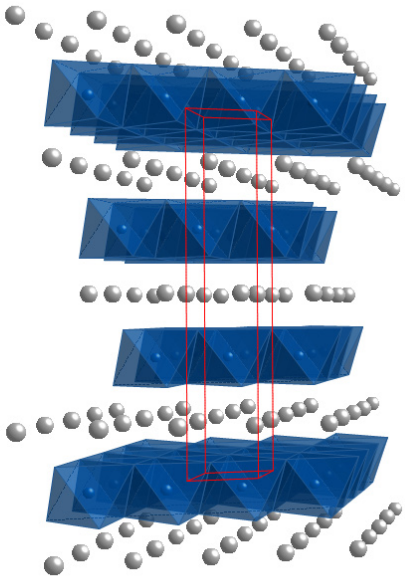

Figure 2.1: The α-$NaFeO_2$ (O3, space group $R\bar{3}m$) structure of the layered oxide cathode materials. Lithium (gray) and transition metal atoms (blue) are in stacked in edge sharing octahedral sheets. Oxygen atoms have been omitted for clarity.

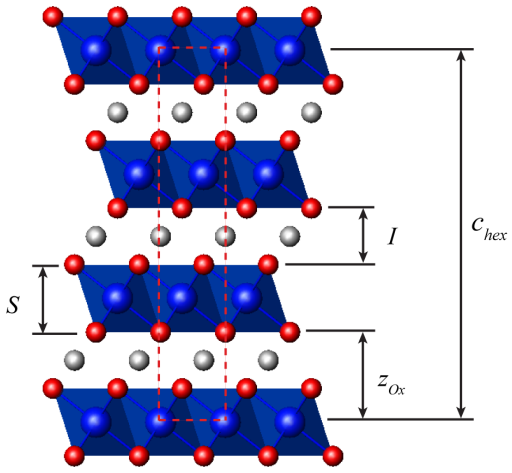

Figure 2.2: Definition of the transition metal "slab" (*S*) and lithium (*I*) "interslab" dimensions in terms of refineable crystallographic quantities c_{hex} and z_{Ox}. Unit cell axis is shown as a dashed line.

and is a measure of the distance between oxygen layers bound to the transition metal centers. The "interslab" or "lithium slab" dimension, (*I*), is the equivalent measure of the distance between oxygen layers astride the lithium plane (Equation 2.2). Equations 2.1 and 2.2 are written for a system indexed with transition metal ions located in the *3a* position at (0,0,0), lithium ions in the *3b* position at (0,0,½), and oxygen ions in the *6c* position at (0,0,z_{Ox}).

$$S = 2\left(\frac{1}{3} - z_{Ox}\right)c_{hex} \qquad \text{Eq. 2.1}$$

$$I = \frac{c_{hex}}{3} - S \qquad \text{Eq. 2.2}$$

2.4 Lithium Transport in Layered Oxides

One of the key advantages to the layered oxide positive electrode materials is the rapid transport of both electrons and lithium ions through the host lattice. For example, the chemical diffusion coefficient of lithium in Li_xCoO_2 has been reported to be $10^{-11.6}$ cm^2/s at x=1 and can increase by almost two orders of magnitude at intermediate lithium concentrations.[18] Electronic conductivity in the same system has been measured to be as high as $\sim 10^{-3}$ S/cm at x=1 with an insulator to metallic transition occurring at lower lithium contents.[19-22]

In the O3 structure lithium transport is limited to the two dimensional lithium plane and is most likely accomplished via a hopping mechanism through adjacent tetrahedral vacancies (Figure 2.3).[23, 24] First principle calculations indicate that the motion of lithium is moderated by the presence of a di-vacancy on the lithium lattice and is therefore highly concentration dependent.[25] Further calculations reveal that the highest activation energy can be closely approximated by a lithium ion residing within the tetrahedral vacancy.[26] A lithium ion residing within the tetrahedral site is found to be under slight compression relative to the fully relaxed structure and is face sharing with the adjacent transition metal

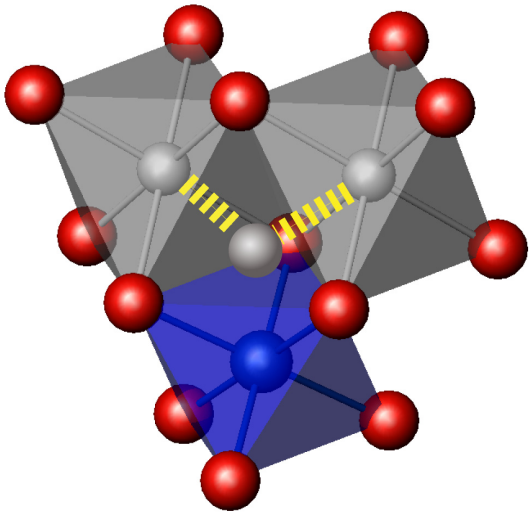

Figure 2.3: Lithium diffusion pathway (yellow) through adjacent tetrahedral vacancies located between transition metal (blue) and lithium (gray) octahedra. The hop is energetically most favorable when accompanied by an associated di-vacancy (not shown).

ion. Both of these factors serve to raise the activation energy for lithium transport to over 400 meV at small lithium slab dimensions in both $LiCoO_2$ and $LiNiO_2$ (Figure 2.4).[26] Increasing the lithium slab dimension lowers the activation energy by both decreasing the site compression and allowing a lithium ion residing in the activated state to shift away from the associated transition metal, decreasing the electrostatic interaction. As an example of how sensitive lithium diffusion is to the activation energy in these materials, it has been calculated that a decrease of only 57 meV may increase lithium diffusion by as much as an order of magnitude.[27] Alternatively, it has been suggested that the incorporation of a percolating network of low valence transition metal ions may allow for a substantial decrease in activation energy.[26] While this may be true, it is important to note that the oxidation state of a low valence transition metal will have to increase as the battery is charged. This mitigates the impact of such a pathway, although it may be compensated in part by an increase in the lithium slab dimension at low lithium contents.

Therefore, to create layered oxide cathode materials with superior lithium

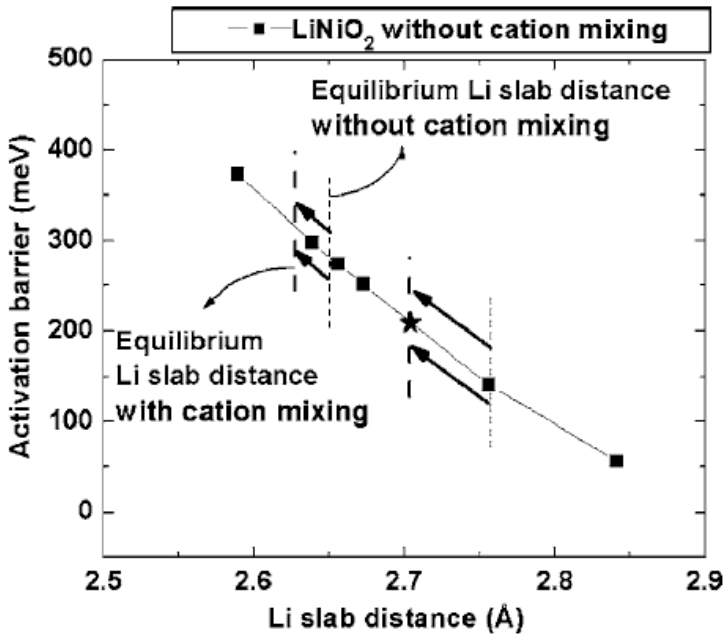

Figure 2.4: The calculated activation energy for lithium migration in $LiNiO_2$ with (stars) and without (squares) ion mixing. The impact of anti-site mixing is particularly strong in the partially delithiated state where it inhibits the expansion of the lithium slab dimension due to the increased bond strength across the slab. Plot from Ref. (26).

transport properties, it is of vital importance to synthesize materials with optimal lithium slab dimensions. One of the biggest obstacles to be overcome in creating such materials is the presence of anti-site defects, whereby a transition metal ion resides on a lithium crystallographic site and vice versa (Figure 2.5). The transition metal ions located within the lithium plane interact strongly with the adjacent oxygen layers, effectively pinning the lithium slab dimension below its equilibrium value. This occurs over the entire state of charge and the effects are most pronounced in the delithiated state as it severely inhibits the expansion of the lithium slab (Figure 2.4).

In order for intercalation of lithium to occur there must be a corresponding uptake and transport of electrons to maintain charge neutrality. Electronic conductivity in the layered oxide materials is generally several orders of magnitude higher than ionic conductivity and is often overlooked.[5, 6] However, the electrochemical behavior of a

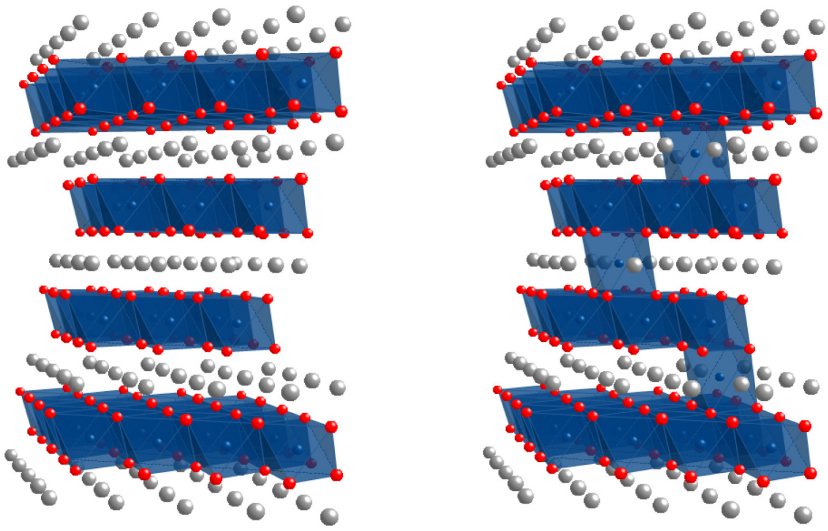

Figure 2.5: Illustrative example of ideal layered active materials (a) and those containing anti-site defects (b). Anti-site defects are formed when transition metal ions (blue octahedra) in the *3a* position exchange with lithium ions residing in the *3b* position. The exchange leads to a constriction of the lithium slab dimension and increased activation energy for lithium diffusion.

system can often be strongly influenced by the underlying electronic structure. These effects can be manifested by such phenomena as non-monotonous charge and discharge curves and metallic-insulator or metallic-semiconductor transitions that drastically alter the charge transfer characteristics.[19, 28-30]

For battery applications, the most important electronic transition that occurs is the shift in conductivity from an insulating (or semiconducting) state at high lithium contents to a metallic state at intermediate lithium concentrations. At high states of charge, electrons are localized on the transition metal centers. As lithium ions and electrons are removed from the host lattice during charge there is a general contraction of the inter-metallic spacing as measured by the *a* unit cell parameter. There is a concurrent increase in d-orbital overlap between transition metal ions.[31] Below a critical value of the metal-metal separation distance, the electrons become delocalized and a metallic character is achieved. Goodenough has developed an empirical equation (Equation 2.3) to identify

$$R_c = \left[3.20 - 0.05m - 0.03(Z - Z_{Ti}) - 0.04s(s+1)\right] \quad \text{Eq. 2.3}$$

the critical separation distance, R_c, at which the transition occurs.[32-35] In Equation 2.3 m is the valance of the transition metal, Z the atomic number of the transition metal, Z_{Ti} the atomic number of titanium, and s is the effective spin. As electronic conductivity is not considered a limiting factor during normal battery operation it will generally be assumed in this work that the ultimate rate performance of a cathode material is associated with the activation energy for lithium diffusion.

2.5 Stabilization of the α-$NaFeO_2$ Structure

As discussed in the previous section, the minimization of the activation energy for lithium diffusion is of key importance in making cathode materials capable of withstanding high discharge rates. To accomplish this, materials with a minimal concentration of anti-site defects must be synthesized to allow for maximum lithium slab dimensions throughout the entire range of lithium solubility. To better understand the conditions required for the synthesis of such ideal materials it is insightful to explore the stability regions in which various polytypes of AMO_2 materials are preferentially formed. It is then possible to establish a practical means of synthesizing such materials, keeping in mind that in order to be viable for large-scale applications both the material and processing costs must be minimized.

Of all of the polytypes listed in Section 2.2 the stabilization of the α-$NaFeO_2$ structure with respect to that of the α-$LiFeO_2$ and γ-$LiFeO_2$ structures is important as the latter show a significant degree of cation intermixing (Figure 2.6). The γ-$LiFeO_2$ structure is related to the rock-salt structure with ordered lithium and transition metal ions giving rise to a tetragonal distortion. Lithium and transition metals alternate in both the tetragonal *c* direction and the basal plane. The structure is related to the α-$NaFeO_2$ structure in that

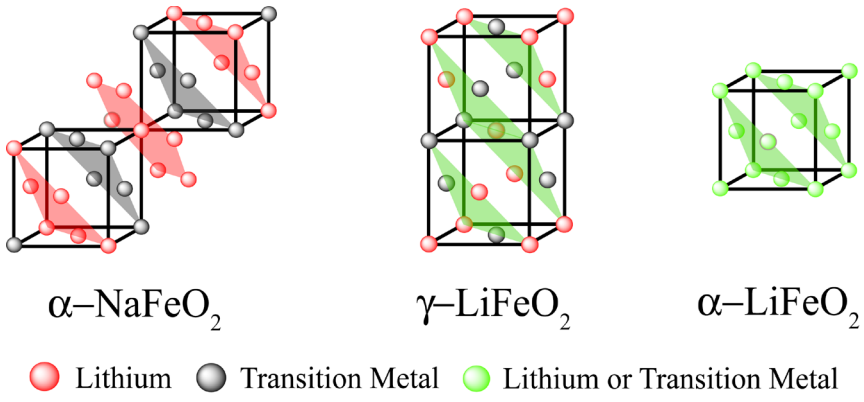

Figure 2.6: Three structural polytypes of the AMO_2 class of materials the α-$NaFeO_2$, α-$LiFeO_2$ and γ-$LiFeO_2$ structures. All of the structures are rock-salt derivatives and are shown in the cubic setting to allow for easier comparison. Lithium planes are marked in red, transition metal planes in gray, and mixed planes in green (oxygen ions omitted for clarity).

it can be derived by the exchange of half of the transition metal and lithium ions (i.e. 50% anti-site defects) in an ordered superstructure. The α-$LiFeO_2$ is the fully disordered rock-salt structure with lithium and transition metals distributed randomly giving rise to a cubic lattice.[36]

A significant amount of research has gone into understanding and predicting the ground state energies and configurations of various alloys and ionic solids.[7, 37 38-40] For the systems of interest in this study, the ground state structure is largely determined by the interaction parameter of the nearest (12 in total) and next-nearest neighbors (6 in total). If only electrostatic interactions are considered, and the Li-O and M-O bond lengths are equal and fixed, the γ-$LiFeO_2$ structure is energetically favored due to a minimization of like nearest neighbor interactions. If in addition to coulombic interactions differences in ionic radii are taken into consideration and bond lengths are allowed to relax, the α-$NaFeO_2$ structure may become the stable ground state configuration for some compositions. Wu *et al.* have related this transition in stability to a more efficient relaxation mechanism in the α-$NaFeO_2$ structure.[7] All of the octahedra in the γ-$LiFeO_2$ structure are perfectly symmetric and there is no mechanism by which long-range relaxation can occur to accommodate a

difference in ionic radius between the lithium and the transition metal ion. In fact, the relaxation of one set of bonds (either Li-O or M-O) inhibits the relaxation of the other. However, due to the existence of infinite layers, comprised solely of either lithium or transition metal ions in the α-$NaFeO_2$ structure, the octahedral environment can distort to accommodate the ionic radius differential. Therefore, one would expect the α-$NaFeO_2$ structure to be favored in materials in which the ionic radius of the transition metal is highly mismatched with respect to that of lithium (0.76 Å).[3] As shown in Table 2.1 this is in fact born out experimentally with compounds having small transition metal/lithium radius ratios favoring the α-$NaFeO_2$ structure.

Table 2.1: The ionic radius of various 3+ transition metals with respect to lithium and the experimentally observed structure. The α-$NaFeO_2$ structure is clearly favored for compositions in which the ionic radius of the transition metal is substantially smaller than that of lithium. (Ionic radii data from Ref. (3) and experimental structure data from Ref. (4) and (7,8).

Cation	Ionic Radius (Å)	M^{3+}/Li^{+} Radius Ratio	Structure (Experimental)
Er^{3+}	0.89	1.17	γ-$LiFeO_2$
Tm^{3+}	0.88	1.16	γ-$LiFeO_2$
Yb^{3+}	0.868	1.14	γ-$LiFeO_2$
Lu^{3+}	0.861	1.13	γ-$LiFeO_2$
In^{3+}	0.8	1.05	γ-$LiFeO_2$
Li^{+}	0.76	1.00	--
Sc^{3+}	0.745	0.98	γ-$LiFeO_2$
Mo^{3+}	0.69	0.91	α-$NaFeO_2$
Rh^{3+}	0.665	0.88	α-$NaFeO_2$
Fe^{3+}	0.645	0.85	γ-$LiFeO_2$
V^{3+}	0.64	0.84	α-$NaFeO_2$
Cr^{3+}	0.615	0.81	α-$NaFeO_2$
Ni^{3+}	0.6	0.79	α-$NaFeO_2$
Co^{3+}	0.545	0.72	α-$NaFeO_2$
Al^{3+}	0.535	0.70	α-$NaFeO_2$

It is important to note that while this analysis predicts the proper ground state structure remarkably well, it ignores several factors that may be important in such systems. The most glaring omissions are that of magnetic interactions and covalent bonding networks. For example, the electrostatic interactions that favor the formation of a γ-$LiFeO_2$ structure may be mitigated for systems exhibiting at least some degree of covalent bonding.

2.6 Substituted Layered Oxide Positive Electrode Materials

Since the first introduction of $LiCoO_2$ as a cathode material for lithium ion batteries in 1980,[13] a tremendous amount of work has been focused on finding new compositions crystallizing in the α-$NaFeO_2$ framework. The materials studied have expanded from unitary to binary and ultimately to tertiary and quaternary lithium transition metal oxides. However, no matter how complex the composition becomes, the ultimate goal remains unchanged, namely to develop a cheaper, less toxic positive electrode material with improved energy density, power density, and abuse tolerance.

Lithium nickel oxide, $LiNiO_2$, was initially explored as a possible replacement positive electrode material due to the higher availability and lower cost of nickel. In addition, $LiNiO_2$ has a higher reversible capacity than $LiCoO_2$ and improved cycle stability.[41-47] Preparation of the stoichiometric $LiNiO_2$ phase may not be possible, however, with the formula $Li_{1-z}Ni_{1+z}O_2$ more accurately reflecting the experimentally observed compositions.[48-53] The exact amount of non-stoichiometry (z) varies considerably and is highly dependent on the experimental conditions used during the synthesis process. The non-stoichiometry is a function of the stability of Ni^{2+} ions in the structure and results in the presence of $z Ni^{2+}$ ions residing within the lithium plane and $z Ni^{2+}$ ions in the transition metal layer.[54-56] The Ni^{2+} in the lithium plane pins the lithium layers together and results in decreased lithium mobility and poor power performance. Further impeding the use of $LiNiO_2$ in commercial batteries is the fact that the structure is unstable at high states

of charge due to an elevated effective equilibrium partial pressure of oxygen.[1, 57] When combined in a high-energy cell with an organic electrolyte, a dangerous thermal event can occur, possibly resulting in a catastrophic cell failure.

Lithium manganese oxide, $LiMnO_2$, is of great interest due to the low cost and toxicity of manganese and high initial charge capacities. While direct synthesis of the lithiated phase is precluded by the fact that it is thermodynamically unstable with respect to the spinel phase ($LiMn_2O_4$),[1, 58] it can be synthesized through ion-exchange pathways from the sodium analog $NaMnO_2$.[59] Due to the presence of Jahn Teller active Mn^{3+}, the unit cell is distorted from rhombohedral to monoclinic symmetry. Materials synthesized by ion exchange deliver an initial charge capacity of ~270 mAh/g below 4.3 V, although a rapid capacity fade is observed as the structure converts to a pseudo-spinel structure during cycling.[59, 60] First principle calculations indicate that the conversion to spinel is associated with the charge-disproportionation reaction of Mn^{3+}, and that stabilization by substitution with low valent cations may be effective at inhibiting the transition.[58]

The extension to new compositions based on the solid solution of various oxides crystallizing in the α-$NaFeO_2$ structure was a natural progression and has led to the synthesis of a host of new materials. For example, the binary compositions, $LiCo_yNi_{1-y}O_2$,[54, 61-68] and $LiNi_yFe_{1-y}O_2$[69-73] have been studied extensively. Mixed manganese-cobalt oxide, $LiCo_yMn_{1-y}O_2$, has been synthesized by ion exchange from the sodium analog. In $LiCo_yMn_{1-y}O_2$ the electronic conductivity of the substituted material is several orders of magnitude higher than that of $LiMnO_2$, but the conversion to the spinel structure is not fully suppressed and little work has been done on the material subsequently.[74] A solid solution up to $y \leq 0.5$ has been reported in the mixed manganese-nickel oxides, $LiNi_yMn_{1-y}O_2$, with the electrochemical performance improving as y is increased.[75-77] The particular composition, $LiNi_{0.5}Mn_{0.5}O_2$, has generated a large amount of interest and is capable of delivering 200 mAh/g between 2.5 and 4.5V at low rates.[78] In contrast to other mixed nickel-manganese oxides, in $LiNi_{0.5}Mn_{0.5}O_2$ the formal oxidation states are found to be

Ni^{2+} and Mn^{4+}. This indicates that $LiNi_{0.5}Mn_{0.5}O_2$ is in fact a new compound and not simply a solid solution mixture of $LiNiO_2$ and $LiMnO_2$.[79] During charge, Ni^{2+} is fully oxidized to Ni^{4+} while manganese remains in the +4 oxidation state, imparting a degree of structural stability to the material. $LiNi_{0.5}Mn_{0.5}O_2$ materials synthesized using traditional methods generally suffer from ~10% anti-site mixing between the lithium and nickel ions and hence exhibit poor rate performance.[80] Electrodes made by ion exchange from the sodium analogs, however, show very little anti-site mixing and are able to sustain high rate discharge cycles (Figure 2.7).[27] These materials, while perhaps impractical for commercialization, serve as a great example of the improvements in electrochemical performance that are possible with an optimized layered structure.

The "layered-layered" composite materials, xLi_2MnO_3-(1-x)$LiMO_2$ (M=Mn, Co, Ni), pioneered by the Thackery group at Argonne National Laboratory show great promise

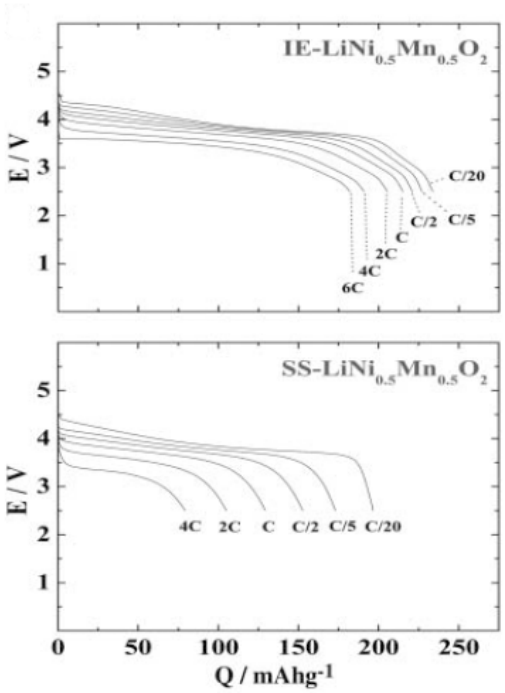

Figure 2.7: Comparison of the discharge curves for $LiNi_{0.5}Mn_{0.5}O_2$ materials synthesized by ion exchange from the sodium (IE) or analog or direct solid-state reactions (SS). Due to the low concentration of anti-site defects in the ion exchanged materials a very high discharge rate can be sustained. Plot from ref. (26).

for achieving discharge capacities exceeding 200 mAh/g. Based on the insights gained from the study of materials such as α-MnO_2 and β″-alumina, these materials aim to impart stability by the incorporation of electrochemically inert structural units.[81] When Li_2MnO_3 is rewritten in the layered notation as $Li[Li_{1/3}Mn_{2/3}]O_2$, it can be immediately observed that all of the manganese is in the 4+ oxidation state. Electrochemical activity can be obtained by reducing a portion of the manganese, forming a $LiMnO_2$ layered component. If these materials are charged to high potentials (>4.4-4.6 V vs. Li/Li^+), lithium can be extracted in excess of that expected, given the phase fraction of active material (*x*). In this case, a simultaneous release of oxygen and lithium is observed from the Li_2MnO_3 phase forming Li_2O. This reaction creates MnO_2-like domains that are electrochemically active and yet stabilized by the remaining Li_2MnO_3 structural units. While these materials show great promise as high-energy electrodes the requirement of high voltage formation cycles and the release of Li_2O remain severe obstacles yet to be overcome.

The ternary oxides, $LiNi_{1-y-z}Co_yMn_zO_2$, created from the solid solution of $LiNi_{0.5}Mn_{0.5}O_2$ and $LiCoO_2$ have been examined by a wide number of research groups. These materials show improved capacities, rate capabilities, and thermal characteristics as compared to the mixed binary oxides discussed previously.[1] In particular, the compositions of $LiNi_{1/3}Co_{1/3}Mn_{1/3}O_2$[82-90] and $LiNi_{0.4}Co_{0.2}Mn_{0.4}O_2$[1, 91-93] have been identified as promising positive electrode materials and serve as baseline materials for the research outlined in the subsequent chapters of this report. These materials are viewed to combine the benefits of the structural stability of Mn^{4+} with the improved lamellar structure characteristic of materials with high cobalt contents. Room for further improvement remains, however, as these materials do suffer from ~6% anti-site mixing, suggesting the rate performance could be further optimized under the proper conditions.

More recently, there has been increased interest in understanding the effects of the substitution of electrochemically inactive elements on both structure and electrochemical properties. Aluminum substitution has been explored owing to the fact that α-$LiAlO_2$ is

isostructural with $LiCoO_2$ (α-$NaFeO_2$) at temperatures below 600° C.[94, 95] At temperatures above 600° C, the α-$LiAlO_2$ phase becomes unstable with respect to the γ-$LiAlO_2$ phase (tetragonal γ-$NaFeO_2$, 4_12_12) where aluminum and lithium ions are found to reside in tetrahedral coordination.[96] However, stable $LiM_yAl_{1-y}O_2$ solid solutions can be formed at temperatures exceeding 600° C due to entropically driven mixing with decreasing solubility at higher temperatures. The series of compositions, $LiCo_yAl_{1-y}O_2$[71, 95, 97-101] and $LiNi_yAl_{1-y}O_2$,[57, 66, 100, 102-109] are the most common examples in the literature. The extraction of lithium from α-$LiAlO_2$ has been predicted to be feasible from first principle methods.[110] The reaction is expected to occur at voltages approaching 5.4 V versus Li/Li^+ (4.7 V average intercalation voltage)[110] and due to the electronically insulating nature of α-$LiAlO_2$, a reversible reaction is not expected.[111] As aluminum is found in the 3+ oxidation state it can not participate in the electrochemical reaction. Instead, it has been proposed that charge transfer in α-$LiAlO_2$ structure is accomplished completely by the oxygen ions due to the high energy of the unfilled aluminum *2p* orbitals and the lack of available *d*-states. In materials with only partial aluminum substitution, charge compensation is primarily centered on the redox active transition metal sites, although a finite amount of charge is incorporated on the adjacent oxygen ions. The activation of oxygen states in the lithium intercalation reaction increases the cell voltage for a given state of charge. The increase in average cell voltage is particularly interesting when considering the theoretical energy densities of such materials. Furthermore, the presence of an electrochemically inactive element can stabilize the host structure through chemical bonding interactions or by inhibiting the complete removal of lithium ions.

2.7 Conclusions

The layered oxide class of cathode materials has been the mainstay of high-energy commercial batteries for small portable applications for the last twenty years. Subsequent research activities have led to the discovery of numerous novel chemical compositions

crystallizing in the α-$NaFeO_2$ structure that are pushing the boundaries in terms of positive electrode energy density, rate performance, and safety. Future improvements and insights are still required to fully realize the ultimate performance of these materials, especially if they are to be utilized in large-scale vehicular applications.

2.8 References

1. Whittingham, M.S., *Lithium batteries and cathode materials.* Chemical Reviews, 2004. **104**(10): p. 4271-4301.

2. Ohzuku, T. and R.J. Brodd, *An overview of positive-electrode materials for advanced lithium-ion batteries.* Journal of Power Sources, 2007. **174**(2): p. 449-456.

3. Nagaura, T., *Development of rechargeable lithium batteries, I. Lithium manganese oxide rechargeable batteries.* Progress in Batteries & Battery Materials, 1991. **10**: p. 209-217.

4. Nagaura, T., *Development of rechargeable lithium batteries, II. Lithium ion rechargeable batteries.* Progress in Batteries & Battery Materials, 1991. **10**: p. 218-226.

5. Whittingham, M.S., *Chemistry of intercalation compounds: Metal guests in chalcogenide hosts.* Progress in Solid State Chemistry, 1978. **12**(1): p. 41-99.

6. Whittingham, M.S., *Electrical Energy-Storage and Intercalation Chemistry.* Science, 1976. **192**(4244): p. 1126-1127.

7. Whittingham, M.S., *The hydrated intercalation complexes of the layered disulfides.* Materials Research Bulletin, 1974. **9**(12): p. 1681-1689.

8. Whittingham, M.S. and F.R. Gamble Jr, *The lithium intercalates of the transition metal dichalcogenides.* Materials Research Bulletin, 1975. **10**(5): p. 363-371.

9. Mizushima, K., et al., *Li(x)CoO(2) (0<x<1): A new cathode material for batteries of high energy density.* Materials Research Bulletin, 1980. **15**(6): p. 783-789.

10. John B. Goodenough, K.M., *Electrochemical cell with new fast ion conductors.* 1981. **06135222**(US 4302518).

11. Whittingham, M.S., *The Role of Ternary Phases in Cathode Reactions.* Journal of the Electrochemical Society, 1976. **123**(3): p. 315-320.

12. Goodenough, J.B., *Design Considerations.* Solid State Ionics, 1994. **69**(3-4): p. 184-198.

13. Hewston, T.A. and B.L. Chamberland, *A Survey of first-row ternary oxides LiMO(2) (M = Sc-Cu).* Journal of Physics and Chemistry of Solids, 1987. **48**(2): p. 97-108.

14. Aydinol, M.K., et al., *First-principles investigation of phase stability in Li(x) CoO(2).* 1998. **58**(6): p. 2976-2987.

15. Wu, E.J., P.D. Tepesch, and G. Ceder, *Size and charge effects on the structural stability of LiMO(2) (M = transition metal) compounds.* Philosophical Magazine B-Physics of Condensed Matter Statistical Mechanics Electronic Optical and Magnetic Properties, 1998. **77**(4): p. 1039-1047.

16. Delmas, C., C. Fouassier, and P. Hagenmuller, *Stuctural classification and properties of the layered oxides.* Physica B & C, 1980. **99**(1-4): p. 81-85.

17. Levi, M.D., et al., *Solid-State Electrochemical Kinetics of Li-Ion Intercalation into Li(1-x)Co)(2): Simultaneous Application of Electroanalytical Techniques SSCV, PITT, and EIS.* Journal of the Electrochemical Society, 1999. **146**(4): p. 1279-1289.

18. Molenda, J., A. Stoklosa, and T. Bak, *Modification in the electronic structure of cobalt bronze Li(x)CoO(2) and the resulting electrochemical properties.* Solid State Ionics, 1989. **36**(1-2): p. 53-58.

19. Imanishi, N., et al., *Preparation and 7Li-NMR study of chemically delithiated Li(1-x)CoO(2) (0<x<0.5).* Solid State Ionics, 1999. **118**(1-2): p. 121-128.

20. Menetrier, M., et al., *The insulator-metal transition upon lithium deintercalation from LiCoO(2): electronic properties and Li-7 NMR study.* Journal of Materials Chemistry, 1999. **9**(5): p. 1135-1140.

21. Nobili, F., et al., *An AC impedance spectroscopic study of Li(x)CoO(2) at different temperatures.* Journal of Physical Chemistry B, 2002. **106**(15): p. 3909-3915.

22. Van der Ven, A. and G. Ceder, *Lithium diffusion mechanisms in layered intercalation compounds.* Journal of Power Sources, 2001. **97-8**: p. 529-531.

23. Delmas, C., et al., *Effect of environment of alkali ion on its mobility in structures with A(x)[L(x)M(1-x)]O(2) sheets.* Materials Research Bulletin, 1979. **14**(3): p. 329-335.

24. Van der Ven, A. and G. Ceder, *Lithium Diffusion in Layered Li(x)CoO(2).* 2000. **3**(7): p. 304.

25. Kang, K. and G. Ceder, *Factors that affect Li mobility in layered lithium transition metal oxides.* Physical Review B (Condensed Matter and Materials Physics), 2006. **74**(9): p. 094105-7.

26. Kang, K.S., et al., *Electrodes with high power and high capacity for rechargeable lithium batteries.* Science, 2006. **311**(5763): p. 977-980.

27. Molenda, J., *Electronic Structure in Relation to the Reactivity of Nonstoichiometric A(x)MX(2) Layered Compounds.* physica status solidi (b), 1991. **165**(2): p. 419-433.

28. Julien, C.M., *Lithium intercalated compounds: Charge transfer and related properties.* Materials Science and Engineering: R: Reports, 2003. **40**(2): p. 47-102.

29. McKinnon, W.R. *Electronic structure of transition-metal chalcogenides and their intercalation compounds*. in *NATO Advanced Study Institute on Chemical Physics of Intercalation*. 1987. Castera Verduzan, France: Plenum Press.

30. Fouassier, C., C. Delmas, and P. Hagenmuller, *Structural development and physical properties of A(x)MO(2) Phases (A=Na,K) (M=Cr,Mn,Co) (x less than or equal to one).* Materials Research Bulletin, 1975. **10**(6): p. 443-449.

31. Goodenough, J.B., *Covalency Criterion for Localized vs Collective Electrons in Oxides with the Perovskite Structure.* Journal of Applied Physics, 1966. **37**(3): p. 1415-1422.

32. Goodenough, J.B., *Narrow-band electrons in transition-metal oxides.* Czechoslovak Journal of Physics, 1967. **17**(4): p. 304-336.

33. Goodenough, J.B., *Metallic oxides.* Progress in Solid State Chemistry, 1971. **5**: p. 145-399.

34. Goodenough, J.B. and P.M. Raccah, *Complex vs Band Formation in Perovskite Oxides.* Journal of Applied Physics, 1965. **36**(3): p. 1031-1032.

35. Cox, D.E., et al., *Neutron diffraction and Mossbauer study of ordered and disordered LiFeO(2).* Physical Review, 1963. **132**(4): p. 1547.

36. Magri, R., S.H. Wei, and A. Zunger, *Ground-state structures and the random-state energy of the Madelung lattice.* Physical Review B, 1990. **42**(17): p. 11388-11391.

37. Li, W., J.N. Reimers, and J.R. Dahn, *Lattice-gas-model approach to understanding the structures of lithium transition-metal oxides LiMO(2).* Physical Review B, 1994. **49**(2): p. 826.

38. Hauck, J., *Short-range order and superstructures of ternary oxides AMO(2), A(2) MO(3) and A(5)MO(6) of monovalent A and multivalent M metals related to the NaCl structure.* Acta Crystallographica Section A, 1980. **36**(2): p. 228-237.

39. Bush, T.S., et al., *Self-consistent Interatomic Potentials for the Simulation of Binary and Ternary Oxides.* Journal of Materials Chemistry, 1994. **4**(6): p. 831-837.

40. Shannon, R., *Revised effective ionic radii and systematic studies of interatomic distances in halides and chalcogenides.* Acta Crystallographica Section A, 1976. **32**(5): p. 751-767.

41. Broussely, M., et al., *Li(x)NiO(2), a promising cathode for rechargeable lithium batteries.* Journal of Power Sources, 1995. **54**(1): p. 109-114.

42. Goodenough, J.B., K. Mizushima, and T. Takeda, *Solid-Solution Oxides for Storage-Battery Electrodes.* Jpn. J. Appl. Phys., 1980. **19-3**: p. 305-313.

43. Ohzuku, T., et al., *Comparative study of LiCoO(2), LiNi(1/2)Co(1/2)O(2) and LiNiO(2) for 4 volt secondary lithium cells.* Electrochimica Acta, 1993. **38**(9): p. 1159-1167.

44. Li, W., J.N. Reimers, and J.R. Dahn, *In situ x-ray diffraction and electrochemical studies of Li(1-x)NiO(2).* Solid State Ionics, 1993. **67**(1-2): p. 123-130.

45. Koksbang, R., et al., *Cathode materials for lithium rocking chair batteries.* Solid State Ionics, 1996. **84**(1-2): p. 1-21.

46. Ohzuku, T., A. Ueda, and M. Nagayama, *Electrochemistry and Structural Chemistry of LiNiO(2) (R-3m) for 4 Volt Secondary Lithium Cells.* Journal of the Electrochemical Society, 1993. **140**(7): p. 1862-1870.

47. Bianchi, V., et al., *Synthesis, structural characterization and magnetic properties of quasistoichiometric LiNiO(2).* Solid State Ionics, 2001. **140**(1-2): p. 1-17.

48. Rougier, A., P. Gravereau, and C. Delmas, *Optimization of the Composition of the Li(1-z)Ni(1+z)O(2) Electrode Materials: Structural, Magnetic, and Electrochemical Studies.* Journal of The Electrochemical Society, 1996. **143**(4): p. 1168-1175.

49. Chappel, E., et al., *High magnetic field study of quasi-stoichiometric Li(1-x)Ni(1+x)O(2).* Physica B, 2001. **294**: p. 124-127.

50. Chappel, E., et al., *Low field magnetism and cationic distribution in quasi-stoichiometric Li(1-x)Ni(1+x)O(2).* Solid State Communications, 2001. **119**(2): p. 83-87.

51. Delmas, C., et al., *On the behavior of the Li(x)NiO(2) system: an electrochemical and structural overview.* Journal of Power Sources, 1997. **68**(1): p. 120-125.

52. Nunez-Regueiro, M.D., et al., *Magnetic structure of S=1/2 triangular Li(1-x)Ni(1+x)O(2).* Physica B, 1999. **261**: p. 1003-1004.

53. Nunez-Regueiro, M.D., et al., *Magnetic structure of Li(1-x)Ni(1+x)O(2).* European Physical Journal B, 2000. **16**(1): p. 37-41.

54. Delmas, C., et al., *An overview of the Li(Ni,M)O(2) systems: syntheses, structures and properties.* Electrochimica Acta, 1999. **45**(1-2): p. 243-253.

55. Rougier, A., C. Delmas, and G. Chouteau, *Magnetism of Li(1-z)Ni(1+z)O(2): A powerful tool for structure determination.* Journal of Physics and Chemistry of Solids, 1996. **57**(6-8): p. 1101-1103.

56. Peres, J.P., et al., *The relationship between the composition of lithium nickel oxide and the loss of reversibility during the first cycle.* Journal of Physics and Chemistry of Solids, 1996. **57**(6-8): p. 1057-1060.

57. Guilmard, M., et al., *Thermal Stability of Lithium Nickel Oxide Derivatives. Part I: Li(x)Ni(1.02)O(2) and Li(x)Ni(0.89)Al(0.16)O(2) (x= 0.50 and 0.30).* Chem. Mater., 2003. **15**(23): p. 4476-4483.

58. Reed, J., G. Ceder, and A. Van Der Ven, *Layered-to-Spinel Phase Transition in Li(x)MnO(2).* 2001. **4**(6): p. A78-81.

59. Armstrong, A.R. and P.G. Bruce, *Synthesis of layered LiMnO(2) as an electrode for rechargeable lithium batteries.* Nature, 1996. **381**(6582): p. 499-500.

60. Armstrong, A.R., et al., *Nonstoichiometric Layered Li(x)Mn(y)O(2) with a High Capacity for Lithium Intercalation/Deintercalation.* Chem. Mater., 2002. **14**(2): p. 710-719.

61. Delmas, C. and I. Saadoune, *Electrochemical and Physical-Properties of the Li(x) Ni(1-y)Co(y)O(2) Phases.* Solid State Ionics, 1992. **53-6**: p. 370-375.

62. Delmas, C., I. Saadoune, and A. Rougier, *The Cycling Properties of the Li(x)Ni(1-y) Co(y)O(2) Electrode.* Journal of Power Sources, 1993. **44**(1-3): p. 595-602.

63. Rougier, A., et al., *Effect of cobalt substitution on cationic distribution in LiNi(1 - y) Co(y)O(2) electrode materials.* Solid State Ionics, 1996. **90**(1-4): p. 83-90.

64. Saadoune, I. and C. Delmas, *LiNi(1-y)Co(y)O2 positive electrode materials: Relationships between the structure, physical properties and electrochemical behaviour.* Journal of Materials Chemistry, 1996. **6**(2): p. 193-199.

65. Saadoune, I. and C. Delmas, *On the Li(x)Ni(0.8)Co(0.2)O(2) system.* Journal of Solid State Chemistry, 1998. **136**(1): p. 8-15.

66. Ohzuku, T., K. Nakura, and T. Aoki, *Comparative study of solid-state redox reactions of LiCo(1/4)Ni(3/4)O(2) and LiAl(1/4)Ni(3/4)O(2) for lithium-ion batteries.* Electrochimica Acta, 1999. **45**(1-2): p. 151-160.

67. Ueda, A. and T. Ohzuku, *Solid-State Redox Reactions of LiNi(1/2)Co(1/2)O(2) (R-3m) for 4 Volt Secondary Lithium Cells.* Journal of the Electrochemical Society, 1994. **141**(8): p. 2010-2014.

68. Cho, J., G. Kim, and H.S. Lim, *Effect of preparation methods of LiNi(1-x)Co(x) O(2) cathode materials on their chemical structure and electrode performance.* Journal of the Electrochemical Society, 1999. **146**(10): p. 3571-3576.

69. Prado, G., et al., *Cationic distribution in the Li(1-z)[Ni(1-y)Fe(y)](1+z)O(2) electrode materials.* Journal of Materials Chemistry, 2000. **10**(11): p. 2553-2560.

70. Chappel, E., et al., *Magnetic properties of LiNi(1-y)Fe(y)O(2).* Solid State Ionics, 2003. **159**(3-4): p. 273-278.

71. Jang, Y.I., et al., *Synthesis and characterization of LiAl(y)Co(1-y)O(2) and LiAl(y) Ni(1-y)O(2).* Journal of Power Sources, 1999. **82**: p. 589-593.

72. Mueller-Neuhaus, J.R., R.A. Dunlap, and J.R. Dahn, *Understanding Irreversible Capacity in Li(x)Ni(1-y)Fe(y)O(2) Cathode Materials.* Journal of The Electrochemical Society, 2000. **147**(10): p. 3598-3605.

73. Reimers, J.N., et al., *Structure and electrochemistry of Li(x)Fe(y)Ni(1-y)O(2).* Solid State Ionics, 1993. **61**(4): p. 335-344.

74. Armstrong, A.R., A.D. Robertson, and P.G. Bruce, *Structural transformation on cycling layered LiMn(1-y)Co(y)O(2) cathode materials.* Electrochimica Acta, 1999. **45**(1-2): p. 285-294.

75. Spahr, M.E., et al., *Characterization of Layered Lithium Nickel Manganese Oxides Synthesized by a Novel Oxidative Coprecipitation Method and Their Electrochemical Performance as Lithium Insertion Electrode Materials.* Journal of The Electrochemical Society, 1998. **145**(4): p. 1113-1121.

76. Rossen, E., C.D.W. Jones, and J.R. Dahn, *Structure and electrochemistry of Li(x) Mn(y)Ni(1-y)O(2).* Solid State Ionics, 1992. **57**(3-4): p. 311-318.

77. Ohzuku, T. and Y. Makimura, *Layered lithium insertion material of LiNi(1/2) Mn(1/2)O(2): A possible alternative to LiCoO(2) for advanced lithium-ion batteries.* Chemistry Letters, 2001(8): p. 744-745.

78. Makimura, Y. and T. Ohzuku, *Lithium insertion material of LiNi(1/2)Mn(1/2)O(2) for advanced lithium-ion batteries.* Journal of Power Sources, 2003. **119**: p. 156-160.

79. Ohzuku, T., et al., *Materials strategy for advanced lithium-ion (shuttlecock) batteries: lithium nickel manganese oxides with or without cobalt.* Electrochemistry, 2005. **73**(1): p. 2-11.

80. Hinuma, Y., et al., *Phase transitions in the LiNi(0.5)Mn(0.5)O(2) system with temperature.* Chemistry of Materials, 2007. **19**(7): p. 1790-1800.

81. Thackeray, M.M., et al., *Li(2)MnO(3)-stabilized LiMO(2) (M = Mn, Ni, Co) electrodes for lithium-ion batteries.* Journal of Materials Chemistry, 2007. **17**(30): p. 3112-3125.

82. Cho, T.-H., Y. Shiosaki, and H. Noguchi, *Preparation and characterization of layered LiMn(1/3)Ni(1/3)Co(1/3)O(2) as a cathode material by an oxalate co-precipitation method.* Journal of Power Sources, 2006. **159**(2): p. 1322-1327.

83. Belharouak, I., et al., *Safety characteristics of LiNi(0.8)Co(0.15)Al(0.05)O(2) and LiNi(1/3)Co(1/3)Mn(1/3)O(2).* Electrochemistry Communications, 2006. **8**(2): p. 329-335.

84. Yabuuchi, N., et al., *Solid-State Chemistry and Electrochemistry of LiCo(1/3)Ni(1/3) Mn(1/3)O(2) for Advanced Lithium-Ion Batteries.* Journal of the Electrochemical Society, 2005. **152**(7): p. A1434-A1440.

85. Shaju, K.M., G.V.S. Rao, and B.V.R. Chowdari, *Influence of Li-ion kinetics in the cathodic performance of layered LiNi(1/3)Co(1/3)Mn(1/3)O(2).* Journal of the Electrochemical Society, 2004. **151**(9): p. A1324-A1332.

86. Yabuuchi, N. and T. Ohzuku, *Novel lithium insertion material of LiCo(1/3)Ni(1/3) Mn(1/3)O(2) for advanced lithium-ion batteries.* Journal of Power Sources, 2003. **119-121**: p. 171-174.

87. Hwang, B.J., et al., *A combined computational/experimental study on LiNi(1/3) Co(1/3)Mn(1/3)O(2).* Chemistry of Materials, 2003. **15**(19): p. 3676-3682.

88. Belharouak, I., et al., *LiNi(1/3)Co(1/3)Mn(1/3)O(2) as a suitable cathode for high power applications.* Journal of Power Sources, 2003. **123**(2): p. 247-252.

89. Shaju, K.M., G.V. Subba Rao, and B.V.R. Chowdari, *Performance of layered LiNi(1/3)Co(1/3)Mn(1/3)O(2) as cathode for Li-ion batteries.* Electrochimica Acta, 2002. **48**(2): p. 145-151.

90. Ohzuku, T. and Y. Makimura, *Layered lithium insertion material of LiCo(1/3) Ni(1/3)Mn(1/3)O(2) for lithium-ion batteries.* Chemistry Letters, 2001(7): p. 642-643.

91. Ma, M., et al., *Structural and electrochemical behavior of LiMn(0.4)Ni(0.4)Co(0.2) O(2).* Journal of Power Sources, 2007. **165**(2): p. 517-534.

92. Li, J., J.M. Zheng, and Y. Yang, *Studies on Storage Characteristics of LiNi(0.4) Co(0.2)Mn(0.4)O(2) as Cathode Materials in Lithium-Ion Batteries.* Journal of The Electrochemical Society, 2007. **154**(5): p. A427-A432.

93. Ngala, J.K., et al., *The synthesis, characterization and electrochemical behavior of the layered LiNi(0.4)Mn(0.4)Co(0.2)O(2) compound.* Journal of Materials Chemistry, 2004. **14**(2): p. 214-220.

94. Lehmann, H.A. and H. Hesselbarth, *Zur Kenntnis Der Lithiumaluminate .1. Uber Eine Neue Modifikation Des Lialo2.* Zeitschrift Fur Anorganische Und Allgemeine Chemie, 1961. **313**(1-2): p. 117-120.

95. Buta, S., et al., *Phase separation tendencies of aluminum-doped transition-metal oxides LiAl(1-x)M(x)O(2) in the alpha-NaFeO(2) crystal structure.* Journal of the Electrochemical Society, 1999. **146**(12): p. 4335-4338.

96. Marezio, M., *The crystal structure and anomalous dispersion of [gamma]-LiAlO(2).* Acta Crystallographica, 1965. **19**(3): p. 396-400.

97. Amdouni, N., et al., *LiAl(y)Co(1-y)O(2) (0<y<0.3) intercalation compounds synthesized from the citrate precursors.* Materials Chemistry and Physics, 2003. **80**(1): p. 205-214.

98. Huang, H., G.V.S. Rao, and B.V.R. Chowdari, *LiAl(x)Co(1-x)O(2) as 4 V cathodes for lithium ion batteries.* Journal of Power Sources, 1999. **81-82**: p. 690-695.

99. Julien, C., et al., *LiCo(1-y)M(y)O(2) positive electrodes for rechargeable lithium batteries - I. Aluminum doped materials.* Materials Science and Engineering B-Solid State Materials for Advanced Technology, 2002. **95**(1): p. 6-13.

100. Julien, C., G.A. Nazri, and A. Rougier, *Electrochemical performances of layered LiM(1-y)M'(y)O(2) (M = Ni, Co; M' = Mg, Al, B) oxides in lithium batteries.* Solid State Ionics, 2000. **135**(1-4): p. 121-130.

101. Khan, M.N. and J. Bashir, *Synthesis and structural refinement of LiAl(x)Co(1-x) O(2) system.* Materials Research Bulletin, 2006. **41**(9): p. 1589-1595.

102. Guilmard, M., L. Croguennec, and C. Delmas, *Thermal Stability of Lithium Nickel Oxide Derivatives. Part II: Li(x)Ni(0.70)Co(0.15)Al(0.15)O(2) and Li(x)Ni(0.90) Mn(0.10)O(2) (x = 0.50 and 0.30). Comparison with Li(x)Ni(1.02)O(2) and Li(x) Ni(0.89)Al(0.16)O(2).* Chem. Mater., 2003. **15**(23): p. 4484-4493.

103. Ohzuku, T. and K. Nakura, *Solid state electrochemistry of intercalation compound of LiAl(1/2)Ni(1/2)O(2) (R-3m) for lithium-ion batteries.* Denki Kagaku, 1998. **66**(12): p. 1209-1214.

104. Ohzuku, T., A. Ueda, and M. Kouguchi, *Synthesis and Characterization of LiAl(1/4)Ni(3/4)O(2) (R-3m) for Lithium-Ion (Shuttlecock) Batteries.* Journal of The Electrochemical Society, 1995. **142**(12): p. 4033-4039.

105. Julien, C. and M. Massot, *Raman scattering of LiNi(1-y)Al(y)O(2).* Solid State Ionics, 2002. **148**(1-2): p. 53-59.

106. Kim, J., et al., *Effect of (Al, Mg) substitution in LiNiO(2) electrode for lithium batteries.* Journal of Power Sources, 2006. **158**(1): p. 641-645.

107. Ohzuku, T., et al., *Innovative insertion material of LiAl(1/4)Ni(3/4)O(2) (R-3m) for lithium-ion (shuttlecock) batteries.* Journal of Power Sources, 1997. **68**(1): p. 131-134.

108. Shinova, E., E. Zhecheva, and R. Stoyanova, *Formation of LiAl(y)Ni(1-y)O(2) solid solutions under high and atmospheric pressure.* Journal of Solid State Chemistry, 2006. **179**(10): p. 3151-3158.

109. Zhong, Q. and U. von Sacken, *Crystal structures and electrochemical properties of LiAl(y)Ni(1−y)O(2) solid solution.* J. Power Sources, 1995. **54**(2): p. 221- 223.

110. Aydinol, M.K., et al., *Ab initio study of lithium intercalation in metal oxides and metal dichalcogenides.* Physical Review B, 1997. **56**(3): p. 1354-1365.

111. Ceder, G., et al., *Identification of cathode materials for lithium batteries guided by first-principles calculations.* Nature, 1998. **392**(6677): p. 694-696.

3. Structure and Electrochemistry of $LiNi_{1/3}Co_{1/3-y}M_yMn_{1/3}O_2$ (M=Ti, Al, Fe) Positive Electrode Materials

3.1 Abstract

A series of materials based on the $LiNi_{1/3}Co_{1/3-y}M_yMn_{1/3}O_2$ (M=Ti, Al, Fe) system have been synthesized and examined structurally and electrochemically. It is found that the changes in electrochemical performance depend highly on the nature of the substituting atom and its effect on the crystal structure. Substitution with small amounts of Ti^{4+} (y=1/12) leads to the formation of a high capacity and high-rate positive electrode material. Iron substituted materials suffer from an increased anti-site defect concentration and exhibit lower capacities and poor rate capabilities. Single-phase materials are found for $LiNi_{1/3}Co_{1/3-y}Al_yMn_{1/3}O_2$ when $y \leq 1/4$ and all exhibit decreased capacities when cycled to 4.3 V. However, an increase in rate performance and cycle stability upon aluminum substitution is correlated with an improved lamellar structure.[1]

3.2 Introduction

A significant amount of research has been directed at finding positive electrode materials with high capacity as well as low cost and toxicity to replace $LiCoO_2$. Of particular interest is the series of materials, $LiNi_{1-y-z}Co_yMn_zO_2$, which potentially combine the rate performance of $LiCoO_2$, the high capacity of $LiNiO_2$, and the structural stabilization imparted by the presence of Mn^{4+}.[2, 3] Specifically, $LiNi_{1/3}Co_{1/3}Mn_{1/3}O_2$ has garnered much attention and has been shown to deliver 150 mAh/g between 2.5 and 4.2 V versus lithium and close to 200 mAh/g when the charge potential limit is increased to 4.6 volts.[4-8] In addition, $LiNi_{1/3}Co_{1/3}Mn_{1/3}O_2$ possesses excellent power characteristics, exceeding the high power pulse requirement for hybrid vehicle applications,[9] and increased thermal abuse tolerance compared to $LiNi_{0.8}Co_{0.15}Al_{0.05}O_2$.[10]

The inherent improvements in rate capability of $LiNi_{1/3}Co_{1/3}Mn_{1/3}O_2$ over other

oxide materials, including $LiNi_{0.5}Mn_{0.5}O_2$ produced using traditional methods,[11-13] is due largely to the structural properties associated with the presence of cobalt. AMO_2 type materials with the highly layered α-$NaFeO_2$ structure (space group $R\bar{3}m$), where A is typically Li^+ and M is a metal 3+ cation, are stabilized for metal ions with an ionic radius substantially smaller than that of lithium (0.76 Å).[14, 15] Due to the small ionic radius of low spin Co^{3+} (0.545 Å) the incorporation of cobalt into the crystal lattice minimizes anti-site cation defect concentrations leading to facile lithium ion transport.[15-19]

To create electrode materials with further reduced cobalt contents and lower anti-site defect concentrations, while avoiding effective but complicated ion exchange pathways,[20] substitutive elements should promote the formation of a lamellar structure through either steric or chemical interactions. Iron, which has an ionic radius of 0.645 Å in the low spin state, is an attractive replacement for cobalt due to its low cost and toxicity. However, the native lithiated oxide, $LiFeO_2$, is not layered like α-$NaFeO_2$ but has an ordered tetragonal structure (γ-$LiFeO_2$, space group $I4_1/amd$).[21, 22] Accordingly, substitution into the layered oxide materials has been limited to relatively low levels. $LiNi_{1/3}Co_{1/6}Fe_{1/6}Mn_{1/3}O_2$, synthesized using a sol-gel synthesis method delivers approximately 150 mAh/g between 3.0 and 4.5 V vs. Li/Li^+ although a ~20% capacity fade within the first 30 cycles was observed.[23]

A previous report on the selective replacement of cobalt with aluminum in the series $LiNi_{1/3}Al_{1/3-x}Co_xMn_{1/3}O_2$ indicates that single phase materials are formed for $1/6 \leq x \leq 1/3$.[24] Interestingly, even given the small ionic radius of the Al^{3+} ion (0.545 Å), an increase in the cation mixing was observed. This was connected with an increased cell polarization and limited capacity below 4.5 V (~120 mAh/g at x=0).

Several different titanium substituted layered oxides have been reported in the literature including $LiCo_{1-z}Ti_zO_2$ (z=0.25, 0.5),[25] $LiNi_{1-x}Ti_xO_2$ ($0 \leq x \leq 0.1$, 0.5),[26, 27] $LiNi_{0.8-y}Ti_yCo_{0.2}O_2$ ($0 \leq y \leq 0.1$),[28] and $LiNi_{0.8}Ti_{0.1}Co_{0.1}O_2$.[29] In most cases, it was found that the incorporation of titanium leads to improved reversibility and thermal stability. The

structural effects of titanium substitution remain unclear, however, with both increasing and decreasing anti-site defect concentrations being reported. Depending on the chemistry involved, this result is not surprising, as substitution with Ti^{4+} may lead to the formation of a Ni^{2+} component for charge compensation. Divalent nickel has a strong propensity to migrate to the lithium *3b* site and may account for at least some of the disparities reported experimentally.

The goal of this work is to understand the systematic changes caused by substitution of Fe^{3+}, Al^{3+}, and Ti^{4+} for Co^{+3} in $LiNi_{1/3}Co_{1/3-y}M_yMn_{1/3}O_2$, for compositions leading to single-phase materials. The effect of these substitutions on the crystallographic parameters, cycle life, and rate performance are discussed.

3.3 Experimental Procedures

The glycine nitrate combustion (GNC) process was used for the synthesis of all oxide active materials used in this study.[30, 31] Aqueous solutions of $LiNO_3$ (Mallinckrodt), $Mn(NO_3)_2$ (45-50 wt.% in dilute nitric acid, Sigma Aldrich), $Co(NO_3)_2 \cdot 6H_2O$ (98%, Sigma Aldrich), $Ni(NO_3)_2 \cdot 6H_2O$ (Sigma Aldrich), $Al(NO_3)_3 \cdot 9H_2O$ (98+%, Sigma Aldrich), $Fe(NO_3)_3 \cdot 9H_2O$ (98% EMD), and $TiO(NO_3)_2$ and glycine (98.5+%, Sigma Aldrich) corresponding to the desired stoichiometry were combined in a stainless steel combustion chamber. The solution was then concentrated on a hot plate until auto ignition occurred. $TiO(NO_3)_2$ was prepared via the hydrolysis of $TiCl_4$ (99.9%, Sigma Aldrich) with ammonia and subsequent reaction with nitric acid (69%, BDH).[32] For comparison purposes, a constant glycine to nitrate ratio of 0.5 was used for all materials corresponding to a combustion temperature of about 1350° C.[30] After combustion, powders were planetary ball milled for one hour in acetone and dried under flowing nitrogen before being fired at 800° C (4° C/min heating rate) for four hours in air.

Powder X-ray diffraction (XRD) was performed on a Phillips X'Pert diffractometer with an X'celerator detector using Cu Kα radiation. A back loading powder holder was

used to minimize the impact of any preferred orientation. Unit cell parameters were obtained from Rietveld refinement using the WINPLOTR/FullProf suite.[33] Particle morphology studies were conducted using a field emission-scanning electron microscope (FESEM, Jeol JSM-6340F).

Laminate composite electrodes comprised of 84 wt.% active material, 8 wt.% poly(vinylidine fluoride) (PVDF, Kureha Chemical Ind. Co. Ltd.), 4 wt.% compressed acetylene black, and 4 wt.% SFG-6 synthetic flake graphite (Timcal Ltd., Graphites and Technologies) were prepared by applying slurries in 1-methyl-2-pyrrolidinone onto carbon coated current collectors (Intelicoat Technologies) by automated doctor blade. After drying in air and in vacuum for at least 24 hours, 1.8 cm^2 electrodes having an average loading of 7-10 mg/cm^2 of active material were punched out. Coin cells (2032) were assembled in a helium filled glove box with lithium metal anodes and 1M $LiPF_6$ in 1:2 ethylene carbonate/dimethyl carbonate (EC/DMC) electrolyte solution (Ferro). Galvanostatic cycling was carried out on an Arbin BT/HSP-2043 cycler between limits of 2.0 and 4.3-4.7 V. All cells were charged at a current density of 0.1 mA/cm^2 independent of the discharge rate.

3.4 Results and Discussion

The impact of substitution for cobalt in layered oxide systems upon electrochemical performance varies depending on the nature of the substituting atom. Because cobalt does not become electroactive until potentials exceeding 4.3 V, much of the capacity related to the $Co^{3+/4+}$ redox couple is not utilized under normal cycling conditions.[34, 35] Therefore, the effect on practical capacities should be minimal as long as no other properties, such as ionic or electronic conductivity or voltage characteristics, are grossly affected by the substitution. This is significant as it may allow for the substitution of cobalt with electrochemically inactive species such as Al^{+3} that lower the theoretical capacity (e.g., 208 mAh/g for $LiNi_{1/3}Al_{1/3}Mn_{1/3}O_2$) compared to the parent material, $LiNi_{1/3}Co_{1/3}Mn_{1/3}O_2$ (278 mAh/g). Aliovalent substitution with Ti^{+4} requires the reduction of the redox state of

another transition metal species to maintain charge neutrality. The most probable charge balance reaction is partial reduction of Mn^{4+} to Mn^{3+}. Mn^{3+} is electroactive in the window of 3-3.5 V[36] and can compensate for the inactivity of Ti^{4+}. Therefore a slight increase in theoretical capacity is expected (289 mAh/g for the hypothetical $LiNi_{1/3}Ti_{1/3}Mn_{1/3}O_2$ due to the lower atomic weight of titanium compared to cobalt. (It may, however, be difficult to detect manganese electroactivity at the low substitution levels utilized in this study).[26] Iron substituted materials have slightly higher theoretical capacities (e.g., 281 mAh/g for the hypothetical $LiNi_{1/3}Fe_{1/3}Mn_{1/3}O_2$) than the $LiNi_{1/3}Co_{1/3}Mn_{1/3}O_2$ because of the slightly lower atomic weight of iron and its presumed electroactivity.

In this study, single-phase materials were obtained for all substitutions when y was limited to a value of 1/12 in $LiNi_{1/3}Co_{1/3-y}M_yMn_{1/3}O_2$ (M=Ti, Al, Fe). Substitution of titanium and iron at levels greater than 1/12 leads to the formation of spinel-like impurity phases and will not be further discussed. A higher degree of solubility was observed in the aluminum substituted system where an impurity phase was observed only for y=1/3 in this study.

The primary particle size estimated from Rietveld refinement is approximately 40-50 nm for all samples and agrees well with the particle size (50 nm) observed in transmission electron microscope images of similarly produced oxide powders.[31] Figure 3.1 shows an SEM image of the parent material, $LiNi_{1/3}Co_{1/3}Mn_{1/3}O_2$, produced using the glycine nitrate combustion method and is characteristic of all of the materials used in this study. The agglomeration into secondary particles with a diameter of approximately 500 nm can be seen clearly and is typical of all the materials used in this study.

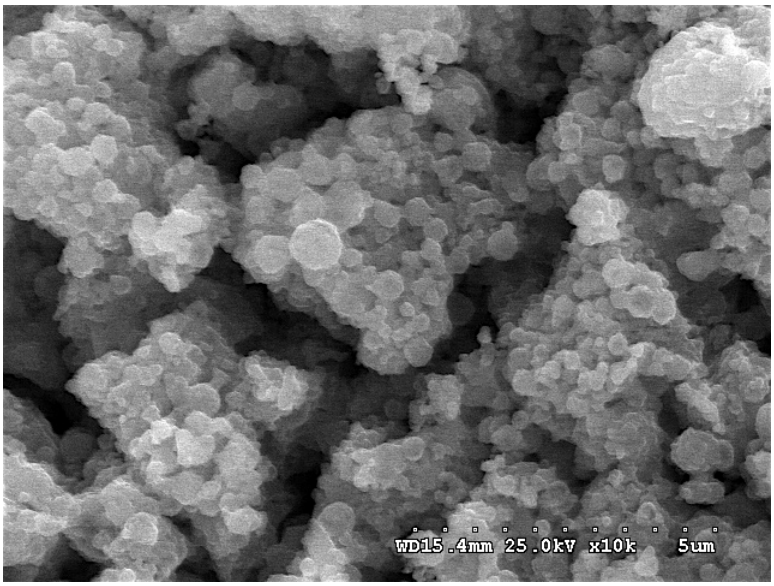

Figure 3.1: SEM image of $LiNi_{1/3}Co_{1/3}Mn_{1/3}O_2$ powder produced via the glycine nitrate combustion method. Secondary particles with a diameters in the range of 500 nm are comprised of ~40-50 nm primary particles.

3.4.1 $LiNi_{1/3}Co_{1/4}M_{1/12}Mn_{1/3}O_2$ (M=Co, Ti, Al, Fe)

The X-ray powder diffraction patterns presented in Figure 3.2 indicate that the substitution of 1/12 of the cobalt content with aluminum, iron, or titanium results in highly crystalline single-phase powders. All peaks could be indexed in the $R\bar{3}m$ space group with no evidence of a second phase (the 200 peak of the aluminum sample holder is, however, evident in the patterns). The results of the Rietveld refinements are presented in Table 3.1. For the α-$NaFeO_2$ structure, the *a* lattice parameter is a measure of the distance between metal centers in the transition metal plane and is relatively unaffected by substitution; only a small shift (0.4% maximum) is observed. The experimentally observed trend is readily explained by the minor differences in ionic radii of cobalt (0.545 Å), aluminum (0.535 Å), titanium (0.605 Å), and iron (0.645 Å).[14] Minor shifts in the *c*-axis are observed upon substitution; the *c* lattice parameter expands to a maximum of 14.298 Å (0.3 %) upon substitution with the largest ion (Ti).

Table 3.1: Structural Parameters of $LiNi_{1/3}Co_{1/3-y}M_yMn_{1/3}O_2$ (M=Co, Ti, Fe, Al) compounds.

Transition Metal	Substitution Level, y	Unit Cell Parameters		Unit Cell Volume (Å^3)	c/3a	z_{Ox}	S (MO_2) (Å)[a]	I (LiO_2) (Å)[a]
		a (Å)	c (Å)					
Co	1/12	2.862(2)	14.254(1)	101.145(2)	1.660	0.2574(2)	2.16	2.59
Ti	1/12	2.870(2)	14.298(2)	101.996(2)	1.661	0.2582(2)	2.15	2.62
Fe	1/12	2.873(3)	14.275(2)	102.072(2)	1.656	0.2590(2)	2.14	2.62
Al	1/12	2.862(2)	14.281(1)	101.332(2)	1.663	0.2596(2)	2.10	2.66
Al	1/6	2.863(2)	14.285(2)	101.423(2)	1.663	0.2593(2)	2.11	2.65
Al	1/4	2.863(2)	14.292(2)	101.437(2)	1.664	0.2590(2)	2.12	2.64
Al	1/3*	2.863(2)	14.298(2)	101.490(2)	1.665	0.2594(2)	2.11	2.66

a) Transition metal slab spacing (S) and lithium slab spacing (I) as defined in Ref. (47)
* γ-$LiAlO_2$ was observed as an impurity in this composition

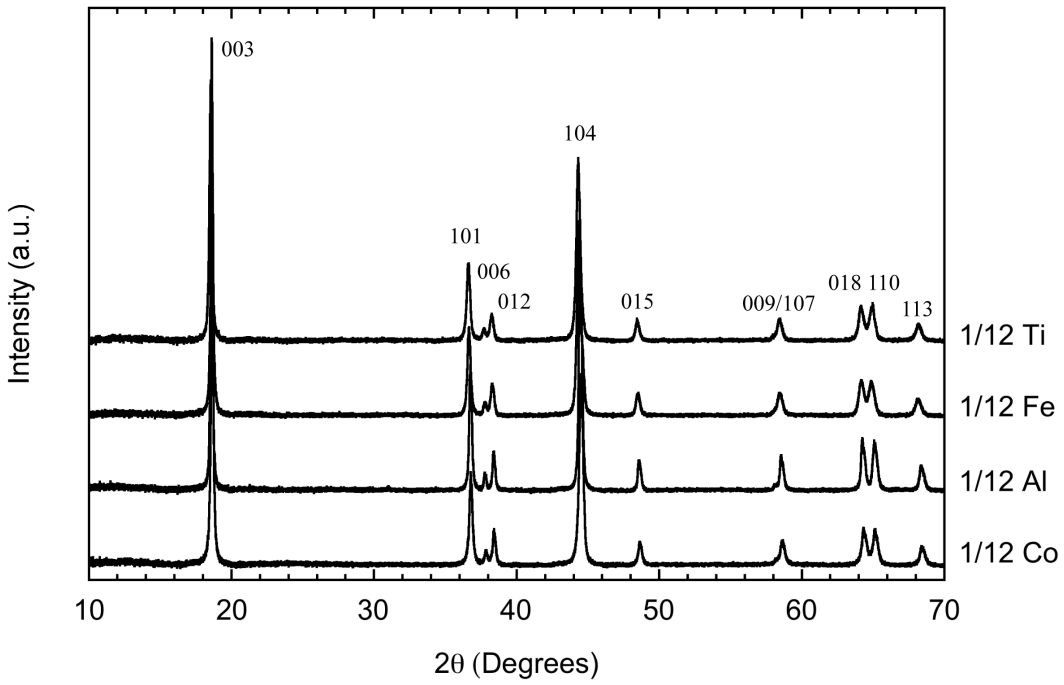

Figure 3.2: Powder XRD patterns of $LiNi_{1/3}Co_{1/4}M_{1/12}Mn_{1/3}O_2$ (M =Ti, Fe, Al, and Co). All materials were single phase and could be indexed to the $R\bar{3}m$ space group.

The overlap of the 200 peak from the aluminum sample holder with the 104 peak of the layered oxides in Figure 3.2 precluded the implicit refinement of the anti-site defect concentration, but the *c/3a* ratio has been shown to be a close corollary for many materials.[37] The ideal structure with a cubic close packed framework has a value of 1.633. For materials with the α-$NaFeO_2$ structure, this ratio increases significantly, approaching 1.793 for an ideal layered material with no ion-mixing, such as $LiTiS_2$.[17] $LiNi_{1/3}Co_{1/3}Mn_{1/3}O_2$ has a *c/3a* ratio of 1.660, implying a significant degree of cation mixing. Substitution with aluminum (1.663) and titanium (1.661) leads to an increase in this value and, presumably, reduced anti-site defect content. In contrast, the *c/3a* ratio of $LiNi_{1/3}Co_{1/4}Fe_{1/12}Mn_{1/3}O_2$ (1.656) is lower than that of the parent compound. This reflects the tendency of materials with high iron content to crystallize in the γ-$LiFeO_2$ structure, with an ordered arrangement of lithium and iron on the *3a* and *3b* crystallographic sites rather than in a lamellar structure. It is important to note, that while large shifts in the

c/3a ratio can generally be ascribed to changes in the anti-site defect concentration, the dimension of the transition metal layer may also change upon substitution. As the ionic radii of low spin Fe^{3+}, Al^{3+}, and Ti^{4+} are not substantially different than that of Co^{3+}, this is not expected to be a large factor in these materials.

$Li/LiNi_{1/3}Co_{1/4}M_{1/12}Mn_{1/3}O_2$ (M=Co, Ti, Al, Fe) cells cycled at low current densities (0.1 mA/cm^2) between 2.0 and 4.3 V (Figure 3.3) show that substitution of even small amounts of cobalt in $LiNi_{1/3}Co_{1/3}Mn_{1/3}O_2$ has a dramatic effect on the electrochemical performance. Cells containing the parent material or $LiNi_{1/3}Co_{1/4}Ti_{1/12}Mn_{1/3}O_2$ deliver ~170 mAh/g on the first discharge and cycle with negligible capacity fade. $Li/LiNi_{1/3}Co_{1/4}Al_{1/12}Mn_{1/3}O_2$ cells cycle equally well, but the discharge capacity is decreased by about 11%. $Li/LiNi_{1/3}Co_{1/4}Fe_{1/12}Mn_{1/3}O_2$ cells only deliver 142 mAh/g initially and the capacity fades rapidly at a rate of 0.6%/cycle. This is similar to previous findings on the effect of Fe substitution in layered transition metal oxides.[22] XPS experiments and *ab-initio* calculations have shown that iron is electroactive in the same potential window as the $Ni^{2+/4+}$ redox couple.[23] Therefore, the reduced practical capacity is assumed to be a result of kinetic rather than thermodynamic limitations.

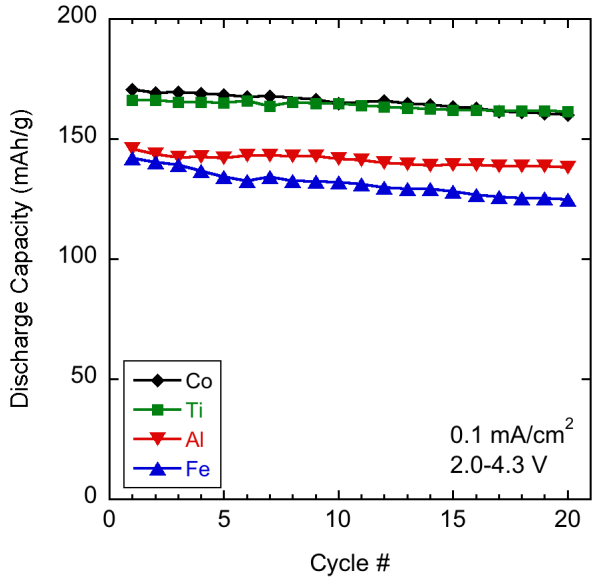

Figure 3.3: Discharge capacities of $Li/LiNi_{1/3}Co_{1/4}M_{1/12}Mn_{1/3}O_2$ (M=Ti, Fe, Al, and Co) cells. Cycling was limited to 2.0-4.3 V vs. Li/Li^+ at a constant charge and discharge current density of 0.1 mA/cm^2.

Differential capacity plots of the first cycles of the $Li/LiNi_{1/3}Co_{1/4}M_{1/12}Mn_{1/3}O_2$ (M=Co, Ti, Al, Fe) cells are presented in Figure 3.4. All of the dQ/dV plots for the substituted materials show increases in the peak charge and discharge potentials and broader peaks compared to those of the parent compound, indicating that the voltage profiles are modified. This not only serves as a strong indicator that the substitutive elements were incorporated into the host lattice but also shows the effects on the electrochemical potential of lithium ion insertion and removal. The shift is greatest for the aluminum substituted

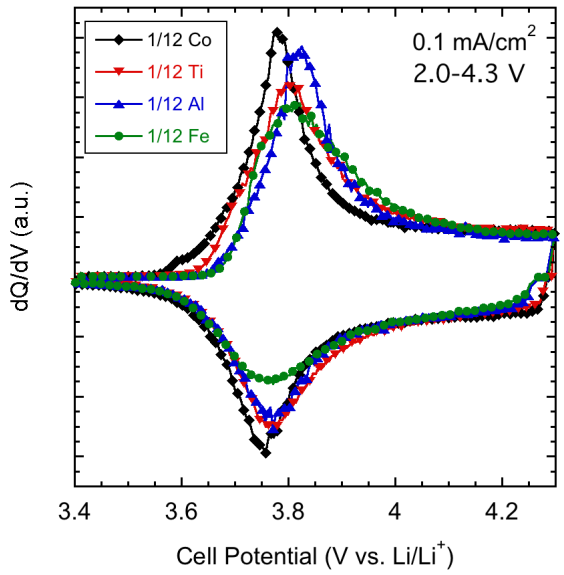

Figure 3.4: Differential capacity plots of the first cycles of $Li/LiNi_{1/3}Co_{1/4}M_{1/12}Mn_{1/3}O_2$ (M=Ti, Fe, Al, and Co) cells. Cycling was limited to 2.0-4.3 V vs. Li/Li^+ at a constant charge and discharge current density of 0.1 mA/cm^2.

material (approximately 50 mV) and has been predicted by *ab-initio* calculations.[24, 38-40] In general, the increase in discharge peak potential is less pronounced than for charge, with all of the substituted materials delivering peak capacity near 3.77 V compared to 3.75 V for the unsubstituted analog. The increase in charge potential explains the lower-than-expected practical capacities obtained for several of the substituted materials using a 4.3

V cutoff. Increasing the charge cutoff potential to 4.7 V allows significantly higher

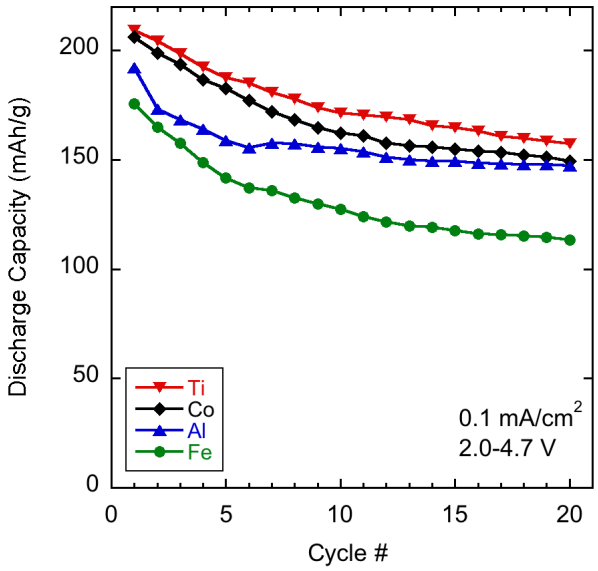

Figure 3.5: Discharge capacities of $Li/LiNi_{1/3}Co_{1/4}M_{1/12}Mn_{1/3}O_2$ (M=Ti, Fe, Al, and Co) cells. Cycling was limited to 2.0-4.7 V vs. Li/Li^+ at a constant charge and discharge current density of 0.1 mA/cm^2.

utilization of the electrode active materials (Figure 3.5) but also results in faster capacity fading due either to instability of the oxidized active materials or irreversible oxidation of the electrolyte solutions.

The capacities of $Li/LiNi_{1/3}Co_{1/4}M_{1/12}Mn_{1/3}O_2$ (M=Co, Ti, Al, Fe) cells as a function of current density are shown in Figure 3.6. Interestingly, substitution with aluminum or titanium leads to improved rate capability compared to $LiNi_{1/3}Co_{1/3}Mn_{1/3}O_2$, most noticeably at higher current densities. The performance of $LiNi_{1/3}Co_{1/4}Ti_{1/12}Mn_{1/3}O_2$ is particularly notable, delivering ~95 mAh/g at 6 mA/cm^2 (~3C rate). The main structural difference between $LiNi_{1/3}Co_{1/3}Mn_{1/3}O_2$ and $LiNi_{1/3}Co_{1/4}Ti_{1/12}Mn_{1/3}O_2$ is the increase in the *c* parameter and lithium interslab space caused by partial replacement of Co^{3+} with the Ti^{4+} ion. The increased lithium slab dimension leads to enhanced lithium ion diffusion through the adjacent tetrahedral vacancy.[16] In contrast, cells with $LiNi_{1/3}Co_{1/4}Fe_{1/12}Mn_{1/3}O_2$ have very poor rate performance with a pronounced reduction in delivered capacity upon even minor increases in the discharge current density.

Figure 3.7 shows first cycles of lithium cells containing $LiNi_{1/3}Co_{1/4}M_{1/12}Mn_{1/3}O_2$,

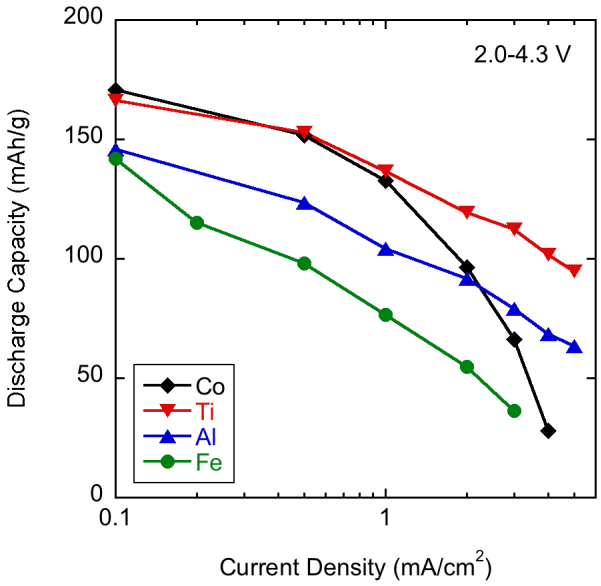

Figure 3.6: Rate capabilities of $Li/LiNi_{1/3}Co_{1/4}M_{1/12}Mn_{1/3}O_2$ (M=Ti, Fe, Al, and Co) cells. Cycling was limited to 2.0-4.3 V and a constant charge current density of 0.1 mA/cm^2 was used.

(M=Co, Ti, Al, Fe) at 0.1 mA/cm^2. The irreversible capacity, defined as the difference in first charge and discharge capacity with respect to the discharge capacity, varies with the nature of the substituent and is lowest for M=Co and highest for M=Fe. High irreversible capacities are undesirable as they can considerably reduce practical energy densities. In non-stoichiometric lithium nickel oxides ($Li_{1-z}Ni_{1+z}O_2$) large irreversible capacities have been associated with the oxidation of Ni^{2+} ions residing within lithium layers. The oxidation of the extra nickel ions leads to the local collapse of the lithium layer inhibiting the re-intercalation of adjacent lithium vacancies except at very low rates.[41, 42] Choi and Manthiram suggest that a parasitic reaction between the active material and electrolyte may be responsible for the irreversibility in cells containing $LiNi_{1/3}Co_{1/3}Mn_{1/3}O_2$.[43] In the same system, Tsai *et al.* discovered a correlation between irreversible capacity and the inability to reduce all of the Ni^{4+} to Ni^{2+} using X-ray absorption near-edge spectroscopy (XANES).[35] Alternatively, a sudden decrease in lithium ion mobility at the end of discharge has been observed in $LiNi_{1-y}Fe_yO_2$ materials.[44] An associated drop in potential inhibits the

complete reinsertion of lithium into the structure, although an over-lithiated surface phase

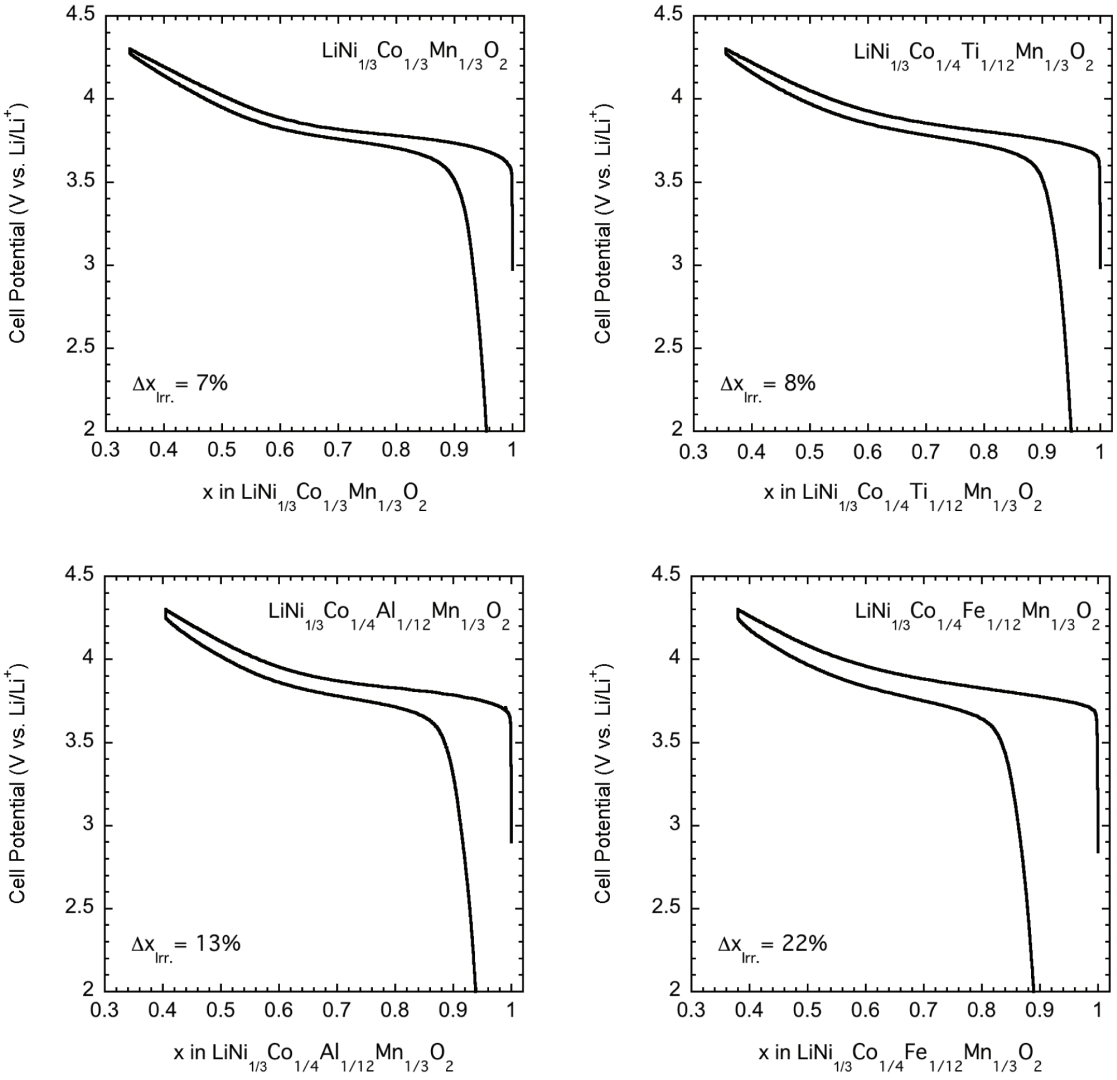

Figure 3.7: First cycles of $Li/LiNi_{1/3}Co_{1/4}M_{1/12}Mn_{1/3}O_2$ (M=Ti, Fe, Al, and Co) cells at 0.1 mA/cm^2 between 2.0 and 4.3 V vs. Li/Li^+. Irreversible capacities are defined in the text.

may be formed at potentials near 2 V.

The irreversible capacities observed for mixed metal systems are dependent upon the voltage limits used and synthesis method, and can vary substantially for identical compositions. For example, a 12.9% irreversible capacity is observed in cells with $LiNi_{1/3}Co_{1/3}Mn_{1/3}O_2$ materials produced via oxalate co-precipitation[1] but only 7.0(4)% for the material in this study, typical of those made by glycine-nitrate combustion.[45] Titanium

substitution does not change this significantly, but aluminum-containing materials suffer from a 13(4)% loss in capacity during the first cycle. The irreversible capacity of the iron substituted material increases to 23(1)% possibly reflecting the inhibited kinetics associated with the decreased *c/3a* ratio of this material and the oxidation of Ni^{2+} in the lithium layers.

Cycling cells to 4.7 V results in a substantial increase in irreversible capacity for all of the positive electrode materials. In cells containing $LiNi_{1/3}Co_{1/3}Mn_{1/3}O_2$, it doubles to 14(1)%, while there is a nearly three-fold increase to 23(2)% for those with $LiNi_{1/3}Co_{1/4}Ti_{1/12}Mn_{1/3}O_2$, and 31(1)% for $LiNi_{1/3}Co_{1/4}Fe_{1/12}Mn_{1/3}O_2$. Interestingly, for Li/ $LiNi_{1/3}Co_{1/4}Al_{1/12}Mn_{1/3}O_2$ cells, there is a relatively small increase in irreversible capacity from 13(4)% using a 4.3 V cutoff to just 17(6)% using 4.7 V. In all cases no evidence of second phase formation between 2.0 and 4.3 or 4.7 V was observed.

3.4.2 $LiNi_{1/3}Co_{1/3-y}Al_yMn_{1/3}O_2$ ($1/3 \geq y \geq 0$)

X-ray powder diffraction patterns (Figure 3.8) show that highly crystalline, single-phase materials are formed for aluminum contents between $0 \leq y \leq 1/4$. For y=1/3, a second phase of γ-$LiAlO_2$ is detected, consistent with previous experimental work [24] and as predicted by Buta *et al.* using *ab initio* methods[46] for materials synthesized above 600° C. Refinement of the X-ray patterns indicate that aluminum substitution has a negligible effect on the *a* unit cell parameter but that there is a systematic expansion of the *c* unit cell parameter with increasing aluminum contents (Table 3.1). Correspondingly, the *c/3a* ratio increases to 1.665 at y=1/3 (1.664 for the single phase material at y=1/4) indicating an improved lamellar structure upon the incorporation of aluminum. This is further substantiated by the increased splitting between the 018 and 110 peaks in the XRD patterns and the shifts in the 003 peaks (Figure 3.8 insets). The lithium slab dimension increases from 2.59 Å at y=0 to 2.66 Å at y=1/3 implying that the incorporation of aluminum leads to a decrease in the anti-site defect concentration.[47] In contrast, Hu *et al.*[24] observed an

increase in anti-site defects at elevated aluminum contents. However, the materials

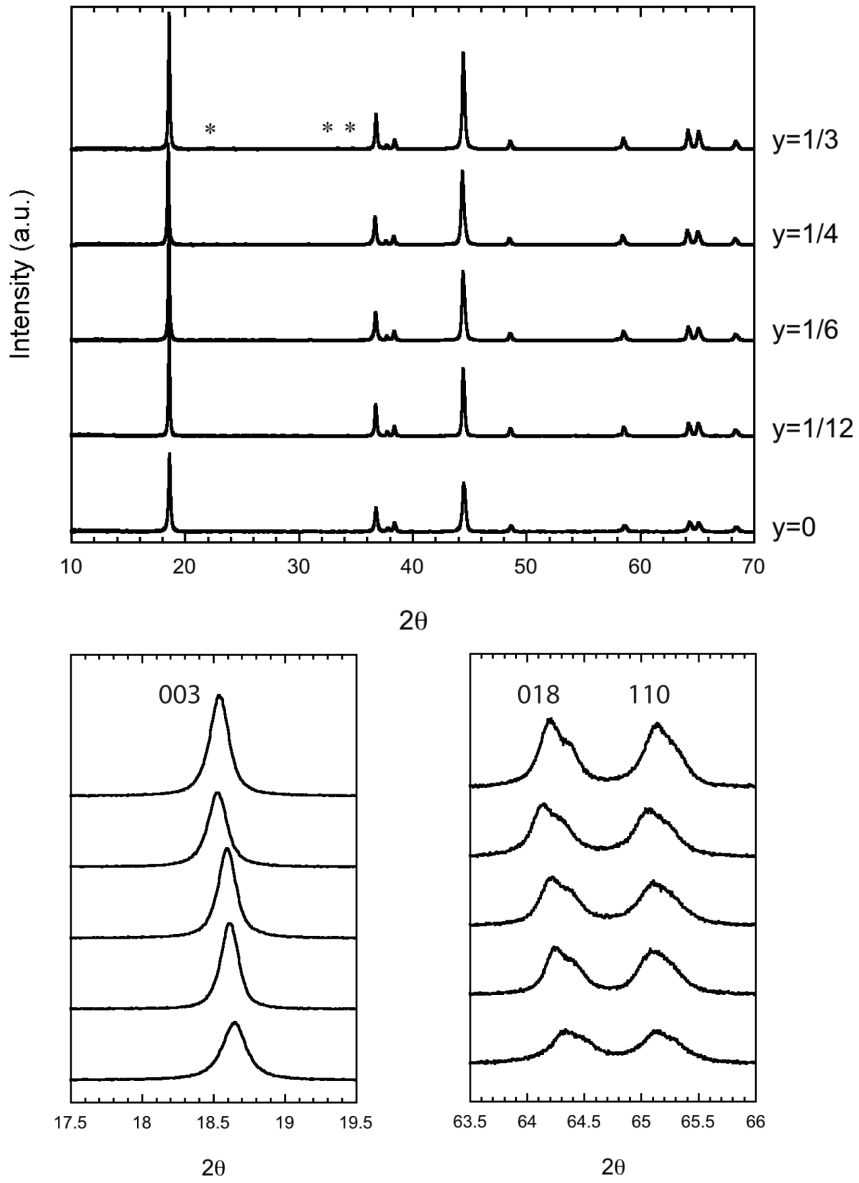

Figure 3.8: Powder XRD diffraction patterns of $LiNi_{1/3}Co_{1/3-y}Al_yMn_{1/3}O_2$, ($0 \leq y \leq 1/3$) compounds. All materials were single phase except y=1/3, in which an impurity of γ-$LiAlO_2$ (*) is observed. Insets show the consistent shift in the 003 peak and increased 018/110 peak splitting. This implies improved lamellar character with increased aluminum content.

in this study were heated to 800° C for a relatively short time (4 hours) rather than 900° C. At the higher temperature, there is reduced solubility of aluminum[46] and more substantial mixing between lithium in the *3b* site and transition metals in the *3a* position.

The discharge capacities of $Li/LiNi_{1/3}Co_{1/3-y}Al_yMn_{1/3}O_2$ ($0 \leq y \leq 1/3$) cells cycled between 2.0 and 4.3 V at a low current density (0.1 mA/cm^2) are presented in Figure 3.9. There is a systematic decrease in the specific capacity as the aluminum content is increased, as found previously.[24] The source of this phenomenon becomes apparent when looking at the differential capacity plots (Figure 3.10). Upon aluminum substitution there is a rise in the oxidation potential, as predicted by first principle calculations, due to the increased oxygen participation in the redox reaction.[40] At y=1/3, the peak oxidation potential is located at 3.97 V and is ~200 mV greater than for the parent compound (3.75 V). Thus the potential required to remove a significant fraction of the lithium from the aluminum substituted materials is above the electrolyte oxidative stability threshold of about 4.3V vs. Li/Li^+, resulting in reduced practical capacity.

Cycling to 4.7 V leads to higher capacities for all the cells containing $LiNi_{1/3}Co_{1/3-y}Al_yMn_{1/3}O_2$, ($0 \leq y \leq 1/3$) electrodes (Figure 3.11), although the amount of improvement is dependent upon the exact composition. For example, there is an increase of only 4% for cells containing $LiNi_{1/3}Co_{1/6}Al_{1/6}Mn_{1/3}O_2$ active materials when cycling to 4.7 (145 mAh/g)

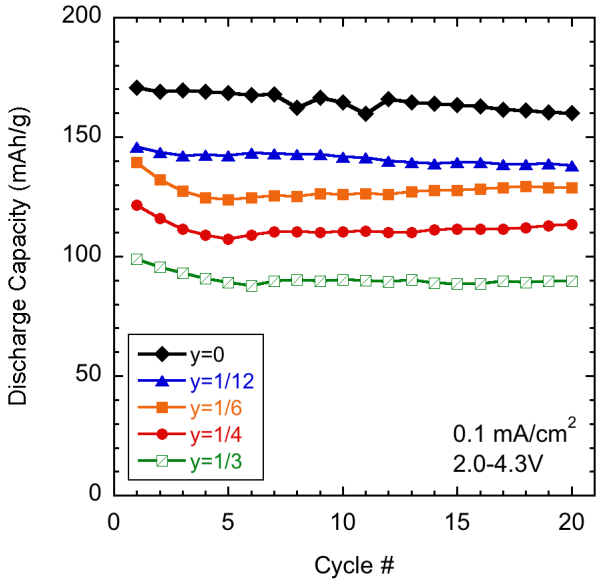

Figure 3.9: Discharge capacities of $Li/LiNi_{1/3}Co_{1/3-y}Al_yMn_{1/3}O_2$, ($0 \leq y \leq 1/3$) cells. Cycling was limited to 2.0-

4.3 V vs. Li/Li^+ at a constant charge and discharge current density of 0.1 mA/cm^2.

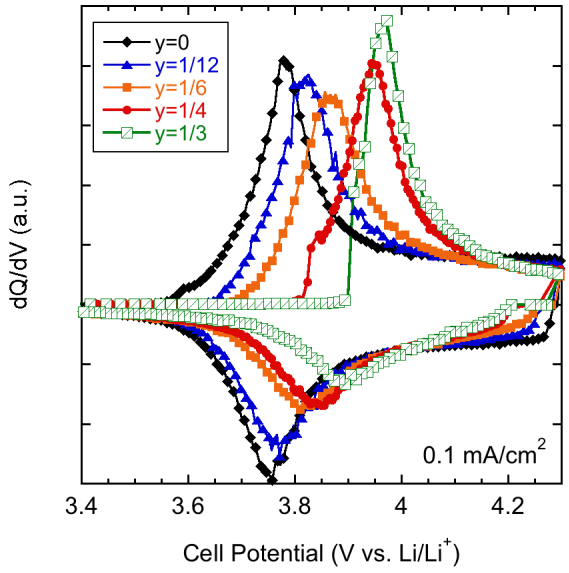

Figure 3.10: Differential capacity plots of the first cycles of $Li/LiNi_{1/3}Co_{1/3-y}Al_yMn_{1/3}O_2$, ($0 \le y \le 1/3$) cells. Current density was 0.1 mA/cm^2 in the potential range 2.0-4.3 V vs. Li/Li^+.

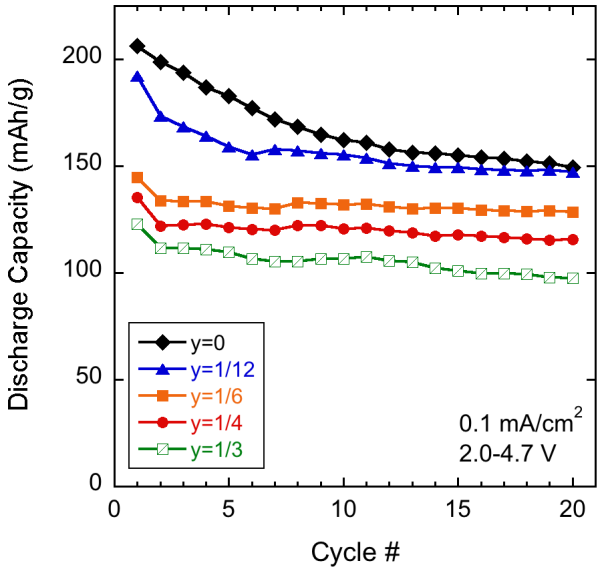

Figure 3.11: Discharge capacities of $Li/LiNi_{1/3}Co_{1/3-y}Al_yMn_{1/3}O_2$, ($0 \le y \le 1/3$) cells. Cycling was limited to 2.0-4.7 V vs. Li/Li^+ at a constant charge and discharge current of 0.1 mA/cm^2.

rather than 4.3 V (139 mAh/g). The higher oxidation potential has a more pronounced effect at all other substitution levels with y=0 (206 mAh/g) delivering 21% more capacity, y=1/12 (192 mAh/g) 32%, y=1/4 (136 mAh/g) 12%, and y=1/3 (123 mAh/g) 24%. Utilization

is increased to 74% of the theoretical capacity for materials with y<1/6 cycled to 4.7 V. However, for materials with y≥1/6 this decreases to 60%, reflecting the shift in the voltage profile caused by the increased aluminum content. Although capacity and utilization are lower, the cycling behavior improves. At substitution levels of y≥1/6 virtually no capacity fade is observed after the first cycle. The increased cycling stability may be due, in part, to the inability to completely remove all of the lithium from the structure even at high potentials. While this lowers the energy density of these materials, it is compensated in part by the increased average cell potential and has been shown to improve the thermal stability of the delithiated oxide.[37, 48, 49]

As the rate data presented in Figure 3.12 shows, the reduced anti-site defect concentration and increase in the lithium slab dimensions (Table 3.1) associated with aluminum substitution lead to positive electrode materials with better rate capabilities than the parent compound. All of the $LiNi_{1/3}Co_{1/3-y}Al_yMn_{1/3}O_2$ compounds retain a significantly greater portion of the discharge capacity obtained at low rates when the current is increased, independent of the value of y. However, the decreased capacity obtained below

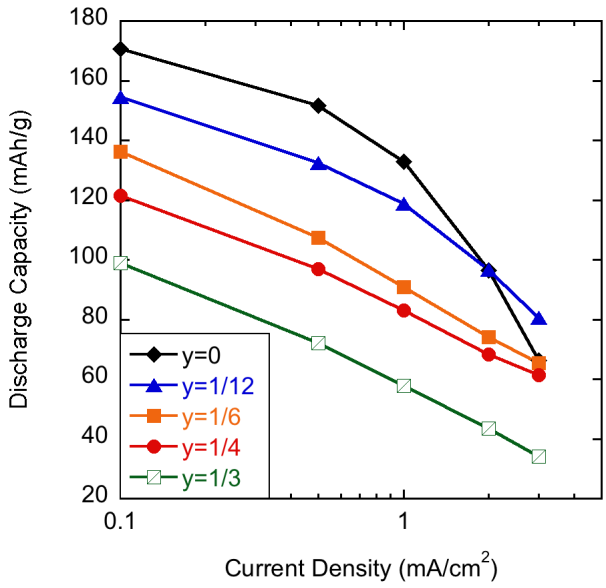

Figure 3.12: Rate capabilities of $Li/LiNi_{1/3}Co_{1/3-y}Al_yMn_{1/3}O_2$, ($0 \leq y \leq 1/3$) cells. Cycling was limited to 2.0-4.3

V and a constant charge current density of 0.1 mA/cm^2 was used.

4.3 V means that the advantages are most evident only for low substitution levels and high current densities. In addition, the increase in first cycle irreversible capacity seen in lithium cells as the aluminum content in $LiNi_{1/3}Co_{1/3-y}Al_yMn_{1/3}O_2$ is raised (Figure 3.13) also suggests that y should be kept low for the ideal high rate, high energy system.

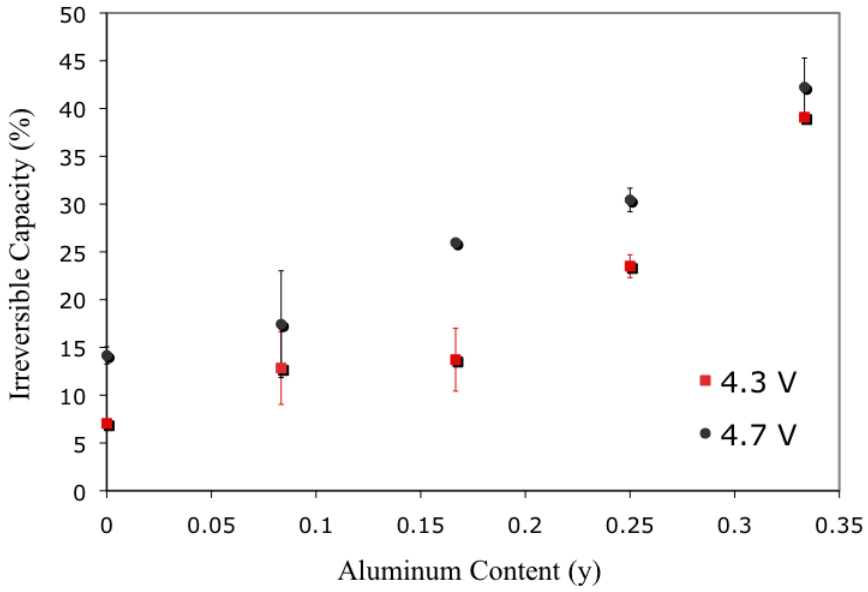

Figure 3.13:. Irreversible capacities of Li/$LiNi_{1/3}Co_{1/3-y}Al_yMn_{1/3}O_2$, ($0 \le y \le 1/3$) cells cycled to a charge cutoff potential of either 4.3 or 4.7 V (0.1 mA/cm^2 current density).

3.5 Conclusions

Several new materials based on the $LiNi_{1/3}Co_{1/3-y}M_yMn_{1/3}O_2$ (M=Co, Ti, Al, Fe) system have been synthesized using the glycine nitrate combustion method. The electrochemical behavior in lithium cells of electrodes based on these materials are substantially altered compared to the $LiNi_{1/3}Co_{1/3}Mn_{1/3}O_2$ parent. These differences can be directly attributed to changes in the structural characteristics induced by the substitutions. $LiNi_{1/3}Co_{1/4}Fe_{1/12}Mn_{1/3}O_2$ exhibits lower capacity and inferior rate capabilities due to kinetic limitations resulting from an increase in the anti-site cation defect concentration as implied

by a reduced *c/3a* ratio. Phase pure $LiNi_{1/3}Co_{1/3-y}Al_yMn_{1/3}O_2$ compounds are formed for $0 \leq y \leq 1/4$ but a γ-$LiAlO_2$ impurity is observed for $y=1/3$. Although aluminum substitution results in decreased capacity between 4.3 and 2.0 V when electrodes are discharged in lithium cells, capacity retention and rate capability is substantially improved. This can be attributed to decreased anti-site mixing and an increased lithium slab dimension compared to $LiNi_{1/3}Co_{1/3}Mn_{1/3}O_2$. The composition, $LiNi_{1/3}Co_{1/4}Ti_{1/12}Mn_{1/3}O_2$ is particularly noteworthy as a high capacity, high rate positive electrode material with good stability and very low irreversible capacity loss.

3.6 Acknowledgments

This work was supported by the Assistant Secretary for Energy Efficiency and Renewable Energy, Office of Vehicle Technologies of the U.S. Department of Energy under Contract No. DE-AC02-05CH11231.

3.7 References

1. Wilcox, J., S. Patoux, and M. Doeff, *Structure and Electrochemistry of LiNi(1/3) Co(1/3-y)M(y)Mn(1/3)O(2) (M=Ti, Al, Fe) Positive Electrode Materials.* Journal of the Electrochemical Society. **Submitted, August 2008**.

2. Cho, T.-H., Y. Shiosaki, and H. Noguchi, *Preparation and characterization of layered LiMn(1/3)Ni(1/3)Co(1/3)O(2) as a cathode material by an oxalate co-precipitation method.* Journal of Power Sources, 2006. **159**(2): p. 1322-1327.

3. B. Ammundsen, J.P., *Novel Lithium-Ion Cathode Materials Based on Layered Manganese Oxides*. Advanced Materials, 2001. **13**(12-13): p. 943-956.

4. Yabuuchi, N., et al., *Solid-State Chemistry and Electrochemistry of LiCo(1/3)Ni(1/3) Mn(1/3)O(2) for Advanced Lithium-Ion Batteries.* Journal of the Electrochemical Society, 2005. **152**(7): p. A1434-A1440.

5. Ohzuku, T. and Y. Makimura, *Layered lithium insertion material of LiCo(1/3)Ni(1/3) Mn(1/3)O(2) for lithium-ion batteries.* Chemistry Letters, 2001(7): p. 642-643.

6. Yabuuchi, N. and T. Ohzuku, *Novel lithium insertion material of LiCo(1/3)Ni(1/3) Mn(1/3)O(2) for advanced lithium-ion batteries.* Journal of Power Sources, 2003. **119-121**: p. 171-174.

7. Koyama, Y., et al., *Solid-State Chemistry and Electrochemistry of LiCo(1/3)Ni(1/3) Mn(1/3)O(2) for Advanced Lithium-Ion Batteries*. Journal of the Electrochemical Society, 2004. **151**(10): p. A1551.

8. Yabuuchi, N., Y. Makimura, and T. Ohzuku, *Solid-State Chemistry and Electrochemistry of LiCo(1/3)Ni(1/3)Mn(1/3)O(2) for Advanced Lithium-Ion Batteries.* Journal of The Electrochemical Society, 2007. **154**(4): p. A314-A321.

9. Belharouak, I., et al., *LiNi(1/3)Co(1/3)Mn(1/3)O(2) as a suitable cathode for high power applications.* Journal of Power Sources, 2003. **123**(2): p. 247-252.

10. Belharouak, I., et al., *Safety characteristics of LiNi(0.8)Co(0.15)Al(0.05)O(2) and LiNi(1/3)Co(1/3)Mn(1/3)O(2).* Electrochemistry Communications, 2006. **8**(2): p. 329-335.

11. Lu, Z.H., et al., *Synthesis, structure, and electrochemical behavior of Li[Ni(x)Li(1/3-2x/3)Mn(2/3-x/3)]O(2).* Journal of the Electrochemical Society, 2002. **149**(6): p. A778-A791.

12. Ohzuku, T. and Y. Makimura, *Layered lithium insertion material of LiNi(1/2) Mn(1/2)O(2): A possible alternative to LiCoO(2) for advanced lithium-ion batteries.* Chemistry Letters, 2001(8): p. 744-745.

13. Makimura, Y. and T. Ohzuku, *Lithium insertion material of LiNi(1/2)Mn(1/2)O(2) for advanced lithium-ion batteries.* Journal of Power Sources, 2003. **119**: p. 156-160.

14. Shannon, R., *Revised effective ionic radii and systematic studies of interatomic distances in halides and chalcogenides.* Acta Crystallographica Section A, 1976. **32**(5): p. 751-767.

15. Wu, E.J., P.D. Tepesch, and G. Ceder, *Size and charge effects on the structural stability of LiMO(2) (M=transition metal) compounds.* Philosophical Magazine B-Physics of Condensed Matter Statistical Mechanics Electronic Optical and Magnetic Properties, 1998. **77**(4): p. 1039-1047.

16. Kang, K. and G. Ceder, *Factors that affect Li mobility in layered lithium transition metal oxides.* Physical Review B (Condensed Matter and Materials Physics), 2006. **74**(9): p. 094105-7.

17. Ngala, J.K., et al., *The synthesis, characterization and electrochemical behavior of the layered LiNi(0.4)Mn(0.4)Co(0.2)O(2) compound.* Journal of Materials Chemistry, 2004. **14**(2): p. 214-220.

18. Yoshio, M., et al., *Preparation and properties of LiCo(y)Mn(x)Ni(1-x-y)O(2) as a cathode for lithium ion batteries.* Journal of Power Sources, 2000. **90**(2): p. 176-181.

19. Manthiram, A., J. Choi, and W. Choi, *Factors limiting the electrochemical performance of oxide cathodes.* Solid State Ionics, 2006. **177**(26-32): p. 2629-2634.

20. Kang, K.S., et al., *Electrodes with high power and high capacity for rechargeable lithium batteries.* Science, 2006. **311**(5763): p. 977-980.

21. Hewston, T.A. and B.L. Chamberland, *A Survey of first-row ternary oxides LiMO(2) (M = Sc-Cu).* Journal of Physics and Chemistry of Solids, 1987. **48**(2): p. 97-108.

22. Reimers, J.N., et al., *Structure and electrochemistry of Li(x)Fe(y)Ni(1-y)O(2).* Solid State Ionics, 1993. **61**(4): p. 335-344.

23. Meng, Y.S., et al., *Combining ab initio computation with experiments for designing new electrode materials for advanced lithium batteries: LiNi(1/3)Fe(1/6) Co(1/6)Mn(1/3)O(2).* Journal of the Electrochemical Society, 2004. **151**(8): p. A1134-A1140.

24. Hu, S.-K., et al., *Effect of Co content on performance of LiAl(1/3-x)Co(x)Ni(1/3) Mn(1/3)O(2) compounds for lithium-ion batteries.* Journal of Power Sources, 2006. **160**(2): p. 1287-1293.

25. Ganesan, M., et al., *Synthesis and characterization of tetravalent titanium (Ti4+) substituted LiCoO(2) for lithium-ion batteries.* Materials Science and Engineering: B, 2006. **131**(1-3): p. 203-209.

26. Ha, H.-W., K.H. Jeong, and K. Kim, *Effect of titanium substitution in layered LiNiO(2) cathode material prepared by molten-salt synthesis.* Journal of Power Sources, 2006. **161**(1): p. 606-611.

27. Tsuda, M., et al., *Electrode performance of layered LiNi(0.5)Ti(0.5)O(2) prepared by ion exchange.* Journal of Power Sources, 2005. **144**(1): p. 183-190.

28. Liu, H., et al., *Structural, electrochemical and thermal properties of LiNi(0.8-y)Ti(y) Co(0.2)O(2) as cathode materials for lithium ion battery.* Electrochimica Acta, 2004. **49**(7): p. 1151-1159.

29. Arai, H., M. Tsuda, and Y. Sakurai, *Lithium nickelate electrodes with enhanced high-temperature performance and thermal stability.* Journal of Power Sources, 2000. **90**(1): p. 76-81.

30. Chick, L.A., et al., *Glycine-nitrate combustion synthesis of oxide ceramic powders.* Materials Letters, 1990. **10**(1-2): p. 6-12.

31. Wilcox, J. and M. Doeff, *Characterization and Electrochemical Performance of Substituted LiNi(0.4)Co(0.2-y)Al(y)Mn(0.4)O(2) (0<y<0.2) Cathode Materials.* ECS Transactions, 2008. **11**(29): p. 27-33.

32. Jung, C.H., et al., *Synthesis of Li(2)TiO(3) ceramic breeder powders by the combustion process.* Journal of Nuclear Materials, 1998. **253**(1-3): p. 203-212.

33. Rodriguez-Carvajal, J., *Recent advances in magnetic structure determination by neutron powder diffraction.* Physica B: Condensed Matter, 1993. **192**(1-2): p. 55-69.

34. Choi, J. and A. Manthiram, *Role of chemical and structural stabilities on the electrochemical properties of layered LiNi(1/3)Mn(1/3)Co(1/3)O(2) cathodes.* Journal of the Electrochemical Society, 2005. **152**(9): p. A1714-A1718.

35. Tsai, Y.W., et al., *In-situ X-ray absorption spectroscopic study on variation of electronic transitions and local structure of LiNi(1/3)Co(1/3)Mn(1/3)O(2) cathode material during electrochemical cycling.* Chemistry of Materials, 2005. **17**(12): p. 3191-3199.

36. Patoux, S., M. Dolle, and M.M. Doeff, *Layered Manganese Oxide Intergrowth Electrodes for Rechargeable Lithium Batteries. 2. Substitution with Al.* Chem. Mater., 2005. **17**(5): p. 1044-1054.

37. Albrecht, S., et al., *Electrochemical and thermal behavior of aluminum- and magnesium-doped spherical lithium nickel cobalt mixed oxides Li(1-x)Ni(1-y-z) Co(y)M(z)O(2) (M = Al, Mg).* Journal of Power Sources, 2003. **119**: p. 178-183.

38. Ohzuku, T., K. Nakura, and T. Aoki, *Comparative study of solid-state redox reactions of LiCo(1/4)Ni(3/4)O(2) and LiAl(1/4)Ni(3/4)O(2) for lithium-ion batteries.* Electrochimica Acta, 1999. **45**(1-2): p. 151-160.

39. Guilmard, M., et al., *Effects of aluminum on the structural and electrochemical properties of LiNiO(2).* Journal of Power Sources, 2003. **115**(2): p. 305-314.

40. Ceder, G., et al., *Identification of cathode materials for lithium batteries guided by first-principles calculations.* Nature, 1998. **392**(6677): p. 694-696.

41. Peres, J.P., et al., *The relationship between the composition of lithium nickel oxide and the loss of reversibility during the first cycle.* Journal of Physics and Chemistry of Solids, 1996. **57**(6-8): p. 1057-1060.

42. Delmas, C., et al., *On the behavior of the Li(x)NiO(2) system: an electrochemical and structural overview.* Journal of Power Sources, 1997. **68**(1): p. 120-125.

43. Choi, J. and A. Manthiram, *Investigation of the Irreversible Capacity Loss in the Layered LiNi(1/3)Mn(1/3)Co(1/3)O(2) Cathodes.* Electrochemical and Solid-State Letters, 2005. **8**(8): p. C102-C105.

44. Mueller-Neuhaus, J.R., R.A. Dunlap, and J.R. Dahn, *Understanding Irreversible Capacity in Li(x)Ni(1-y)Fe(y)O(2) Cathode Materials.* Journal of The Electrochemical Society, 2000. **147**(10): p. 3598-3605.

45. Patoux, S. and M.M. Doeff, *Direct synthesis of LiNi(1/3)Co(1/3)Mn(1/3)O(2) from nitrate precursors.* Electrochemistry Communications, 2004. **6**(8): p. 767-772.

46. Buta, S., et al., *Phase separation tendencies of aluminum-doped transition-metal oxides LiAl(1-x)M(x)O(2) in the alpha-NaFeO(2) crystal structure.* Journal of the Electrochemical Society, 1999. **146**(12): p. 4335-4338.

47. Guilmard, M., et al., *Structural and electrochemical properties of LiNi(0.70) Co(0.15)Al(0.15)O(2).* Solid State Ionics, 2003. **160**(1-2): p. 39-50.

48. Zhou, F., et al., *The effect of Al substitution on the reactivity of delithiated LiNi(1/3) Mn(1/3)Co(1/3-z)Al(z)O(2) with non-aqueous electrolyte.* Electrochemistry Communications, 2008. **10**(8): p. 1168-1171.

49. Zhou, F., et al., *The Effect of Al Substitution on the Reactivity of Delithiated LiNi(0.5-z)Mn(0.5-z)Al(2z)O(2) with Nonaqueous Electrolyte.* 2008. **11**(9): p. A155-157.

4. The Impact on Structure and Electrochemistry of Aluminum and Iron Substitution in $LiNi_{0.4}Co_{0.2-y}M_yMn_{0.4}O_2$ Materials

4.1 Abstract

A series of novel aluminum and iron substituted layered oxide positive electrode materials with the composition $LiNi_{0.4}Co_{0.2-y}M_yMn_{0.4}O_2$ ($0 \leq y \leq 0.2$) (M=Al, Fe) have been prepared. The impact of substitution on the structure has been examined by both XRD and neutron diffraction experiments. Aluminum substituted materials exhibit slightly increased anti-site defect concentrations, but an increase in the covalency of the transition metal layer leads to the opening of the lithium slab dimension. This results in improved rate performance compared to the parent compound. In contrast, iron substitution inhibits the electrochemical rate performance due to a decrease in the lithium slab dimension. The cycling stability of aluminum containing materials is vastly superior to both the parent material and iron substituted materials.

4.2 Introduction

$LiCoO_2$ has been a mainstay of commercial batteries since first being introduced by Sony in 1991.[1] However, concerns over its high cost, toxicity, and limited abuse tolerance has led to a prolonged effort to find replacement positive electrode materials for the next generation of lithium ion batteries. The mixed transition metal oxides of composition $LiNi_yCo_{1-2y}Mn_yO_2$ have been extensively studied as a means of creating positive electrodes with optimal capacity, rate capability, and thermal/structural stability.[2] In particular, the compositions of $LiNi_{1/3}Co_{1/3}Mn_{1/3}O_2$ and $LiNi_{0.4}Co_{0.2}Mn_{0.4}O_2$ have been widely characterized and are capable of delivering in excess of 160 mAh/g when cycled to 4.2-4.4 V and over 200 mAh/g when charged to potentials above 4.6-4.7 V.[3-6]

The rate performance of an intercalation electrode material operating under standard cycling conditions is largely determined by the rate at which lithium ions can

be transported through the host lattice. Using *ab initio* calculations, the activation energy for lithium ion diffusivity in the lamellar α-$NaFeO_2$ (O3, $R\bar{3}m$) structure has been shown to be highly sensitive to the dimension of the lithium layer.[7] Often termed lithium "slab" spacing, the distance between the oxygen layers bridging the lithium plane determines the compressive stress on a lithium ion residing in the activated tetrahedral site. Increasing the lithium slab dimension lowers the compression on the activated lithium and simultaneously allows the lithium ion to shift away from the face sharing transition metal in the adjacent layer, decreasing the electrostatic repulsion. To maximize the lithium slab spacing and create high rate materials it is critical to minimize the number of anti-site defects where a transition metal, typically nickel, is found to reside on the *3a* site in the lithium plane.[8] Anti-site defects effectively pin the lithium slab spacing below the equilibrium distance and increase the activation energy for lithium diffusion over the entire state of charge of battery operation. Due to its small ionic radius compared to lithium (0.76 Å), cobalt in the low spin state (0.545 Å) minimizes the anti-site defect concentration in both $LiNi_{1-y}Co_yO_2$ and $LiNi_{0.4}Co_{0.2}Mn_{0.4}O_2$ systems and stabilizes the layered structure.[9-12] An alternative strategy is to synthesize the analogous sodium-containing compound and ion exchange the sodium for lithium in a molten salt.[13] The large ionic radius of sodium (1.02 Å) creates a strong driving force for the formation of the lamellar structure and nearly defect free materials have been synthesized in this manner.[12-14]

Aluminum, with an ionic radius of 0.535 Å, is expected to promote the formation of a lamellar phase in a similar manner to cobalt.[15] Recent work on $LiNi_{1/3}Co_{1/3-y}Al_yMn_{1/3}O_2$ reveals that aluminum can be substituted up to y=0.25 without the formation of a γ-$LiAlO_2$ impurity phase.[16] This leads to a small decrease in anti-site defect concentration and a general improvement in rate capability of powders prepared using combustion methods[16-18] While aluminum is electrochemically inactive under normal cycling conditions, substituted materials exhibit an increased charge and discharge potential due to the activation of the oxygen *2p* orbital in the redox reaction.[19] Aluminum substitution into layered oxides has

also been shown to have a positive effect on the thermal abuse tolerances of layered oxide positive electrode materials either by inhibiting lithium extraction at high states of charge or by chemical stabilization of the structure itself.[20-22]

$LiFeO_2$ does not crystallize in the layered α-$NaFeO_2$ structure but either as tetragonally distorted γ-$LiFeO_2$ (*I4$_1$/amd*) or as the cubic α-$LiFeO_2$ (*Fm3m*).[23-26] Both lack a long range diffusion pathway for lithium, and the associated electrochemistry activity is limited.[27, 28] Single phase, $LiNi_{1-x}Fe_xO_2$ and $LiNi_{1/3}Co_{1/6}Fe_{1/6}Mn_{1/3}O_2$ materials with the α-$NaFeO_2$ structure have been synthesized, although the electrochemical performance is generally observed to suffer from lower capacity and impaired cycling properties as compared to the iron-free analogs.[29-31] These characteristics have been correlated with a strong increase in anti-site defect concentration, leading to poor lithium ion transport and increased difficulty in oxidizing nickel in the presence of iron.[32, 33]

The goal of this work is to understand the impact of aluminum and iron substitution on the structure and electrochemistry of $LiNi_{0.4}Co_{0.2-y}M_yMn_{0.4}O_2$ (M=Al, Fe). Changes in structural parameters and in the bonding nature will be related to shifts in the transport properties of both ions and electrons and ultimately to the electrochemical rate performance of the positive electrode materials.

4.3 Experimental Procedures

All materials for this study were synthesized using the glycine nitrate combustion method.[18, 34] The nitrate salts of the desired components, $LiNO_3$ (Mallinckrodt), $Mn(NO_3)_2$ (45-50 wt.% in dilute nitric acid, Sigma Aldrich), $Co(NO_3)_2 \cdot 6H_2O$ (98%, Sigma Aldrich), $Ni(NO_3)_2 \cdot 6H_2O$ (Sigma Aldrich), $Al(NO_3)_3 \cdot 9H_2O$ (98+%, Sigma Aldrich), and $Fe(NO_3)_3 \cdot 9H_2O$ (98% EMD), were dissolved in distilled water in the desired proportions. The total concentration of the transition metal species in solution was generally held around 3.5 M. A slight excess of lithium (5%) was used to compensate for the loss of lithium at elevated temperature during the combustion and sintering processes. Glycine

(98.5+%, Sigma Aldrich) was combined with the nitrate salt solution at a glycine to nitrate ratio of 0.5, corresponding to a flame temperature of approximately 1350° C.[34] Small aliquots (~25 ml) of the nitrate solution were concentrated in a stainless steel combustion chamber on a hot plate until auto ignition occurred. The resulting powders were collected and planetary ball milled for one hour in acetone. After removal of the solvent under flowing nitrogen the powders were heat treated at 800° C for four hours in air (4° C/min ramp rate).

Powder X-ray diffraction (XRD) was performed in the range of 10-70° 2Θ on a Phillips X'Pert diffractometer with an X'celerator detector using Cu Kα radiation. A custom milled polycarbonate powder holder was used so as to avoid any peak overlap associated with the holder material.[16] Neutron diffraction studies were undertaken on the Neutron Powder Diffractometer (NPDF) at the Lujan Neutron Scattering Center at Los Alamos National Laboratory. Samples ranging in size from 1-2 g were sealed in vanadium sample holders and data was collected for 6-12 hours under ambient conditions. Unit cell parameters and site occupancy factors were obtained from a combined XRD/ neutron diffraction Rietveld refinement using the General Structure Analysis System (GSAS/EXPGUI) software package.[35, 36]

Particle morphology studies were conducted using a field emission-scanning electron microscopy (FESEM, Jeol JSM-6340F) and transmission electron microscopy (TEM) (Phillips CM200FEG (field emission gun)) at an accelerating voltage of 200 kV. To prepare samples for TEM, powders were ground in a mortar and pestle in acetone and transferred to a holey carbon grid. Background corrected Fourier transform infrared spectroscopy (FTIR) experiments were conducted on a Thermo Nicolet 6700 on samples composed of mixed active material/potassium bromide pellets, and data was collected in the range of 400-4000 cm^{-1}. Elemental analysis was done by inductively coupled plasma optical emission spectrometry (ICP-OES) (Columbia Analytical Services, Tucson, AZ).

Pressed pellets for conductivity studies were fabricated by uni-axially pressing

~0.5 g of active material to 5 kpsi in a ½" stainless steel die. The pellets were transferred into balloon holders and cold isostatically pressed to 180 kpsi achieving a green density of ~70% of the theoretical density calculated from diffraction. To achieve further densification, pellets were packed in a getter material of the same composition and fired to 800° C for 48 hours in air. The pellet faces were polished flat and parallel and a final density of nearly 75% was obtained. Thin gold electrodes were sputtered onto each face of the pellet using a Bal-Tec SCD 050 sputter coater. AC impedance spectra were obtained using a Solartron Instruments 1260 impedance/gain-phase analyzer at selected temperatures between 25 and 200° C. Conductivities were derived from the intercept of the capacitative arc with the Z' axis in the Nyquist plots.

Laminate composite electrodes comprised of 84 wt.% active material, 8 wt.% poly(vinylidine fluoride) (PVDF, Kureha Chemical Ind. Co. Ltd.), 4 wt.% compressed acetylene black, and 4 wt.% SFG-6 synthetic flake graphite (Timcal Ltd., Graphites and Technologies) were prepared by applying slurries in 1-methyl-2-pyrrolidinone onto carbon coated current collectors (Intelicoat Technologies) by automated doctor blade. After drying in air and in vacuum for at least 24 hours, 1.8 cm^2 electrodes having an average loading of 7-10 mg/cm^2 of active material were punched out. Coin cells (2032) were assembled in a helium filled glove box with lithium metal anodes and 1M $LiPF_6$ in 1:2 ethylene carbonate/dimethyl carbonate (EC/DMC) electrolyte solution (Ferro). Galvanostatic cycling was carried out on an Arbin BT/HSP-2043 cycler between limits of 2.0 and 4.3-4.7 V. All cells were charged at a current density of 0.1 mA/cm^2 independent of the discharge rate. Galvanostatic intermittent titration technique (GITT) experiments were conducted on a Macpile II (Bio-Logic, S.A., Claix, France) automated cycling data recorder between rest potentials of 2.0 and 4.4 V. Current pulses of 0.135 mA lasting 40.5 minutes were used on both charge and discharge corresponding to approximately 3-4% of the total cell capacity being passed on each titration step. A relaxation time of four hours was utilized after each current pulse to allow the cell to equilibrate.

4.4 Results and Discussion

4.4.1 $LiNi_{0.4}Co_{0.2-y}Al_yMn_{0.4}O_2$ ($0 \leq y \leq 0.2$)

All of the powders were determined to be phase pure by XRD analysis over the entire substitution range, $0 \leq y \leq 0.2$ (Figure 4.1). Powders ranged in color from a black/gray at y=0 to slightly red at higher aluminum contents. TEM images of the parent compound, $LiNi_{0.4}Co_{0.2}Mn_{0.4}O_2$, and completely aluminum substituted material, $LiNi_{0.4}Al_{0.2}Mn_{0.4}O_2$, are presented in Figure 4.2. Both types of powders are highly crystalline and consist of small primary particles with an average diameter of approximately 50 nm. This agrees well with the particle size determined during Rietveld refinement (35-50 nm) of XRD patterns. Primary particles are agglomerated into secondary particles that vary in diameter between approximately 250-500 nm (Figure 4.3).

Elemental analysis by ICP-OES indicates that there is a slight excess of lithium in materials with low aluminum contents ($0 \leq y \leq 0.1$) (Table 4.1). The oxygen content was not determined in these experiments and any off-stoichiometry is simply denoted as 2-δ, where

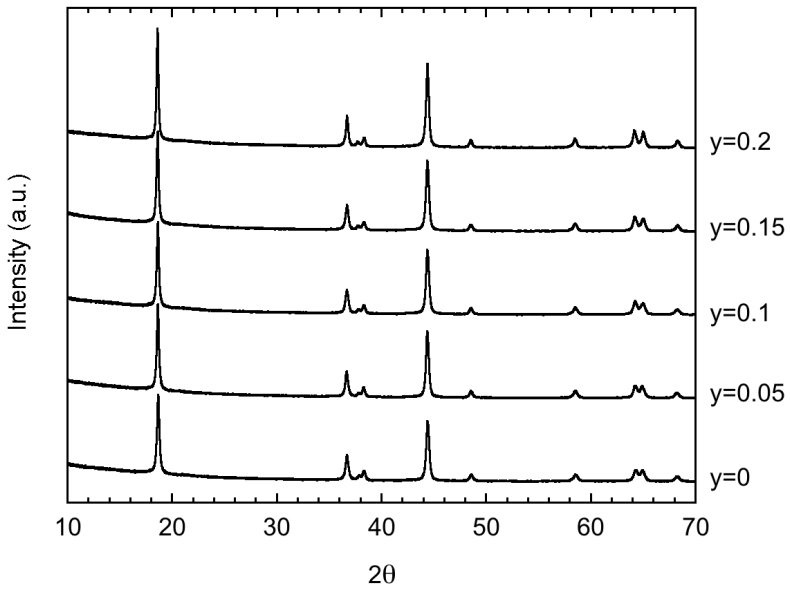

Figure 4.1: Powder XRD patterns of $LiNi_{0.4}Co_{0.2-y}Al_yMn_{0.4}O_2$ ($0 \leq y \leq 0.2$) materials. No impurity phases can be detected and all peaks can be indexed in the $R\bar{3}m$ space group.

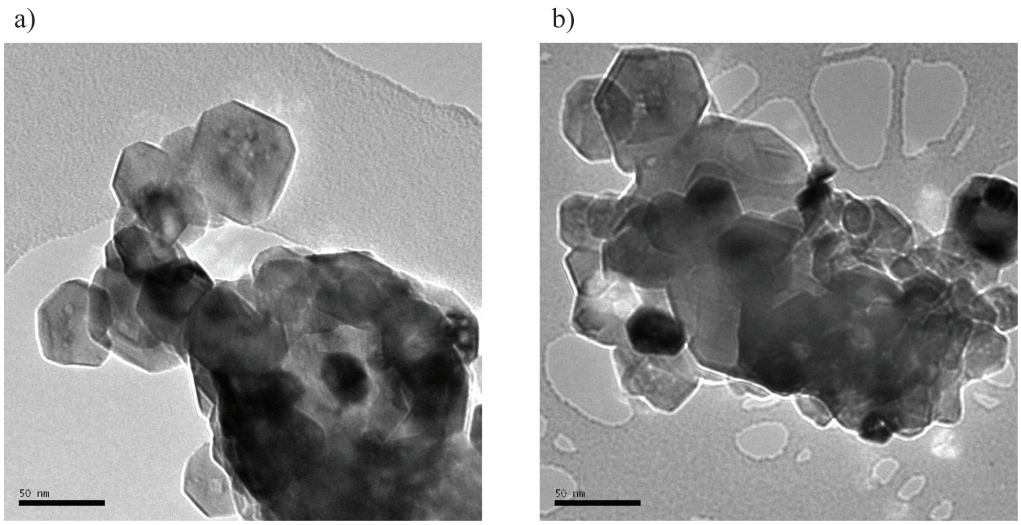

Figure 4.2: TEM images of (a) $LiNi_{0.4}Co_{0.2}Mn_{0.4}O_2$ and (b) $LiNi_{0.4}Al_{0.2}Mn_{0.4}O_2$ active materials. The average particle size is approximately 50 nm regardless of aluminum content and agrees well with the particle size from X-ray and neutron diffraction results (scale bar is 50 nm).

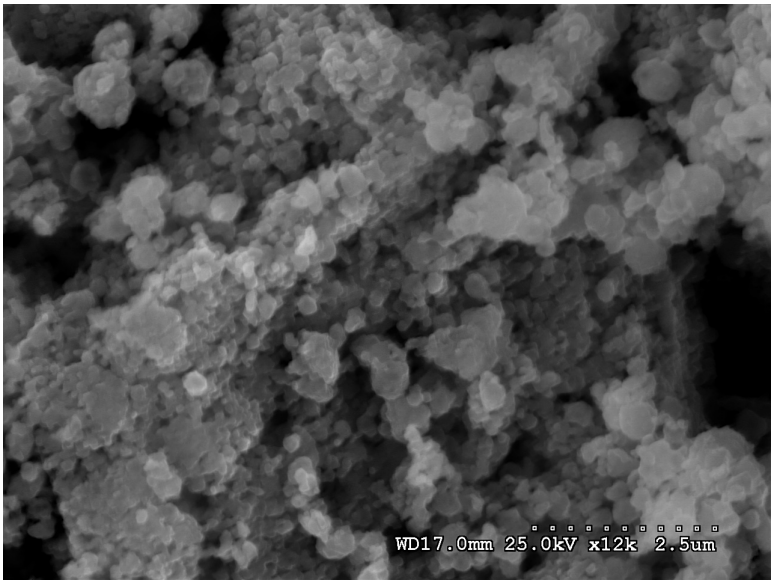

Figure 4.3: SEM image of $LiNi_{0.4}Co_{0.2}Mn_{0.4}O_2$ powder after sintering in air at 800° C. The primary particles are agglomerated into secondary particles ranging in size from 250-500 nm and is representative of all the materials used in this study.

Table 4.1: Nominal and experimentally determined elemental compositions.

Nominal Composition	Experimentally Observed Composition
$LiNi_{0.4}Co_{0.2}Mn_{0.4}O_2$	$Li_{1.08}Ni_{0.4}Co_{0.2}Mn_{0.41}O_{2-\delta}$
$LiNi_{0.4}Co_{0.15}Al_{0.05}Mn_{0.4}O_2$	$Li_{1.07}Ni_{0.4}Co_{0.15}Al_{0.05}Mn_{0.41}O_{2-\delta}$
$LiNi_{0.4}Co_{0.1}Al_{0.1}Mn_{0.4}O_2$	$Li_{1.02}Ni_{0.4}Co_{0.09}Al_{0.09}Mn_{0.41}O_{2-\delta}$
$LiNi_{0.4}Co_{0.05}Al_{0.15}Mn_{0.4}O_2$	$Li_{0.96}Ni_{0.39}Co_{0.5}Al_{0.14}Mn_{0.42}O_{2-\delta}$
$LiNi_{0.4}Al_{0.2}Mn_{0.4}O_2$	$Li_{0.99}Ni_{0.4}Al_{0.19}Mn_{0.41}O_{2-\delta}$

δ can be positive or negative.[1] As the experimental and intended compositions of the active materials are in good agreement, all materials will be referenced by the nominal formula. As can be seen in Figure 4.1, all of the peaks can be indexed in the $R\bar{3}m$ space group over the entire substitution range ($0 \leq y \leq 0.2$). There is no evidence for the formation of a second, γ-$LiAlO_2$ impurity phase, which is commonly found in materials with high aluminum contents heat treated above 600° C.[37, 38] The increased splitting of the 108/110 and 006/012 peaks and the consistent shift in the 003 peaks to larger d-spacings with increasing aluminum content suggest the formation of superior lamellar structures upon substitution.[39]

The results of Rietveld analysis on the combined X-ray and neutron diffraction data sets are presented in Table 4.2 and Figure 4.4. The *a* unit cell parameter shifts inversely with y, contracting 0.1% in the fully substituted material. The *c* unit cell parameter increases 0.03Å (0.2%) over the same range. As the ionic radii of Co^{3+} (0.545 Å) and Al^{3+} (0.535 Å) are very similar, no major shift in the *a* unit cell parameter, which measures the M-M spacing, is expected. The minor shrinkage of the *a* and expansion

[1a] The actual amount of oxygen off-stoichiometry is expected to be very small in these materials, as no major shifts in capacity were observed during electrochemical cycling.

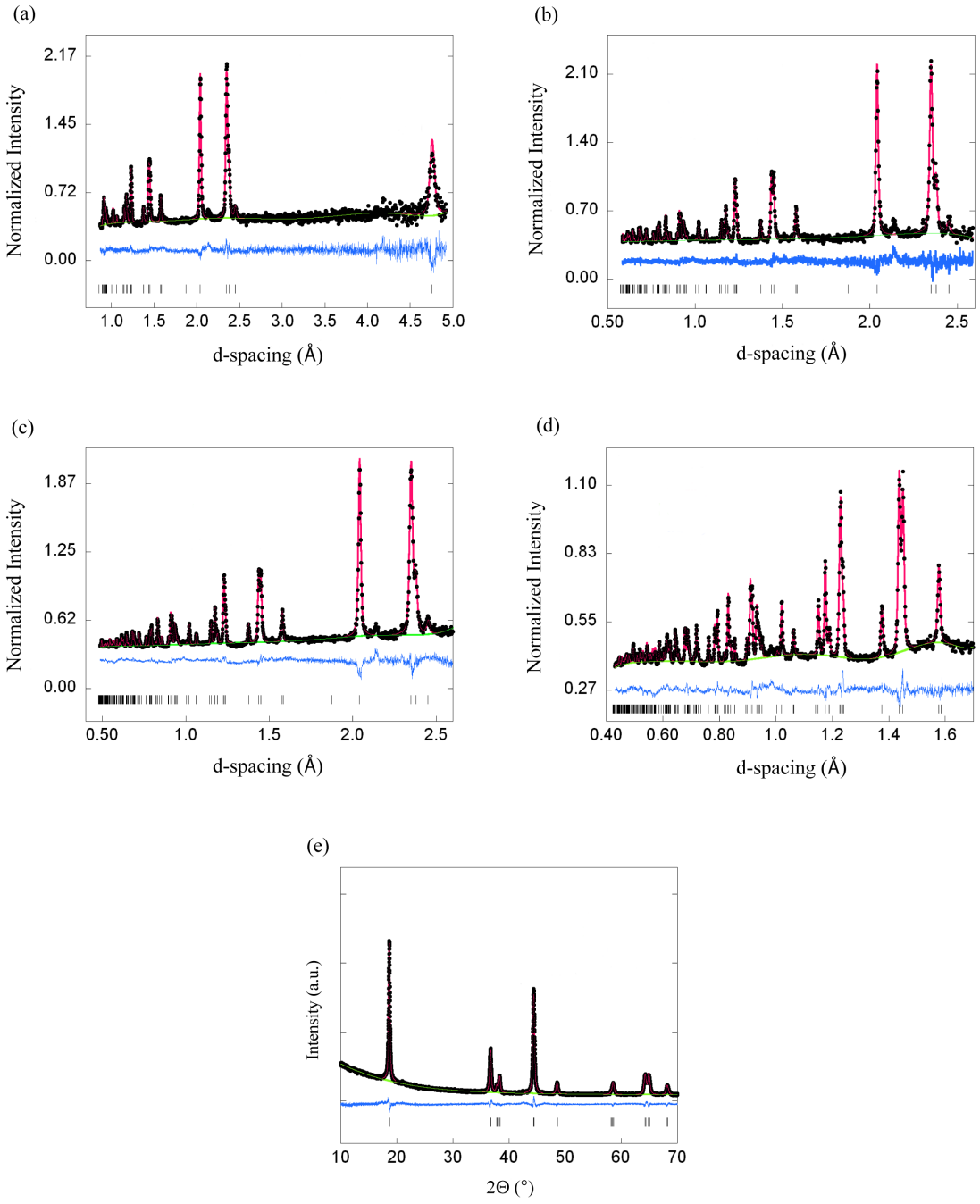

Figure 4.4: The Rietveld refinement results from (a) Bank 1 (40°), (b) Bank 2 (90°), (c) Bank 3 (119°), (c) Bank 4 (148°), and (e) XRD for the composition $LiNi_{0.4}Co_{0.2}Mn_{0.4}O_2$. Black dots and red line represent the experimental data and calculated fit, respectively. Allowed Bragg reflections are marked as black bars and the difference between the experimental data and calculated fit is noted in blue. The structural parameters from the refinement are given in Table 4.2.

Table 4.2: Crystal structure parameters from combined X-ray, neutron diffraction Rietveld refinement.

Al Content (y)	Unit Cell Parameters		z_{Ox}	Unit Cell Volume (Å^3)	Ni_{3a}	I (LiO_2) (Å)	R_{wp} (%)
	a (Å)	c (Å)					
0	2.87238(2)	14.2688(2)	0.24165(3)	101.954(2)	0.066(1)	2.616(1)	4.26
0.05	2.87242(2)	14.2729(2)	0.24153(3)	101.987(2)	0.073(1)	2.621(1)	4.46
0.1	2.87169(3)	14.2854(2)	0.24168(3)	102.024(2)	0.075(1)	2.619(1)	4.92
0.15	2.86970(3)	14.2896(3)	0.24159(3)	101.913(2)	0.074(1)	2.622(1)	4.98
0.2	2.86900(2)	14.2993(2)	0.24159(3)	101.932(2)	0.074(1)	2.624(1)	5.35

of the *c* parameter can be explained on the basis of an increased covalency within the transition metal plane upon aluminum substitution (see next section for the discussion of FTIR results). An increase in covalent bond strength shortens the average M-M bond and pulls electron density away from the bridging oxygen layers. The reduction of electron density on the adjoining oxygen layer weakens the Li-O bond, allowing the expansion of the lithium slab dimension (*I*) and the *c* unit cell parameter. The anti-site defect concentration, measured by the amount of nickel residing on the *3a* position (Ni_{3a}), is lowest in the aluminum free material. The anti-site defect concentration increases less than 1% upon the substitution of aluminum and is statistically unchanged in the range $0.05 \leq y \leq 0.2$. It is important to note the slight increase in the weighted residual criteria of fit (R_{wp}) with aluminum substitution. The source of the shift is not understood at the present time and an effort to define a better structural model is underway. Potential model improvements include the incorporation of local metal clustering and strain effects (see Chapter 8 for a further discussion).

The normalized FTIR spectra as a function of aluminum content are presented in Figure 4.5. The broad adsorption band indicative of materials crystallizing in a rock salt based structure is clearly observed in the 400-700 cm^{-1} range.[40] The broadening of

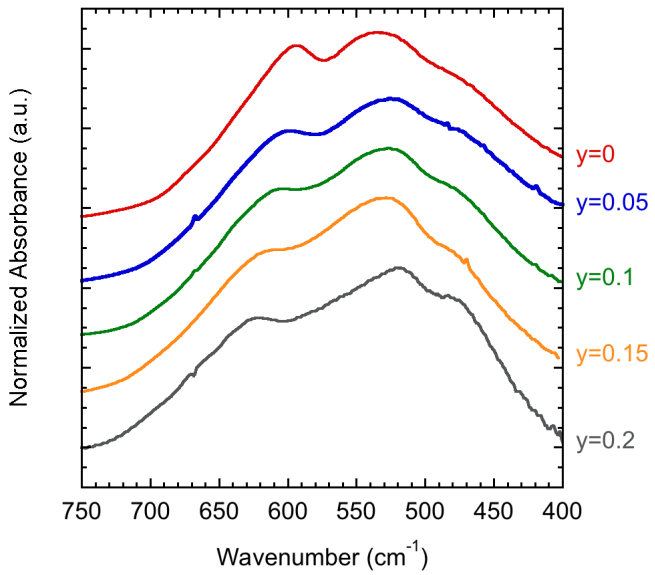

Figure 4.5: FTIR spectra of $LiNi_{0.4}Co_{0.2-y}Al_yMn_{0.4}O_2$ ($0 \leq y \leq 0.2$) layered materials, exhibit the broad adsorption band characteristic of rock-salt derived structures. The three vibrational resonances of the MO_6 structural unit are clearly defined for all samples.

the adsorption band is due to the mixing of nickel, manganese, cobalt, and aluminum in the *3b* position. The homogeneous atomic distribution on a macroscopic scale leads to a dispersion in M-O bond lengths and a distortion in the local octahedral environment in the transition metal plane.[41] Group factor analysis predicts a total of four infrared active vibrational modes for the D_{3d}^5, $R\bar{3}m$ space group with a basis of one formula unit.[42] Of the four active bands there is a general splitting in the frequency response between the MO_6 and LiO_6 components. The three bands associated with the vibrational response of the MO_6 octahedra are located in the 400-650 cm^{-1} region and the single asymmetric vibrational mode of the LiO_6 unit resides between 200-400 cm^{-1}.[43-46] The three high frequency resonance bands of the MO_6 octahedra can be clearly seen in Figure 4.5 and are associated with one asymmetric M-O bond vibration mode (595-625 cm^{-1}) and two O-M-O bending modes (465-480 and 515-535 cm^{-1}).[47] The asymmetric vibrational mode of LiO_6 is beyond the instrument resolution limit, therefore the effects of substitution on the lithium environment cannot be discerned. Upon substitution, the M-O stretching mode

shifts to higher wavenumbers and the intensities of both O-M-O bending modes increase and show relatively minor shifting as previously reported.[48] The observed frequency shifts reflect both changes in the unit cell volume and the increased covalency of the $(Ni_{0.4}Co_{0.2-y}Al_yMn_{0.4})O_2$ layer upon substitution with aluminum.

Aluminum is an electrochemically inactive element under normal cycling conditions; thus, the theoretical capacity shifts inversely with y in $LiNi_{0.4}Co_{0.2-y}Al_yMn_{0.4}O_2$.[19] Assuming complete delithiation upon charge, this value decreases from 279 mAh/g in the parent material (y=0) to 239 mAh/g at full substitution (y=0.2). However, X-ray adsorption spectroscopy experiments,[49, 50] first principle calculations,[51, 52] and iodometric titration results on chemically de-lithiated layered oxides[53] indicate that the $Co^{3+/4+}$ redox couple is not electrochemically active until potentials exceeding 4.3 V, [54] above the oxidative stability limit of common electrolyte solutions. Therefore, practical capacities in cells operated under normal cycling conditions should be minimally impacted as long as no other properties are grossly affected by the aluminum substitution.

The discharge capacities of $Li/LiNi_{0.4}Co_{0.2-y}Al_yMn_{0.4}O_2$ ($0 \leq y \leq 0.2$) coin cells cycled between 2.0 and 4.3 V are presented in Figure 4.6. The unsubstituted compound delivers 163 mAh/g on the first discharge cycle but fades nearly 6% in the first twenty cycles. Materials with y=0.05 have a slightly lower initial discharge capacity of 159 mAh/g but outperform the parent compound after only 15 cycles. Increasing the substitution level to y=0.1, 0.15, and 0.2 leads to further decreases in the initial discharge capacities to 151, 147, and 127 mAh/g respectively. Cycling stability is enhanced for oxides with intermediate aluminum contents ($0.05 \leq y \leq 0.15$) exhibiting an average capacity loss of only 2-3% over the first twenty cycles. The capacity fade of the fully substituted material (y=0.2) is equivalent to that of the parent material (y=0) with a 6% loss.

One possible explanation for the inverse relationship between substitution level and discharge capacity is the elevated average cell potentials of aluminum containing

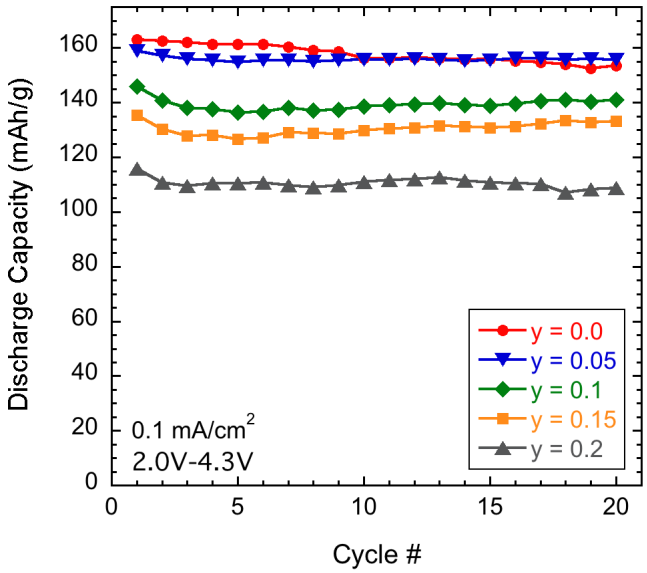

Figure 4.6: Discharge capacities of $Li/LiNi_{0.4}Co_{0.2-y}Al_yMn_{0.4}O_2$ ($0 \leq y \leq 0.2$) cells. Cycling was limited to 2.0-4.3 V vs. Li/Li^+ at a constant charge and discharge current density of 0.1 mA/cm^2.

materials. The shift in the peak oxidation and reduction potentials can be clearly seen in the differential capacity (dQ/dV) plot of materials cycled to 4.3 V (Figure 4.7). The broad peaks are consistent with a topotactically occurring, single-phase reaction in all cases. The peak shape upon charge is relatively unchanged but the potential shifts from 3.795 V for materials with y=0 to a maximum of 3.958 V for a fully substituted material (y=0.2). Upon reduction of the oxides, a similar trend is apparent with discharge potentials increasing from 3.747 V at y=0 to 3.903 V at y=0.2. This phenomenon has been attributed to the increased participation of oxygen *2p* orbitals in the redox reaction and has been observed in other aluminum substituted oxide materials.[17, 19, 38, 48] The increase in cell potential may slightly impact the energy density of these materials but it also limits the amount of lithium that can be removed from the system below the 4.3 V cutoff necessitated by electrolyte stability concerns. The inability to remove all of the lithium from structure has been shown to have a positive effect on the thermal stability of substituted materials, but it also leads to a decrease in electrode utilization at elevated aluminum contents.[20-22]

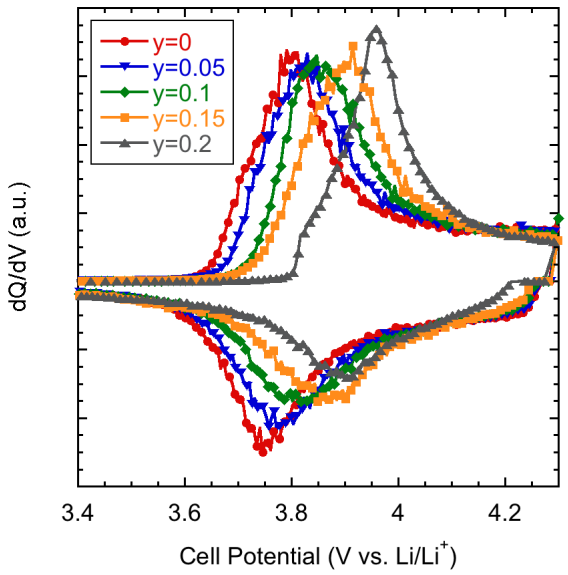

Figure 4.7: Differential capacity plots of the first cycles of Li/$LiNi_{0.4}Co_{0.2-y}Al_yMn_{0.4}O_2$ ($0 \leq y \leq 0.2$) cells. Current density was 0.1 mA/cm^2 in the potential range 2.0-4.3 V vs. Li/Li^+.

The shape of the reduction peak is changed significantly with substitution, simultaneously losing intensity and broadening. This decrease in relative peak height may indicate a shift in the reaction kinetics upon substitution. Additionally, an increase in the ohmic overpotential in materials with high aluminum contents is observed upon the initiation of the reduction step. This is consistent with an expected decrease in electronic conductivity upon the incorporation of an insulating component.[19]

Increasing the charge cutoff potential to 4.7 V allows for higher initial discharge capacities at the expense of accelerated capacity fading (Figure 4.8). The discharge capacity of the unsubstituted (y=0) material increases by over 25% to 204 mAh/g but fades rapidly, losing over 30% in the first twenty cycles. The discharge capacities of compounds with y=0.05, 0.1, 0.15, and 0.2 improve modestly to 190, 174, 164, and 149 mAh/g, respectively. The rate of capacity fade of all aluminum containing materials is improved with respect to the parent material, but remains high, at nearly 1%/cycle.

Substitution of aluminum for cobalt in these materials has a pronounced effect on the rate capability, as can be seen in Figure 4.9. Upon discharging at increasing current

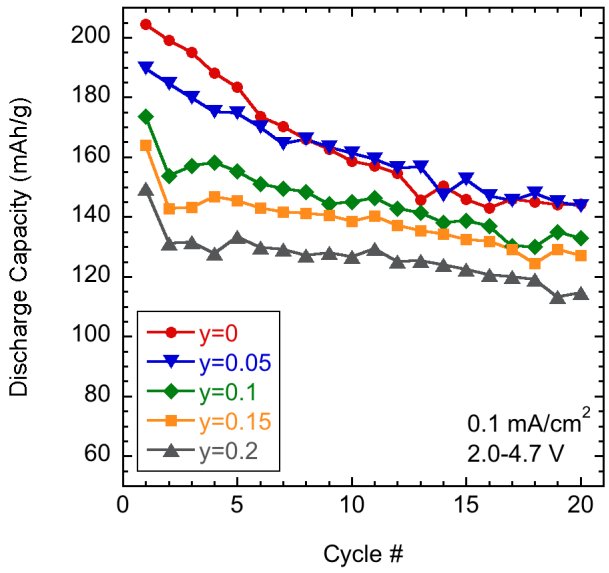

Figure 4.8: Discharge capacities of $Li/LiNi_{0.4}Co_{0.2-y}Al_yMn_{0.4}O_2$ ($0 \leq y \leq 0.2$) cells. Cycling was limited to 2.0-4.7 V vs. Li/Li^+ at a constant charge and discharge current density of 0.1 mA/cm^2.

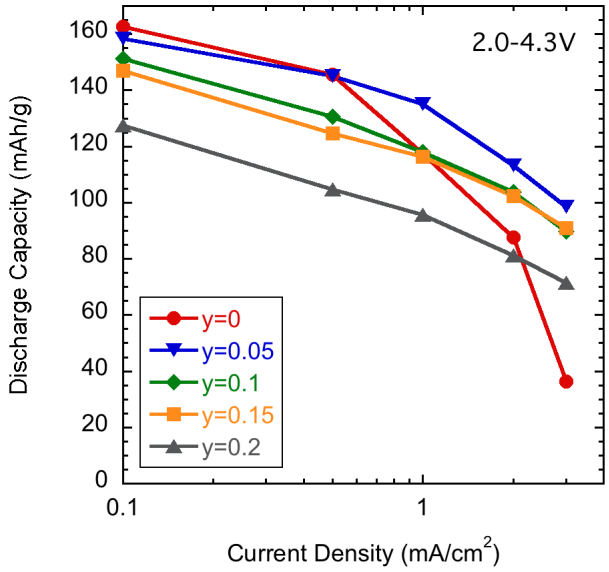

Figure 4.9: The rate performance of $Li/LiNi_{0.4}Co_{0.2-y}Al_yMn_{0.4}O_2$ ($0 \leq y \leq 0.2$) cells cycled between 2.0 and 4.3 V. Aluminum substituted materials show significantly improved capacity retention at high current densities compared to the parent compound. A constant charge current density of 0.1 mA/cm^2 was used for all materials.

densities the capacity of $LiNi_{0.4}Co_{0.2}Mn_{0.4}O_2$ electrodes diminishes rapidly to 36 mAh/g at 3 mA/cm^2. The incorporation of even small amounts of aluminum leads to electrodes with vastly improved rate performance, consistent with previous experiments in our lab on similarly produced $LiNi_{1/3}Co_{1/3-y}Al_yMn_{1/3}O_2$ powders.[18] In particular, the composition $LiNi_{0.4}Co_{0.15}Al_{0.05}Mn_{0.4}O_2$ performs quite well at high current densities, delivering 99 mAh/g when discharged at 3 mA/cm^2. While the neutron diffraction and XRD refinements reveal a slight increase in anti-site mixing concentration upon aluminum substitution, there is a consistent expansion of the lithium slab dimension with increasing y. This is significant, as the activation energy for lithium diffusion has been shown to be highly sensitive to the lithium slab dimension.[7, 13] Expansion of the lithium slab decreases the magnitude of the steric compression of the lithium ion residing in the activated state as well as the lithium-transition metal electrostatic interaction. The expansion of the lithium slab dimension upon aluminum substitution has a direct impact on electrochemical performance as seen in the decreased polarization at high current densities in Figure 4.10. This contradicts results obtained on $LiNi_{1/3}Co_{1/3-y}Al_yMn_{1/3}O_2$ compounds made by the mixed hydroxide method but not with those made by combustion synthesis.[16-18] The inconsistencies may arise from the details of aluminum distribution in the final product.[17, 55] The rapid nature of the combustion process allows for the mixing of chemical species on a very fine scale and the dispersion of species that would otherwise tend to partition using other synthetic methods. Active materials with elevated levels of metal clustering may exhibit variable electrochemical properties reflecting the changes in activity of the various compositions.

Preliminary cycle life studies for the y=0 and y=0.05 materials at low current densities (0.1 mA/cm^2, ~C/25) between 2.0 and 4.3 V reveal a significant degree of cycling stabilization in materials containing small aluminum contents (Figure 4.11). The $LiNi_{0.4}Co_{0.2}Mn_{0.4}O_2$ electrodes initially have discharge capacities exceeding 160 mAh/g but fade at a rate of 0.33%/cycle losing 25% after only 75 cycles. In contrast, $LiNi_{0.4}Co_{0.15}Al_{0.05}Mn_{0.4}O_2$ electrodes only lose 9.8% of their capacities over the first 75

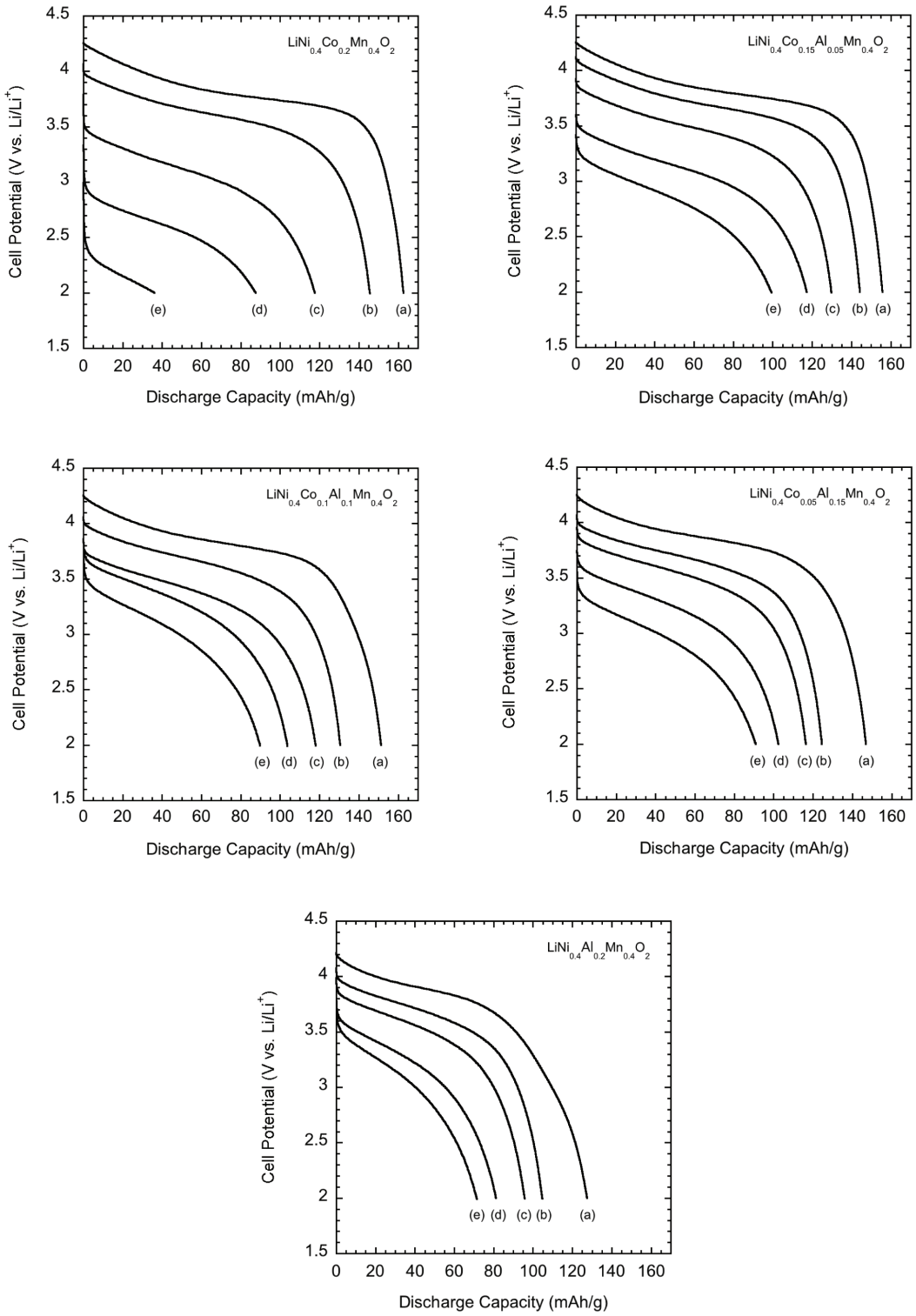

Figure 4.10: Discharge curves of $Li/LiNi_{0.4}Co_{0.2-y}Al_yMn_{0.4}O_2$ ($0 \leq y \leq 0.2$) cells at 0.1 (a), 0.5 (b), 1 (c), 2 (d), and 3 (e) mA/cm^2. A charge current of 0.1 mA/cm^2 was used for all samples and compositions are as marked.

cycles, corresponding to a fade rate of 0.13%/cycle. The discharge curves of a few cycles of $LiNi_{0.4}Co_{0.15}Al_{0.05}Mn_{0.4}O_2$ electrodes are presented in Figure 4.12 demonstrating the stable cycling behavior.

Another important factor to consider when exploring new materials for high-energy lithium ion batteries is the amount of first cycle irreversible capacity loss. Irreversible capacity loss, as defined in Equation 4.1, can have many potential sources and needs to

$$\textit{Irreversible Capacity} = (n^{th}\ \textit{Charge} - n^{th}\ \textit{Discharge})/n^{th}\ \textit{Charge} \times 100\% \qquad \text{Eq. 4.1}$$

be well characterized if such oxides are to be used in full cells with graphitic anodes. One mechanism proposed for the non-stoichiometric $Li_{1-z}Ni_{1+z}O_2$ materials is the local collapse of the lithium slab due to the oxidation of Ni^{2+} ions residing within the lithium plane during charge. The re-intercalation of the lithium vacancies in the vicinity of the nickel defect is thereby impeded by the slab contraction, except at very low rates.[56, 57] Slow lithium diffusion at high states of discharge has been observed in $LiNi_{1-y}Fe_yO_2$ materials

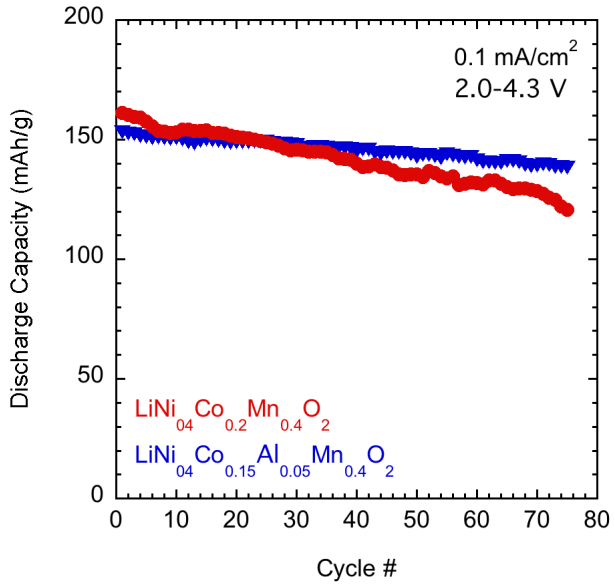

Figure 4.11: Discharge capacities as a function of cycle number for $LiNi_{0.4}Co_{0.2}Mn_{0.4}O_2$ and $LiNi_{0.4}Co_{0.15}Al_{0.05}Mn_{0.4}O_2$ materials. The rate of capacity fade is significantly reduced for aluminum containing materials (0.13%/cycle) compared to the parent oxide (0.33%/cycle).

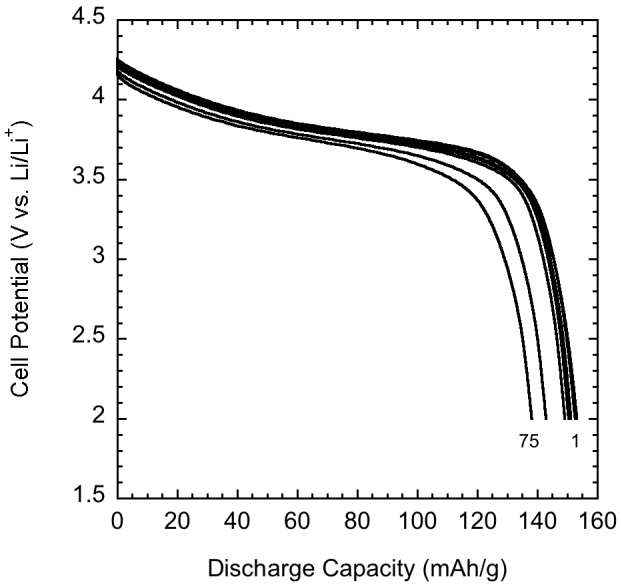

Figure 4.12: Discharge curves from the 1st, 2nd, 5th, 10th, 25th, 50th, and 75th cycles of $LiNi_{0.4}Co_{0.15}Al_{0.05}Mn_{0.4}O_2$ materials cycled between 2.0 and 4.3 V vs Li/Li^+.

leading to an increased concentration of lithium on the particle surface.[32] The decrease in the diffusion coefficient is a result of the reduction in concentration of di-vacancies in the lithium plane at high lithium contents. Di-vacancies mitigate the energetically most favorable diffusion pathway for lithium and the lack of a significant fraction of paired vacancies forces lithium motion through a more energetically unfavorable mono-vacancy pathway.[58, 59] The inability to transport lithium ions away from the particle surface at an appreciable rate can lead to the formation of a lithium excess surface material ($Li_{1+x}Ni_{1-y}Fe_yO_2$) at low potentials (~2V) in which lithium ions are located in tetrahedral coordination.[56, 60-62] X-ray absorption near-edge spectroscopy (XANES) experiments on $LiNi_{1/3}Co_{1/3}Mn_{1/3}O_2$ positive electrode materials have correlated the amount of irreversible capacity loss with the inability to fully reduce all of the Ni^{+4} produced during the initial charge cycle back to Ni^{2+} upon subsequent discharge.[50] The possibility of electrochemical side reactions with the electrolyte and the loss of electrochemical activity in a fraction of

the electrode domain during the initial charging process have also been explored.[63, 64]

The irreversible capacity loss for aluminum substituted materials cycled to 4.3 and 4.7 V are presented in Table 4.3. Unsubstituted $LiNi_{0.4}Co_{0.2}Mn_{0.4}O_2$ cycled in lithium half-cells to 4.3 V has a very low irreversible capacity loss of 6.1%, a level consistent with previous reports of materials synthesized using the glycine nitrate combustion method.[16, 65] This quantity increases with aluminum content up to the y=0.1 level, above which a loss of ~14% is observed regardless of aluminum content (y). Materials cycled to 4.7 V show a substantial increase in irreversible capacity losses although the effect of aluminum

Table 4.3: Irreversible capacity of $LiNi_{0.4}Co_{0.2-y}Al_yMn_{0.4}O_2$ ($0 \leq y \leq 0.2$) materials cycled to 4.3 and 4.7 V vs. Li/Li^+. A charge and discharge current density of 0.1 mA/cm^2 was used for all electrodes.

Composition	y	Irreversible Capacity Loss (4.3 V) (%)	Irreversible Capacity Loss (4.7 V) (%)
$LiNi_{0.4}Co_{0.2}Mn_{0.4}O_2$	0	6.10 ±0.47	14.32 ±0.2
$LiNi_{0.4}Co_{0.15}Al_{0.05}Mn_{0.4}O_2$	0.05	9.18 ±1.6	17.27 ±0.1
$LiNi_{0.4}Co_{0.1}Al_{0.1}Mn_{0.4}O_2$	0.1	13.24 ±2.2	14.83 ±1.0
$LiNi_{0.4}Co_{0.05}Al_{0.15}Mn_{0.4}O_2$	0.15	14.20 ±2.6	15.17 ±0.9
$LiNi_{0.4}Al_{0.2}Mn_{0.4}O_2$	0.2	14.14 ±4.1	20.86 ±5.2

substitution is less clear. Compounds with y=0, 0.05 and 0.2 show the largest differences, with increases of 135, 88 and 47%, respectively, over the same materials cycled to 4.3 V. Compositions with intermediate aluminum contents fare much better with irreversible losses increasing only 12% for y=0.1 and 7% for y=0.15.

The first charge and discharge cycles for cells cycled to 4.3 and 4.7 V are shown in Figure 4.13. All materials show a monotonic increase in cell potential on both charge and discharge, consistent with a single-phase intercalation reaction. There is an apparent increase in polarization at the end of charge in cells containing aluminum-substituted compounds, as indicated by the magnitude of the voltage relaxation. This is seen regardless of the oxidation cutoff potential but is much more pronounced in cells cycled to 4.7 V. There is also a distinct increase in potential at ~4.5 V during the initial charging process for

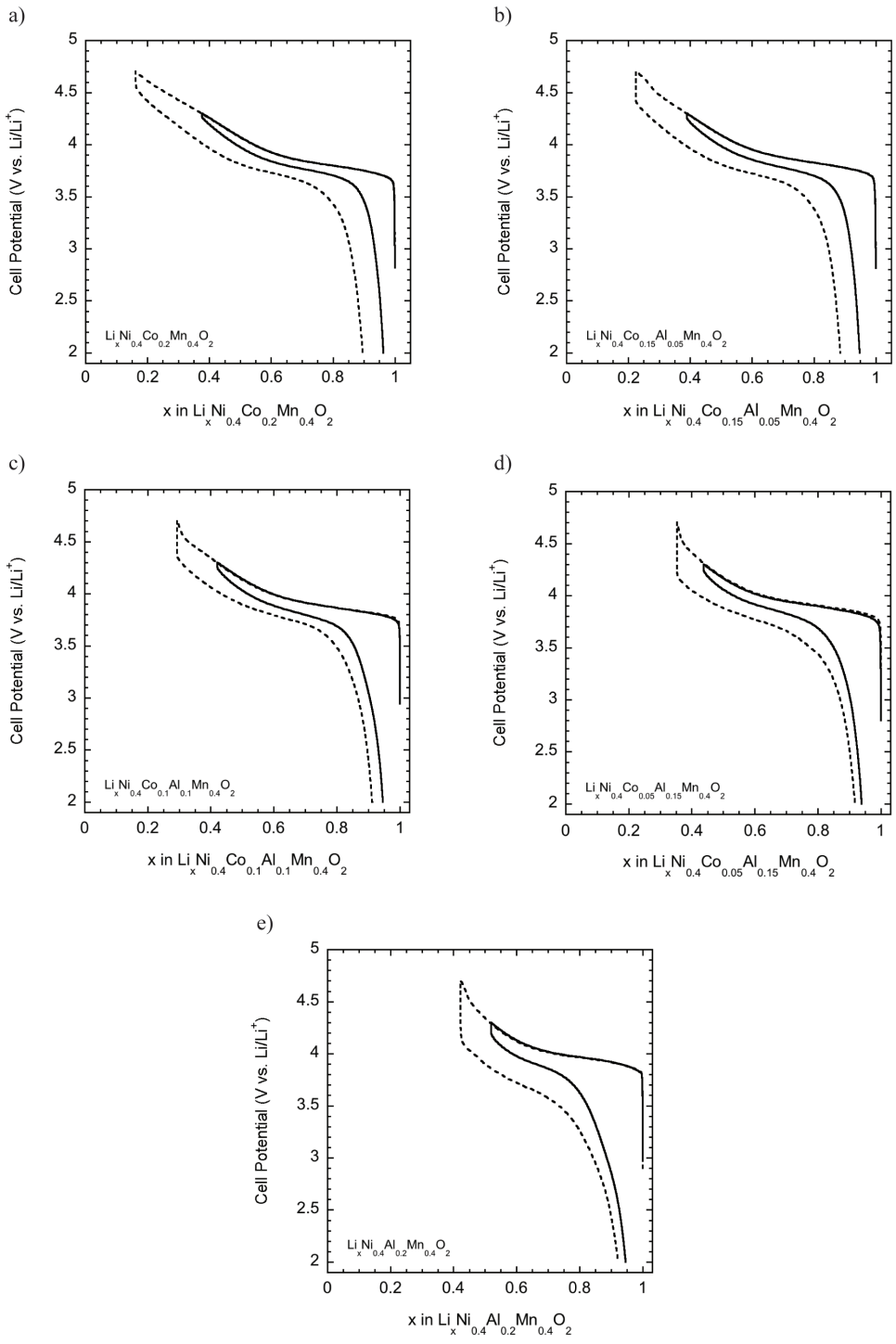

Figure 4.13: First cycle charge and discharge curves of $Li/LiNi_{0.4}Co_{0.2-y}Al_yMn_{0.4}O_2$ with (a) y=0, (b) y=0.05, (c) y=0.1, (d) y=0.15, and (e) y=0.2. All cells were cycled between 2.0 and 4.3 or 4.7 V at a current density of 0.1 mA/cm^2. The increase in polarization at the end of charge is clearly visible and increases with aluminum content.

all cells containing aluminum substituted compounds. The exact source of this behavior is presently not understood, but may be related to a decrease in conductivity resulting from the addition of an insulating component to the solid solution or related lithium transport limitations.

To understand better the effects of aluminum substitution on the transport properties of $LiNi_{0.4}Co_{0.2-y}Al_yMn_{0.4}O_2$ materials, the pressed pellet electronic conductivities were measured using AC impedance spectroscopy. The Arrhenius plot as a function of aluminum content (y) is shown in Figure 4.14. The composition $LiNi_{0.4}Co_{0.2}Mn_{0.4}O_2$ has the highest electronic conductivity ($1.1x10^{-5}$ S/cm) of all the samples at 75° C. It is, however, several orders of magnitude lower than that of other layered oxides such as $LiCoO_2$, which have values on the order of 10^{-3} S/cm at room temperature.[66] The electronic conductivities of these highly substituted layered oxide materials are highly sensitive to even small levels of aluminum substitution; for example, for $LiNi_{0.4}Co_{0.15}Al_{0.05}Mn_{0.4}O_2$, it is only $1.2x10^{-6}$ S/cm at 75°C. It is lowered further to $2.2x10^{-8}$ S/cm at y=0.1, $8.6x10^{-9}$ S/cm at y=0.15, and $3.6x10^{-9}$ S/cm at y=0.2. This is consistent with the substitution of an *sp*-type metal for

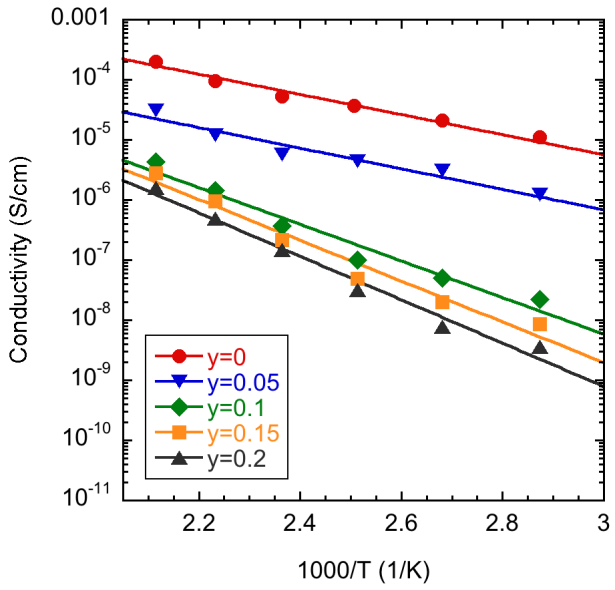

Figure 4.14: Pressed pellet electronic conductivities of $LiNi_{0.4}Co_{0.2-y}Al_yMn_{0.4}O_2$ ($0 \leq y \leq 0.2$) materials as a function of inverse temperature.

cobalt in these systems, which causes a decrease in electronic conductivity.[17] Aluminum has no available *d*-states near the Fermi energy and therefore, can not participate in electron transport processes during cycling.

The activation energies calculated from the Arrhenius type behavior seen in Figure 4.14 are presented in Table 4.3. The magnitude of these values is consistent with an activated, small polaron conduction mechanism and tracks in a very similar manner to the overall conductivity results discussed above.[10, 67-70] The activation energy increases with aluminum content (y) and agrees with the shift in bond covalency upon aluminum

Table 4.3: Activation energies for electron transport as a function of aluminum content (y).

Formula	y	E_a (eV)
$LiNi_{0.4}Co_{0.2}Mn_{0.4}O_2$	0	0.346(1)
$LiNi_{0.4}Co_{0.15}Al_{0.05}Mn_{0.4}O_2$	0.05	0.361(2)
$LiNi_{0.4}Co_{0.1}Al_{0.1}Mn_{0.4}O_2$	0.1	0.639(1)
$LiNi_{0.4}Co_{0.05}Al_{0.15}Mn_{0.4}O_2$	0.15	0.707(1)
$LiNi_{0.4}Al_{0.2}Mn_{0.4}O_2$	0.2	0.752(4)

substitution observed in the FTIR experiments. The increase in average bond strength in the transition metal plane impedes the vibrationally coupled motion of the charged polaron and, therefore, lowers the electronic conductivity.

The effect of aluminum substitution on lithium diffusion rates was studied using the galvanostatic intermittent titration technique (GITT) on porous electrodes in lithium half-cells. Chemical diffusion coefficients of lithium (D_{Li}) as a function of state of charge were extracted from the voltage responses to the incremental passage of current.[71-73] The cell potential during the titration step was found to be linear with respect to the square root of time, and the chemical diffusion coefficient of lithium was calculated using Equation 4.2.[73, 74] In this content τ is the time of the current pulse, m_B the active material

mass, V_m the molar volume, M_B the molecular weight, A_s the surface area in contact with the electrolyte, ΔE_s is the change in stationary cell potential, and ΔE_τ is the change in

$$D_{Li} = \frac{4}{\pi \tau}\left(\frac{m_B V_m}{M_B A_s}\right)^2\left(\frac{\Delta E_s}{\Delta E_\tau}\right)^2 \qquad \tau << \frac{L^2}{D_{Li}} \qquad \text{Eq. 4.1}$$

cell potential during the titration step corrected for IR losses. The absolute value of the diffusion coefficient calculated in this manner is highly sensitive to the amount of active surface area (A) in contact with the electrolyte and therefore capable of reacting. These values are unknown so the geometric surface area of the electrode (1.8 cm^2) was used. Because all of the electrodes were prepared the same way from powders with nearly identical particle size distributions and morphologies, direct comparisons (especially the behavior as a function of state-of-charge) are possible. Another consideration, however, is that the boundary conditions required for GITT analysis may not have been met. Porous electrodes with a thickness of ~60 μm were used in these experiments. GITT analysis assumes that the current density is equally distributed through the entire electrode so that the flux of lithium ions across a particle surface is equivalent throughout the electrode. According to porous electrode theory, however, as the matrix and electrolyte solution have different conductivities the current will necessarily partition itself between the two phases to minimizes the ohmic losses in the system.[75] This implies that, except in the case of exceptionally slow surface kinetics, a porous electrode may never truly satisfy the boundary conditions for GITT analysis. A more accurate determination of D_{Li} may be possible using thin film electrodes of the active material (see Chapter 8 for further discussion), however, such electrodes can suffer from highly anisotropic transport properties, and depending on how they are made, the diffusion length may still be ill defined.

The results of the GITT analysis during the first charge cycle are presented in Figure 4.15. For comparison purposes, the data is presented as a dimensionless ratio

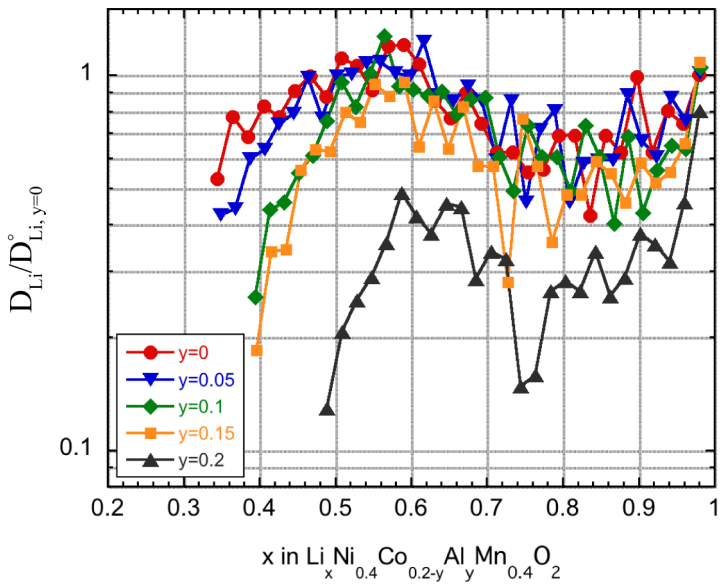

Figure 4.15: Normalized chemical diffusion coefficient of lithium ($D_{Li}/D^{\circ}_{Li,\,y=0}$) as a function of lithium content for the series of materials, $Li/LiNi_{0.4}Co_{0.2-y}Al_yMn_{0.4}O_2$ ($0 \le y \le 0.2$). The diffusion coefficient was calculated using Eq. 4.2 during the first charge process.

with respect to the initial diffusion coefficient measured for $Li_xNi_{0.4}Co_{0.2}Mn_{0.4}O_2$ at x=1 ($D_{Li}/D^{\circ}_{Li,\,y=0}$). At the beginning of the charging process, D_{Li} is nearly the same for all materials independent of y, even though the electrical conductivity was observed to vary by nearly four orders of magnitude. During the initial charge process, the chemical diffusion coefficient decreases, reaching a minimum near x=0.8. This behavior may reflect a weak charge ordering effect in the lithium plane at intermediate states of charge.[76-78] The diffusion coefficient increases upon removal of lithium past this point, most likely due to an expansion of the lithium slab dimension and an increase in di-vacancy concentration. D_{Li} decreases dramatically at low lithium contents, consistent with the increase in cell polarization at the end of charge. The effect of aluminum substitution is relatively minor during the initial charging process for materials with $y \le 0.1$. At higher states of charge all of the aluminum containing materials show reduced values of D_{Li} proportional to y. The fully substituted material, $LiNi_{0.4}Al_{0.2}Mn_{0.4}O_2$, exhibits the lowest D_{Li} of all the materials tested over all lithium contents, dropping nearly an order of magnitude at the end of charge

(x=0.49).

It is important to note that during normal galvanostatic experiments, compositions corresponding to the high states-of-charge are usually not achieved. Thus, while aluminum substitution does not appear to increase diffusion coefficients significantly, it limits the composition changes to a range with the highest average rates of lithium diffusion, resulting in improved performance at high current densities. This alone many not explain the observed rate behavior and other factors that need to be addressed to understand the behavior of these materials. These factors include evaluating any underlying changes in active surface area, quantifying the surface reactivity for lithium ion uptake, and probing the influence of cycle history on rate performance in substituted materials (see Chapter 8 for further discussion). Interestingly, the decrease in lithium mobility at the end of charge may act as a form of fundamental overcharge protection, improving the cycling and thermal stability of the material.

4.4.2 $LiNi_{0.4}Co_{0.15}Fe_{0.05}Mn_{0.4}O_2$

A series of iron substituted materials was also synthesized using the glycine nitrate combustion method. As discussed previously, lithium iron oxide materials tend to have structures with three-dimensional character and hence suffer from poor electrochemical performance because they lack diffusional pathways for lithium. The competing effects of increased anti-site defects and cobalt content can be probed by comparing iron substituted materials with the $LiNi_{0.4}Co_{0.2-y}Al_yMn_{0.4}O_2$ system previously described.

Due to the formation of secondary impurity phases in materials sintered at 800° C in air, substitution was limited to the y=0.05 level (Figure 4.16). Subsequent results suggest that the synthesis of a single-phase material with y=0.1 may be possible under the proper conditions but will not be discussed further presently. Elemental analysis (Table 4.5) reveals a stoichiometry very close to the nominally assumed composition. Unlike aluminum, iron is electrochemically active in the same potential window as the

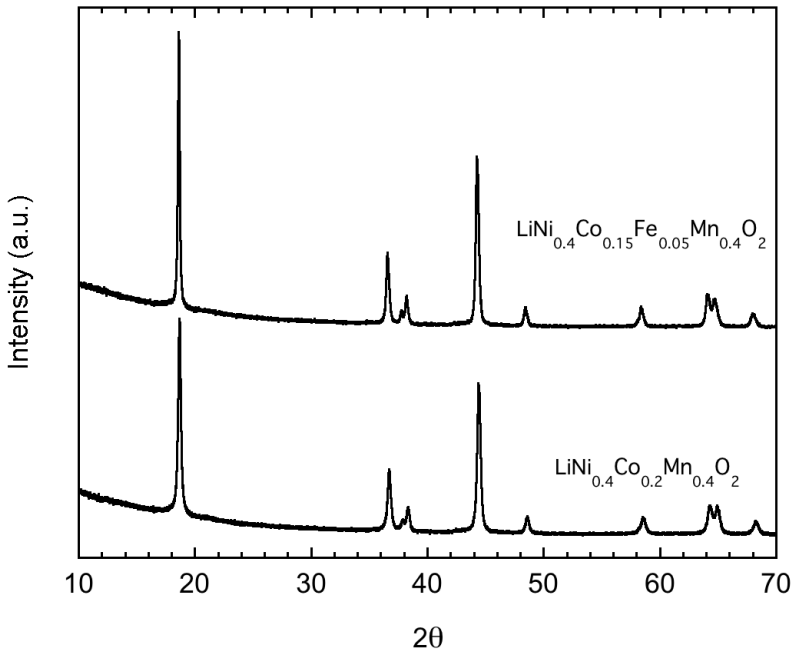

Figure 4.16: Powder XRD patterns of $LiNi_{0.4}Co_{0.15}Fe_{0.05}Mn_{0.4}O_2$ and $LiNi_{0.4}Co_{0.2}Mn_{0.4}O_2$. No impurity phases can be detected and all peaks can be indexed in the $R\bar{3}m$ space group.

Table 4.5: Nominal and experimental elemental compositions of iron substituted oxides.

Nominal Composition	Experimentally Observed Composition
$LiNi_{0.4}Co_{0.15}Fe_{0.05}Mn_{0.4}O_2$	$Li_{1.01}Ni_{0.39}Co_{0.15}Fe_{0.05}Mn_{0.41}O_{2-\delta}$

Ni^{2+}/ Ni^{4+} redox couple and the substitution of iron for cobalt has a negligible impact on the theoretical capacity for the composition $LiNi_{0.4}Co_{0.15}Fe_{0.05}Mn_{0.4}O_2$ (279 mAh/g).[29, 33]

The results of the Rietveld analysis on the combined X-ray and neutron diffraction data sets are presented in Table 4.6. Both the *a* and *c* unit cell parameters increase slightly (0.2%) upon iron substitution. The expansion of the M-M separation can be explained by the larger ionic radius of high spin Fe^{3+} in six-fold coordination (0.645 Å) relative to Co^{3+} (0.545 Å).[12] The opening of the unit cell in the *c* direction is primarily a result of an increase in the transition metal layer dimension, as the lithium slab dimension is unchanged. The anti-site defect concentration is slightly increased relative to $LiNi_{0.4}Co_{0.2}Mn_{0.4}O_2$ and is

Table 4.6: Crystal structure parameters from combined X-ray, neutron diffraction Rietveld refinement.

Fe Content	Unit Cell Parameters		z_{Ox}	Unit Cell Volume (Å^3)	Ni_{3a}	I (LiO_2) (Å)	R_{wp} (%)
	a (Å)	c (Å)					
0	2.87238(2)	14.2688(2)	0.24165(3)	101.954(2)	0.066(1)	2.616(1)	4.26
0.05	2.88027(4)	14.2930(4)	0.24180(1)	102.689(2)	0.072(1)	2.617(1)	4.53

equivalent to the levels observed in aluminum substituted compounds. Given the tendency of lithium iron oxides to crystallize with lithium and iron intermixed between the lithium and transition metal plane, this result is somewhat surprising.[30, 32, 79] However, the inability to synthesize single phase materials suggests that the stability of the layered structure is highly limited except at low iron contents.

The FTIR signature of $LiNi_{0.4}Co_{0.15}Fe_{0.05}Mn_{0.4}O_2$ is unchanged from unsubstituted $LiNi_{0.4}Co_{0.2}Mn_{0.4}O_2$ materials (Figure 4.17). The adsorption peaks associated with asymmetric MO_6 vibration and O-M-O are clearly visible at 594 and 531 cm^{-1} while

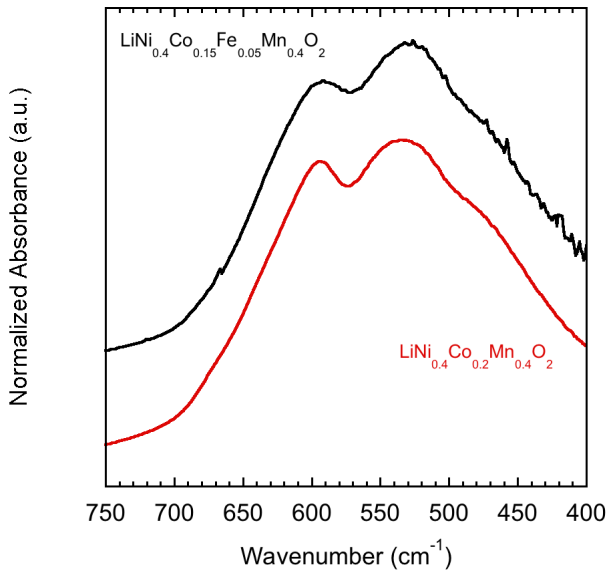

Figure 4.17: FTIR spectra of $LiNi_{0.4}Co_{0.15}Fe_{0.05}Mn_{0.4}O_2$ and $LiNi_{0.4}Co_{0.2}Mn_{0.4}O_2$ materials. The three adsorption bands of the MO_6 structural unit can be seen in both spectra and there is only minor shifting upon the substitution of iron.

the bending mode at 465 cm^{-1} is observed as a small inflection on the main adsorption band. The peaks are observed to broaden slightly in the substituted materials consistent with the intermixing of an additional species in the transition metal plane. The average bond covalency in the transition metal plane is unchanged due to the similar bonding nature of iron, cobalt, nickel, and manganese and the low levels of substitution in these materials.[80]

$LiNi_{0.4}Co_{0.15}Fe_{0.05}Mn_{0.4}O_2$ exhibits a reduced capacity compared to $LiNi_{0.4}Co_{0.2}Mn_{0.4}O_2$ when cycled in lithium coin cells between 2.0 and 4.3 V at 0.1 mA/ cm^2 (Figure 4.18). The initial discharge capacity of 146 mAh/g is comparable to that of $LiNi_{0.4}Co_{0.05}Al_{0.15}Mn_{0.4}O_2$ electrodes, which lose only 2% of the initial discharge capacity after the first twenty cycles. In contrast, $LiNi_{0.4}Co_{0.15}Fe_{0.05}Mn_{0.4}O_2$ electrodes fade rapidly, losing 8.8% of the initial discharge capacity under the same cycling conditions. The magnitude of the capacity fade exceeds that of the parent material (5.8%) and is similar to the electrochemical behavior observed in other iron substituted layered oxide electrode materials.[29]

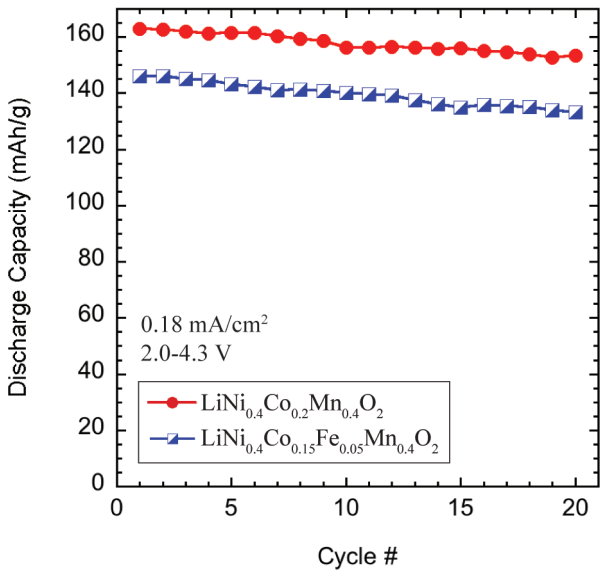

Figure 4.18: Discharge capacities of Li/$LiNi_{0.4}Co_{0.2}Mn_{0.4}O_2$ and Li/$LiNi_{0.4}Co_{0.15}Fe_{0.05}Mn_{0.4}O_2$ cells. Cycling

was limited to 2.0-4.3 V vs. Li/Li^+ at a constant charge and discharge current density of 0.1 mA/cm^2.

The differential capacity plots reveal that the peak oxidation and reduction potentials shift to higher potentials in cells containing $LiNi_{0.4}Co_{0.15}Fe_{0.05}Mn_{0.4}O_2$. (Figure 4.19). The oxidation peak shape also changes significantly upon substitution, becoming more asymmetric with an abrupt increase in oxidation occurring at 3.74 V vs. Li/Li^+. The magnitude of the increase in cell potential is very similar to $LiNi_{0.4}Co_{0.15}Al_{0.05}Mn_{0.4}O_2$

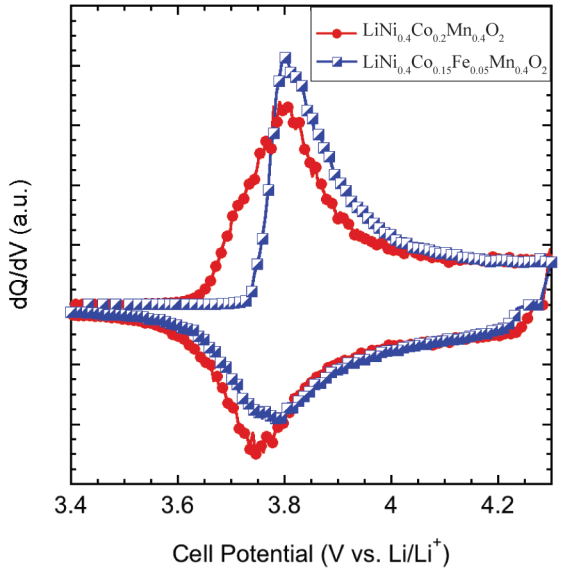

Figure 4.19: Differential capacity plots of the first cycles of $Li/LiNi_{0.4}Co_{0.2}Mn_{0.4}O_2$ and $Li/LiNi_{0.4}Co_{0.15}Fe_{0.05}Mn_{0.4}O_2$ cells. Current density was 0.1 mA/cm^2 in the potential range 2.0-4.3 V vs. Li/Li^+.

materials, although the presence of redox active iron *d*-orbitals near the Fermi energy suggests that this is a result of either steric or electronic changes in the structure. The increase in redox potential upon iron substitution has been observed in $LiNi_{1-z}Fe_zO_2$ materials and has been correlated with the difference in ionic radius between Fe^{3+} (0.645 Å in the high spin state) and Ni^{+2} (0.56 Å in the low spin state).[12, 33] The intermixing of iron and nickel in the transition metal planes of these compounds leads to compressed FeO_6 and elongated NiO_6 octahedra, making the oxidation to Ni^{+4} more difficult due to an increasing strain upon reaction. While the materials presented in this work are significantly more

complicated, an increase in cell potential upon iron substitution has been predicted using first principle methods for the related $Li_xNi_{1/3}Co_{1/3}Fe_{1/6}Mn_{1/3}O_2$ phase for $0<x<1/2$.[29]

The discharge capacity of $LiNi_{0.4}Co_{0.15}Fe_{0.05}Mn_{0.4}O_2$ increases upon charging to 4.7 V vs. Li/Li^+ to 174 mAh/g (Figure 4.20). It is interesting to observe that $LiNi_{0.4}Co_{0.15}Al_{0.05}Mn_{0.4}O_2$ cells cycled to 4.3 and 4.7 V have higher discharge capacities than the iron analogs, despite having nearly equivalent peak oxidation and reduction potentials.

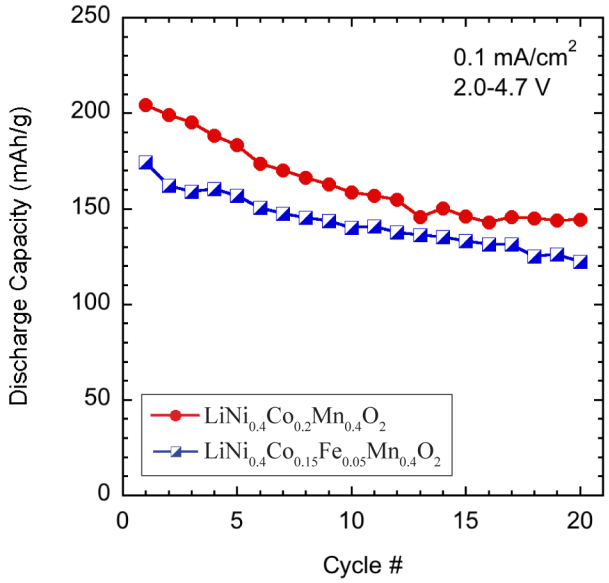

Figure 4.20: Discharge capacities of $Li/LiNi_{0.4}Co_{0.2}Mn_{0.4}O_2$ and $Li/LiNi_{0.4}Co_{0.15}Fe_{0.05}Mn_{0.4}O_2$ cells. Cycling was limited to 2.0-4.7 V vs. Li/Li^+ at a constant charge and discharge current density of 0.1 mA/cm^2.

As iron is expected to be electrochemically active in the same potential range as the $Ni^{2+/4+}$ redox couple, the decreased capacity may be a result of the increased polarization at the end of charge (Figure 4.21). The capacity fades more rapidly upon cycling to 4.7 V, with a loss of 30% observed over the initial twenty cycles.

The rate capability of the parent and iron substituted compound is shown in Figure 4.22. Cycling at increasing current densities leads to a substantial decrease in delivered capacity as has been observed with $LiNi_{1/3}Co_{1/4}Fe_{1/12}Mn_{1/3}O_2$ electrodes.[16] Unlike the

aluminum substituted materials, the capacity is not stabilized at increasing current densities, delivering only 50 mAh/g at a current density of 3 mA/cm^2. The similar electrochemical behavior of the parent and iron substituted compound is consistent with the structural data, specifically the nearly identical lithium slab dimensions.

Cells cycled at 0.1 mA/cm^2 between 2.0 and 4.3 V showed a nearly three-fold increase in irreversible capacity losses (16.7(9)%) relative to those containing $LiNi_{0.4}Co_{0.2}Mn_{0.4}O_2$ (6.1(5)%). The irreversible capacity losses of cells with $LiNi_{0.4}Co_{0.15}Fe_{0.05}Mn_{0.4}O_2$ electrodes are found to be relatively insensitive to the charge cutoff potential. Those cycled to 4.7 V lost an average of 19.6(9)% on the first cycle. The behavior differs from that of cells containing $LiNi_{0.4}Co_{0.2}Mn_{0.4}O_2$ and $LiNi_{0.4}Co_{0.15}Al_{0.05}Mn_{0.4}O_2$ electrodes, where the first cycle losses increased substantially upon cycling to 4.7 V. This suggests that the source of the irreversible capacity losses may be different for iron-containing materials compared to those containing cobalt and/or aluminum. While changes in the surface reactivity for parasitic electrolyte reactions cannot be excluded, the most likely source is a decrease in the lithium ion mobility. A drop in lithium transport at the end of discharge has been observed in other iron substituted materials, although the formation of a lithium excess Li_2MO_2 (where M represents transition metals with an average valence state of 2+) phase was not observed in cells cycled to 2.0 V in the present work.[32]

The pressed pellet conductivity of $LiNi_{0.4}Co_{0.15}Fe_{0.05}Mn_{0.4}O_2$ is compared to that of $LiNi_{0.4}Co_{0.2}Mn_{0.4}O_2$ in Figure 4.23. As can be clearly seen, the incorporation of iron into the lattice lowers the electronic conductivity, dropping it from $1.1x10^{-5}$ S/cm at 75° C for $LiNi_{0.4}Co_{0.2}Mn_{0.4}O_2$ to $2.7x10^{-8}$ S/cm for $LiNi_{0.4}Co_{0.15}Fe_{0.05}Mn_{0.4}O_2$. The activation energy increases to 660(2) meV, indicating increased difficulty in moving the charge-carrying defect in the substituted material. This result is intriguing, as iron has *d*-states available near the Fermi energy and iron substituted materials have been calculated to have smaller band gaps than unsubstituted materials. This would indicate that the thermally driven formation of charged defects, either electrons or holes, should be more favorable in the

substituted system.[29] As indicated in the FTIR experiments, the incorporation of iron does

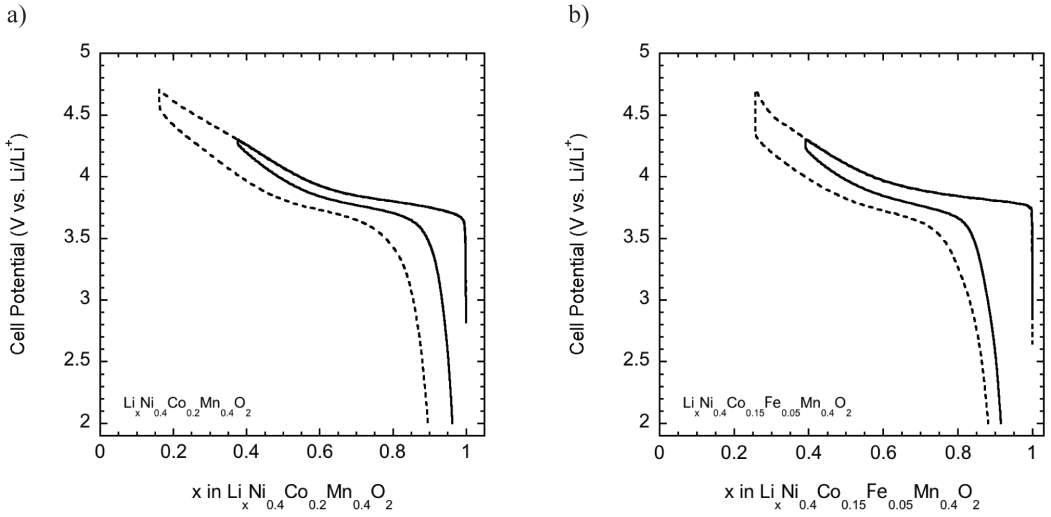

Figure 4.21: First cycle charge and discharge curves of (a) Li/$LiNi_{0.4}Co_{0.2}Mn_{0.4}O_2$ and (b) Li/$LiNi_{0.4}Co_{0.15}Fe_{0.05}Mn_{0.4}O_2$ cells. All cells were cycled between 2.0 and 4.3 or 4.7 V at a current density of 0.1 mA/cm^2. An abrupt increase in polarization is observed in iron substituted materials at the end of charge.

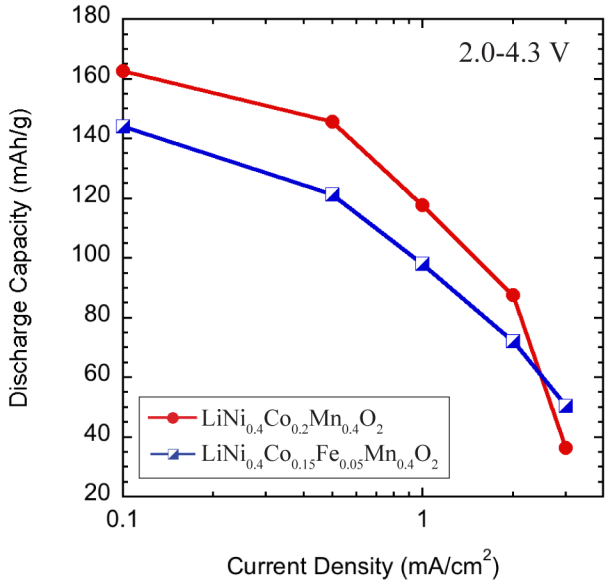

Figure 4.22: The rate performance of Li/$LiNi_{0.4}Co_{0.2}Mn_{0.4}O_2$ and Li/$LiNi_{0.4}Co_{0.15}Fe_{0.05}Mn_{0.4}O_2$ half cells cells cycled between 2.0 and 4.3 V. Both unsubstituted and iron containing materials exhibit limited rate performance.. A constant charge current density of 0.1 mA/cm^2 was used for all materials.

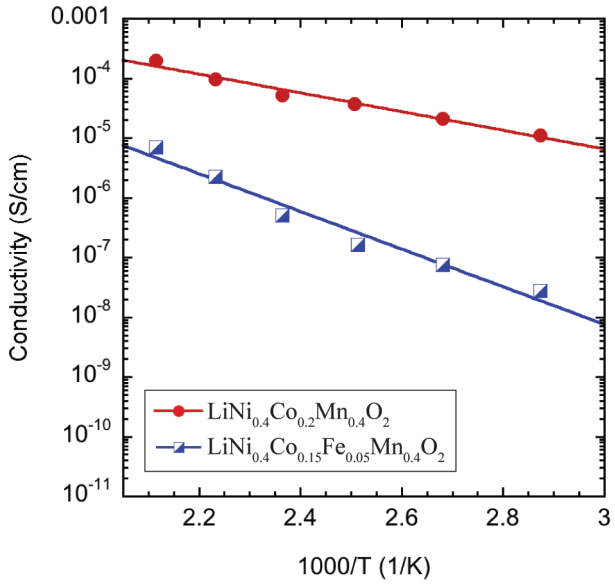

Figure 4.23: Pressed pellet electronic conductivities of $LiNi_{0.4}Co_{0.2}Mn_{0.4}O_2$ and $LiNi_{0.4}Co_{0.15}Fe_{0.05}Mn_{0.4}O_2$ materials as a function of inverse temperature.

not lead to a shift in the bonding nature relative to that of the parent material, so the source of the increased activation energy and decreased conductivity must derive from the structure itself. These results also reinforce the important role of cobalt in layered oxide materials. Owing to the fact that both *sp*- and transition metal substitution decrease the electronic conductivity, the observed trends may relate more to a disruption in the cobalt bonding network than the presence of the substituting atom.

4.5 Conclusions

A series of new layered oxide positive electrode materials based on the $LiNi_{0.4}Co_{0.2-y}M_yMn_{0.4}O_2$ (M=Al, Fe) system has been synthesized using the glycine nitrate combustion method. Aluminum is found to be soluble over the entire composition range ($0 \leq y \leq 0.2$) with no second phase impurities observed using XRD. Simultaneous Rietveld refinement of both X-ray and neutron diffraction spectra indicate that the anti-site defect concentration is slightly elevated upon substitution. However, the lithium slab dimension is observed

to increase in aluminum containing compounds as a result of an increase in the covalent bonding character of the transition metal layer. This results in a dramatically improved rate performance with the composition $LiNi_{0.4}Co_{0.15}Al_{0.05}Mn_{0.4}O_2$ delivering over twice the capacity of unsubstituted materials when cycled at 3 mA/cm^2. The increase in covalent bonding is associated with a decrease in electronic conductivity and increased activation energy. The chemical diffusion coefficient of lithium is largely unaffected at low substitution levels ($0 \leq y \leq 0.1$) except at high states of charge where lithium transport decreases rapidly. Finally, the cycling stability is observed to improve substantially in aluminum substituted oxides over a wide range of current densities.

The formation of single-phase iron containing compounds was limited to low substitution levels, specifically $LiNi_{0.4}Co_{0.15}Fe_{0.05}Mn_{0.4}O_2$. Iron containing oxides show a slightly elevated anti-site defect concentration and no change in the lithium slab dimension. Cells cycled to 4.3 V showed a reduced capacity and limited rate capability. The electronic conductivity decreased several orders of magnitude relative to the parent oxide although the ionic nature of the bonding network was largely unchanged. These factors, combined with the high fade rate of iron containing materials imply that iron should be avoided in attempting to design high energy and power density layered oxide materials.

4.6 Acknowledgments

This work was supported by the Assistant Secretary for Energy Efficiency and Renewable Energy, Office of Vehicle Technologies of the U.S. Department of Energy under Contract No. DE-AC02-05CH11231. This work has benefited from the use of the Lujan Center at the Los Alamos Neutron Science Center, funded by the DOE Office of Basic Energy Sciences and Los Alamos National Laboratory funded by the Department of Energy under contract W-7405-ENG-36. The authors would also like to thank Aaron Kueck for his expertise in the obtaining the TEM images of the active materials.

4.7 References

1. Nagaura, T., *Development of rechargeable lithium batteries, II. Lithium ion rechargeable batteries.* Progress in Batteries & Battery Materials, 1991. **10**: p. 218-226.

2. Whittingham, M.S., *Lithium batteries and cathode materials.* Chemical Reviews, 2004. **104**(10): p. 4271-4301.

3. Yabuuchi, N., et al., *Solid-State Chemistry and Electrochemistry of LiCo(1/3)Ni(1/3) Mn(1/3)O(2) for Advanced Lithium-Ion Batteries.* Journal of the Electrochemical Society, 2005. **152**(7): p. A1434-A1440.

4. Ohzuku, T. and Y. Makimura, *Layered lithium insertion material of LiCo(1/3)Ni(1/3) Mn(1/3)O(2) for lithium-ion batteries.* Chemistry Letters, 2001(7): p. 642-643.

5. Ma, M., et al., *Structural and electrochemical behavior of LiMn(0.4)Ni(0.4)Co(0.2) O(2).* Journal of Power Sources, 2007. **165**(2): p. 517-534.

6. Yang, S., et al., *Performance of LiFePO(4) as lithium battery cathode and comparison with manganese and vanadium oxides.* Journal of Power Sources, 2003. **119-121**: p. 239-246.

7. Kang, K. and G. Ceder, *Factors that affect Li mobility in layered lithium transition metal oxides.* Physical Review B (Condensed Matter and Materials Physics), 2006. **74**(9): p. 094105-7.

8. Rougier, A., P. Gravereau, and C. Delmas, *Optimization of the Composition of the Li(1-z)Ni(1+z)O(2) Electrode Materials: Structural, Magnetic, and Electrochemical Studies.* Journal of The Electrochemical Society, 1996. **143**(4): p. 1168-1175.

9. Rougier, A., et al., *Effect of cobalt substitution on cationic distribution in LiNi(1 - y) Co(y)O(2) electrode materials.* Solid State Ionics, 1996. **90**(1-4): p. 83-90.

10. Saadoune, I. and C. Delmas, *LiNi(1-y)Co(y)O2 positive electrode materials: Relationships between the structure, physical properties and electrochemical behaviour.* Journal of Materials Chemistry, 1996. **6**(2): p. 193-199.

11. Ngala, J.K., et al., *The synthesis, characterization and electrochemical behavior of the layered LiNi(0.4)Mn(0.4)Co(0.2)O(2) compound.* Journal of Materials Chemistry, 2004. **14**(2): p. 214-220.

12. Shannon, R., *Revised effective ionic radii and systematic studies of interatomic distances in halides and chalcogenides.* Acta Crystallographica Section A, 1976. **32**(5): p. 751-767.

13. Kang, K.S., et al., *Electrodes with high power and high capacity for rechargeable lithium batteries.* Science, 2006. **311**(5763): p. 977-980.

14. Breger, J., et al., *NMR, PDF and RMC study of the positive electrode material LiNi(0.5)Mn(0.5)O(2) synthesized by ion-exchange methods.* Journal of Materials Chemistry, 2007. **17**(30): p. 3167-3174.

15. Wu, E.J., P.D. Tepesch, and G. Ceder, *Size and charge effects on the structural stability of LiMO2 (M = transition metal) compounds.* Philosophical Magazine B-Physics of Condensed Matter Statistical Mechanics Electronic Optical and Magnetic Properties, 1998. **77**(4): p. 1039-1047.

16. Wilcox, J., S. Patoux, and M. Doeff, *Structure and Electrochemistry of LiNi(1/3) Co(1/3-y)M(y)Mn(1/3)O(2) (M=Ti, Al, Fe) Cathode Materials.* Journal of the Electrochemical Society. **Submitted, August 2008**.

17. Hu, S.-K., et al., *Effect of Co content on performance of LiAl(1/3-x)Co(x)Ni(1/3) Mn(1/3)O(2) compounds for lithium-ion batteries.* Journal of Power Sources, 2006. **160**(2): p. 1287-1293.

18. Wilcox, J. and M. Doeff, *Characterization and Electrochemical Performance of Substituted LiNi(0.4)Co(0.2-y)Al(y)Mn(0.4)O(2) (0<y<0.2) Cathode Materials.* ECS Transactions, 2008. **11**(29): p. 27-33.

19. Ceder, G., et al., *Identification of cathode materials for lithium batteries guided by first-principles calculations.* Nature, 1998. **392**(6677): p. 694-696.

20. Albrecht, S., et al., *Electrochemical and thermal behavior of aluminum- and magnesium-doped spherical lithium nickel cobalt mixed oxides Li(1-x)Ni(1-y-z) Co(y)M(z)O(2) (M = Al, Mg).* Journal of Power Sources, 2003. **119**: p. 178-183.

21. Zhou, F., et al., *The effect of Al substitution on the reactivity of delithiated LiNi(1/3) Mn(1/3)Co(1/3-z)Al(z)O(2) with non-aqueous electrolyte.* Electrochemistry Communications, 2008. **10**(8): p. 1168-1171.

22. Zhou, F., et al., *The Effect of Al Substitution on the Reactivity of Delithiated LiNi(0.5-z)Mn(0.5-z)Al(2z)O(2) with Nonaqueous Electrolyte.* 2008. **11**(9): p. A155-157.

23. Hewston, T.A. and B.L. Chamberland, *A Survey of first-row ternary oxides LiMO(2) (M = Sc-Cu).* Journal of Physics and Chemistry of Solids, 1987. **48**(2): p. 97-108.

24. Wang, M. and A. Navrotsky, *LiMO(2) (M=Mn, Fe, and Co): Energetics, polymorphism and phase transformation.* Journal of Solid State Chemistry, 2005. **178**(4): p. 1230-1240.

25. Cox, D.E., et al., *Neutron diffraction and Mossbauer study of ordered and disordered LiFeO(2).* Physical Review, 1963. **132**(4): p. 1547-&.

26. Anderson, J.C. and M. Schieber, *Order-disorder transitions in heat-treated rock-salt lithium ferrite* Journal of Physics and Chemistry of Solids, 1964. **25**(9): p. 961-&.

27. Morales, J. and J. Santos-Pena, *Highly electroactive nanosized [alpha]-LiFeO(2).* Electrochemistry Communications, 2007. **9**(8): p. 2116-2120.

28. Ado, K., et al., *Preparation of LiFeO(2) with Alpha-NaFeO(2)-Type Structure Using a Mixed-Alkaline Hydrothermal Method.* Journal of the Electrochemical Society, 1997. **144**(7): p. L177-L180.

29. Meng, Y.S., et al., *Combining ab initio computation with experiments for designing new electrode materials for advanced lithium batteries: LiNi(1/3)Fe(1/6) Co(1/6)Mn(1/3)O(2).* Journal of the Electrochemical Society, 2004. **151**(8): p. A1134-A1140.

30. Reimers, J.N., et al., *Structure and electrochemistry of Li(x)Fe(y)Ni(1-y)O(2).* Solid State Ionics, 1993. **61**(4): p. 335-344.

31. Chappel, E., et al., *Magnetic properties of LiNi(1-y)Fe(y)O(2).* Solid State Ionics, 2003. **159**(3-4): p. 273-278.

32. Mueller-Neuhaus, J.R., R.A. Dunlap, and J.R. Dahn, *Understanding Irreversible Capacity in Li(x)Ni(1-y)Fe(y)O(2) Cathode Materials.* Journal of The Electrochemical Society, 2000. **147**(10): p. 3598-3605.

33. Delmas, C., et al., *An overview of the Li(Ni,M)O(2) systems: syntheses, structures and properties.* Electrochimica Acta, 1999. **45**(1-2): p. 243-253.

34. Chick, L.A., et al., *Glycine-nitrate combustion synthesis of oxide ceramic powders.* Materials Letters, 1990. **10**(1-2): p. 6-12.

35. Larson, A.C. and R.B. Von Dreele, *General Structure Analysis System (GSAS).* Los Alamos National Laboratory Report LAUR, 2000. **86**: p. 748.

36. Toby, B.H., *EXPGUI, a graphical user interface for GSAS.* J. Appl. Cryst., 2001. **34**: p. 210-213.

37. Buta, S., et al., *Phase separation tendencies of aluminum-doped transition-metal oxides LiAl(1-x)M(x)O(2) in the alpha-NaFeO(2) crystal structure.* Journal of the Electrochemical Society, 1999. **146**(12): p. 4335-4338.

38. Jang, Y.I., et al., *Synthesis and characterization of LiAl(y)Co(1-y)O(2) and LiAl(y) Ni(1-y)O(2).* Journal of Power Sources, 1999. **82**: p. 589-593.

39. Gummow, R.J., et al., *Structure and electrochemistry of lithium cobalt oxide synthesised at 400C.* Materials Research Bulletin, 1992. **27**(3): p. 327-337.

40. Julien, C., et al., *Combustion synthesis and characterization of substituted lithium cobalt oxides in lithium batteries.* Solid State Ionics, 2000. **135**(1-4): p. 241-248.

41. Julien, C., *Structure, morphology and electrochemistry of doped lithium cobalt oxides.* Ionics, 2000. **6**(5): p. 451-460.

42. Moore, R.K. and W.B. White, *Study of Order-Disorder in Rock-Salt-Related Structures by Infrared Spectroscopy.* Journal of the American Ceramic Society, 1970. **53**(12): p. 679-682.

43. Julien, C. and M. Massot, *Spectroscopic studies of the local structure in positive electrodes for lithium batteries.* Physical Chemistry Chemical Physics, 2002. **4**(17): p. 4226-4235.

44. Sathiyamoorthi, R. and T. Vasudevan, *Synthesis and electrochemical behavior of nanosized LiNi(1-x)Ca(x)O(2) cathode materials for high voltage secondary lithium-ion cells.* Materials Research Bulletin, 2007. **42**(8): p. 1507-1517.

45. Julien, C., G.A. Nazri, and A. Rougier, *Electrochemical performances of layered LiM(1-y)M'(y)O(2) (M = Ni, Co; M' = Mg, Al, B) oxides in lithium batteries.* Solid State Ionics, 2000. **135**(1-4): p. 121-130.

46. Kalyani, P., et al., *Studies on LiNi(0.7)Al(0.3-x)Co(x)O(2) solid solutions as alternative cathode materials for lithium batteries.* Materials Research Bulletin, 2004. **39**(1): p. 41-54.

47. Julien, C., et al., *Layered LiNi(1−y)Co(y)O(2) compounds synthesized by a glycine-assisted combustion method for lithium batteries.* Journal of Materials Science, 2002. **37**(11): p. 2367-2375.

48. Amdouni, N., et al., *LiAl(y)Co(1-y)O(2) (0<y<0.3) intercalation compounds synthesized from the citrate precursors.* Materials Chemistry and Physics, 2003. **80**(1): p. 205-214.

49. Deb, A., et al., *In situ X-ray absorption spectroscopic study of Li(1.05)Ni(0.35) Co(0.25)Mn(0.4)O(2) cathode material coated with LiCoO(2).* Journal of the Electrochemical Society, 2007. **154**(6): p. A534-A541.

50. Tsai, Y.W., et al., *In-situ X-ray absorption spectroscopic study on variation of electronic transitions and local structure of LiNi(1/3)Co(1/3)Mn(1/3)O(2) cathode material during electrochemical cycling.* Chemistry of Materials, 2005. **17**(12): p. 3191-3199.

51. Koyama, Y., et al., *Crystal and electronic structures of superstructural Li(1-x) Co(1/3)Ni(1/3)Mn(1/3)O(2) (0<x<1).* Journal of Power Sources, 2003. **119**: p. 644-648.

52. Hwang, B.J., et al., *A combined computational/experimental study on LiNi(1/3) Co(1/3)Mn(1/3)O(2).* Chemistry of Materials, 2003. **15**(19): p. 3676-3682.

53. Choi, J. and A. Manthiram, *Role of chemical and structural stabilities on the electrochemical properties of layered LiNi(1/3)Mn(1/3)Co(1/3)O(2) cathodes.* Journal of the Electrochemical Society, 2005. **152**(9): p. A1714-A1718.

54. Shaju, K.M., G.V. Subba Rao, and B.V.R. Chowdari, *Performance of layered LiNi(1/3)Co(1/3)Mn(1/3)O(2) as cathode for Li-ion batteries.* Electrochimica Acta, 2002. **48**(2): p. 145-151.

55. Zhao, X.M., F. Zhou, and J.R. Dahn, *Phases formed in Al-doped Ni(1/3)Mn(1/3) Co(1/3)(OH)(2) prepared by coprecipitation: Formation of layered double hydroxide.* Journal of the Electrochemical Society, 2008. **155**(9): p. A642-A647.

56. Peres, J.P., et al., *The relationship between the composition of lithium nickel oxide and the loss of reversibility during the first cycle.* Journal of Physics and Chemistry of Solids, 1996. **57**(6-8): p. 1057-1060.

57. Delmas, C., et al., *On the behavior of the Li(x)NiO(2) system: an electrochemical and structural overview.* Journal of Power Sources, 1997. **68**(1): p. 120-125.

58. Van der Ven, A. and G. Ceder, *Lithium diffusion mechanisms in layered intercalation compounds.* Journal of Power Sources, 2001. **97-8**: p. 529-531.

59. Van der Ven, A. and G. Ceder, *Lithium Diffusion in Layered Li(x)CoO(2).* 2000. **3**(7): p. 304.

60. Davidson, I., et al., *Structure of 1T-Li(2)NiO(2) from powder neutron diffraction.* Solid State Ionics, 1991. **46**(3-4): p. 243-247.

61. Dahn, J.R., U. von Sacken, and C.A. Michal, *Structure and electrochemistry of Li(1+/-y)NiO(2) and a new Li(2)NiO(2) phase with the Ni (OH)(2) structure.* Solid State Ionics, 1990. **44**(1-2): p. 87-97.

62. Kang, S.-H., et al., *Investigating the first-cycle irreversibility of lithium metal oxide cathodes for Li batteries.* Journal of Materials Science, 2008. **43**(14): p. 4701-4706.

63. Choi, J. and A. Manthiram, *Investigation of the Irreversible Capacity Loss in the Layered LiNi(1/3)Mn(1/3)Co(1/)]O(2) Cathodes.* Electrochemical and Solid-State Letters, 2005. **8**(8): p. C102-C105.

64. Arai, H., et al., *Reversibility of LiNiO(2) cathode.* Solid State Ionics, 1997. **95**(3-4): p. 275-282.

65. Patoux, S. and M.M. Doeff, *Direct synthesis of LiNi(1/3)Co(1/3)Mn(1/3)O(2) from nitrate precursors.* Electrochemistry Communications, 2004. **6**(8): p. 767-772.

66. Molenda, J., A. Stoklosa, and T. Bak, *Modification in the electronic structure of cobalt bronze Li(x)CoO(2) and the resulting electrochemical properties.* Solid State Ionics, 1989. **36**(1-2): p. 53-58.

67. Molenda, J., P. Wilk, and J. Marzec, *Transport properties of the LiNi(1-y)Co(y)O(2) system.* Solid State Ionics, 1999. **119**(1-4): p. 19-22.

68. Molenda, J., P. Wilk, and J. Marzec, *Structural, electrical and electrochemical properties of LiNiO(2).* Solid State Ionics, 2002. **146**(1-2): p. 73-79.

69. Molenda, J., P. Wilk, and J. Marzec, *Electronic and electrochemical properties of Li(x)Ni(1-y)Co(y)O(2) cathode material.* Solid State Ionics, 2003. **157**(1-4): p. 115-123.

70. Wilk, P., J. Marzec, and J. Molenda, *Structural and electrical properties of LiNi(1-y) Co(y)O(2).* Solid State Ionics, 2003. **157**(1-4): p. 109-114.

71. Wen, C.J., et al., *Thermodynamic and Mass Transport Properties of ``LiAl''.* Journal of The Electrochemical Society, 1979. **126**(12): p. 2258-2266.

72. Weppner, W. and R.A. Huggins, *Electrochemical Methods for Determining Kinetic-Properties of Solids.* Annual Review of Materials Science, 1978. **8**: p. 269-311.

73. Weppner, W. and R.A. Huggins, *Determination of the Kinetic Parameters of Mixed-Conducting Electrodes and Application to the System Li(3)Sb.* Journal of The Electrochemical Society, 1977. **124**(10): p. 1569-1578.

74. Shaju, K.M., G.V.S. Rao, and B.V.R. Chowdari, *Influence of Li-ion kinetics in the cathodic performance of layered LiNi(1/3)Co(1/3)Mn(1/3)O(2).* Journal of the Electrochemical Society, 2004. **151**(9): p. A1324-A1332.

75. Newman, J. and K. Thomas-Alyea, *Electrochemical Systems*. 2004, Hoboken, NJ: John Wiley & Sons, Inc.

76. Hong, J.-S. and J.R. Selman, *Relationship Between Calorimetric and Structural Characteristics of Lithium-Ion Cells II. Determination of Li Transport Properties.* Journal of the Electrochemical Society, 2000. **147**(9): p. 3190-3194.

77. Shaju, K.M., G.V.S. Rao, and B.V.R. Chowdari, *Electrochemical Kinetic Studies of Li-Ion in O2-Structured Li(2/3)Ni(1/3)Mn(2/3)O(2) and Li(2/3+x)Ni(1/3) Mn(2/3)O(2) by EIS and GITT.* Journal of the Electrochemical Society, 2003. **150**(1): p. A1-A13.

78. Shaju, K.M., G.V.S. Rao, and B.V.R. Chowdari, *Li ion kinetic studies on spinel cathodes, LiM(1/6)Mn(11/6)O(4) (M = Mn, Co, CoAl) by GITT and EIS.* Journal of Materials Chemistry, 2003. **13**(1): p. 106-113.

79. Prado, G., et al., *Cationic distribution in the Li(1-z)[Ni(1-y)Fe(y)](1+z)O(2) electrode materials.* Journal of Materials Chemistry, 2000. **10**(11): p. 2553-2560.

80. Ohzuku, T., et al., *Materials strategy for advanced lithium-ion (shuttlecock) batteries: lithium nickel manganese oxides with or without cobalt.* Electrochemistry, 2005. **73**(1): p. 2-11.

5. Physical Properties of Transition Metal Olivines

5.1 Abstract

This chapter serves as a brief overview of the use of transition metal olivines, in particular $LiFePO_4$, as positive electrode materials in lithium ion batteries. The structure, transport properties, electrochemistry and synthesis are discussed. In addition, the production and characterization of carbon coated olivine particles is outlined with an emphasis on the use of Raman spectroscopy to probe local carbon structure.

5.2 Introduction

Driven by increasing concerns over the high cost and limited thermal stability of $LiCoO_2$ electrodes, there has been a large push to identify new structural classes of materials for future lithium ion batteries. Arguably, the most viable success of these efforts has been the discovery of the electrochemical activity of transition metal olivines, namely $LiFePO_4$.[1] $LiFePO_4$ is comprised of naturally abundant elements and holds the potential of being a low cost, environmentally benign electrode material depending on the synthetic method used to produce it. Limited by an extremely low electronic (10^{-10} S/cm) and ionic conductivity (~10^{-13} S/cm), a significant amount of particle engineering has been developed to allow the use of $LiFePO_4$ in commercial cells. As will be discussed later, $LiFePO_4$ possesses excellent abuse tolerance, although a limited energy density may inhibit its use in some applications.

5.3 Structure

$LiFePO_4$ is a naturally occurring mineral (triphyllite) and is a prototypical member of the ordered olivine family ($(Mg,Fe)_2SiO_4$).[2] $LiFePO_4$ crystallizes in the *Pmnb* space group with an orthorhombic unit cell containing four formula units (Figure 5.1). The oxygen ions form a nearly hexagonal close packed (hcp) array with the distortion arising

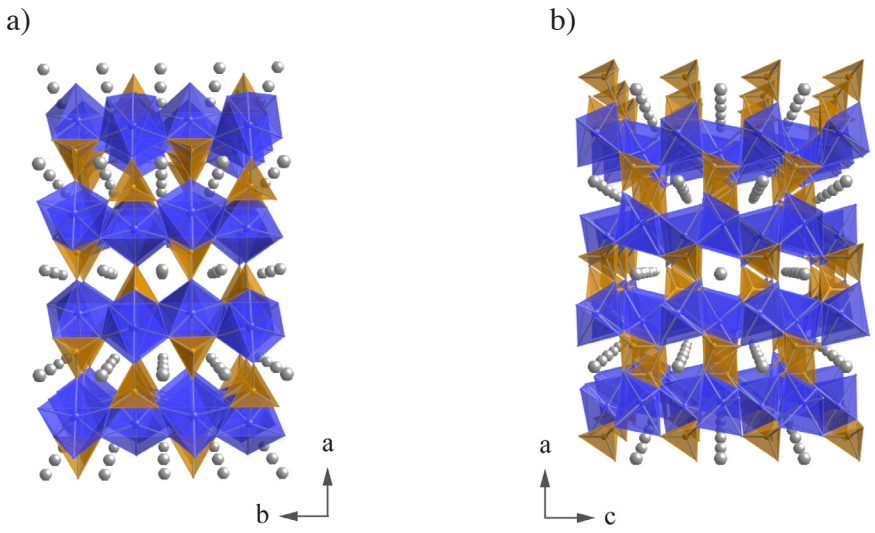

Figure 5.1: Crystal structure of $LiFePO_4$ indexed in the *Pnmb* space group looking down the (a) [001] and (b) [010] directions. Lithium ions are shown as gray spheres, iron octahedra are blue, and PO_4 tetrahedra are gold.

from the minimization of cation-cation electrostatic interactions.[1] Lithium ions occupy the M1 position and form edge-sharing, octahedrally coordinated chains in the [100] direction. Fe^{2+} ions reside on the M2 site in six fold coordination and form edge-sharing networks in the (010) plane.[3, 4] Extraction of lithium occurs via a first-order phase transformation forming orthorhombic $FePO_4$ (heterosite).[3, 5]

Recently, with knowledge gained from the work of Delacourt *et al.* that showed a temperature driven solid solution of Li_xFePO_4 ($0 \leq x \leq 1$) at 450° C, the solubility of lithium in either end member, $LiFePO_4$ or $FePO_4$, has been closely re-examined.[6, 7] Room temperature neutron diffraction experiments have revealed two solid solution regions in Li_xFePO_4, characterized as $Li_\alpha FePO_4$ and $Li_{1-\beta}FePO_4$.[8] The parameters α and β were found to have values of 0.05 and 0.89, respectively, in materials with a 100 nm particle size.[8] The extent of the solid solution domain is found to be an inverse function of the particle size and has been explained as a result of changes in the surface energy or stress of the phase boundary in small particles.[9] The existence of phases with mixed Fe^{2+}/Fe^{3+} oxidation

states as well as lithium ions and vacancies intermixed on the M1 site, may be vital to the operation of $LiFePO_4$ electrodes. As both $LiFePO_4$ and $FePO_4$ are poor electronic and ionic conductors, a region of even limited lithium (or vacancy) solubility may explain the ability of $LiFePO_4$ electrodes to be cycled at high rates.

Lithium conductivity in $LiFePO_4$ is highly limited and estimated to be on the order of 10^{-13} S/cm.[10] Lithium motion through the lattice is accomplished via a hopping mechanism between adjacent M1 sites in the [010] direction of the crystal structure. The tunnels through which lithium transport occurs are highly one-dimensional and can clearly be seen in Figure 5.1b. Due to anisotropic lithium ion vibrations in the [010] direction, the actual diffusion pathway is expected to be a one-dimensional curved chain.[11] An activation energy of 0.27 eV has been calculated for lithium diffusion along the *b*-axis through an intermediate tetrahedral vacancy.[12] The next lowest energy pathway for lithium diffusion, through face sharing octahedral vacancies in the *c*-axis direction, is expected to have an activation energy nearly an order of magnitude higher than along the *b*-axis.[12] Further microscopic evidence of the directional nature of lithium transport and the two-phase reaction zone has been reported by Chen *et al.*[13] Transmission electron microscopy experiments on large single crystal particles revealed disordered phase boundaries in the *ac* plane between $LiFePO_4$ and $FePO_4$ domains. Upon lithium extraction the phase boundary between the domains moved along the *a*-axis at dislocation lines running parallel to the *c*-axis. These results further emphasize the limited dimensionality of lithium transport in the olivine system and have large implications for the particle engineering of high performance $LiFePO_4$ materials.

$LiFePO_4$ has been experimentally determined to be an electronic insulator with an electronic conductivity on the order of 10^{-10} S/cm at room temperature.[14,15] Electron transport occurs by the thermally activated hopping of small polarons between iron centers. Excess charge carriers, either Fe^{3+} hole states in $Li_{1-\beta}FePO_4$ or filled Fe^{2+} electron states in $Li_{\alpha}FePO_4$, induce local lattice distortions that trap the charge carrier.[16] Reported activation

energies have varied widely, e.g., 0.39-0.5 eV,[17] 0.54-0.65 eV,[14] and 0.775 eV[18]. These values are highly dependent upon the sample preparation and measurement method used in the experiment. Such inconsistencies suggest that the impact of secondary components, such as grain boundaries or surface impurities, may be significant in some materials. Using first principle methods, the activation energy of a free polaron has been calculated to be as low as 0.215 eV in $LiFePO_4$ and 0.175 eV in $FePO_4$ indicating that the intrinsic mobility of charge carriers is quite high.[16] However, strong interactions between the charge carrying defect and either lithium ions or lithium vacancies strongly limit polaron mobility.

There has been significant debate as to whether $LiFePO_4$, typically viewed as a thermodynamic line phase, can be aliovalently doped with elements such as Nb^{5+}.[3] Doping allows for the formation of phases with mixed Fe^{2+}/Fe^{3+} oxidation states and, presumably, elevated electronic conductivity. However, evidence of increased electronic conductivity in doped and undoped $LiFePO_4$ samples has been related to the formation of interconnected impurity phases (such as Fe_2P, and $Fe_{75}P_{15}C_{10}$).[19]

5.4 Electrochemistry

In an electrochemical cell lithium extraction and intercalation occur via a two-phase reaction between $LiFePO_4$ and $FePO_4$ (ignoring any solid solution behavior for simplicity) (Equation 5.1). The reaction occurs at a potential of 3.4 V vs. Li/Li^+ and has a theoretical capacity of 170 mAh/g if all of the lithium is utilized. According to the Gibbs

$$LiFePO_4 - xLi^+ - xe^- \leftrightarrow xFePO_4 + (1-x)LiFePO_4 \qquad \text{Eq. 5.1}$$

phase rule, a binary system operating under constant temperature and pressure conditions and containing two phases has no degrees of freedom. Therefore, the potential is fixed for all compositions and the system exhibits a characteristic flat voltage profile (Figure 5.2).

The reaction potential of 3.4 V versus Li/Li^+ is substantially higher than other active materials operating on the $Fe^{2+/3+}$ redox couple. The shift of the $Fe^{2+/3+}$ oxidation

states in $LiFePO_4$ is often explained in terms of an induction effect resulting from the high electronegativity of the PO_4^{3-} structural units.[20] However, an induction effect does not explain the elevated redox potential of $LiFePO_4$ relative to other phosphates, such as $Li_3Fe_2(PO_4)_3$ that reacts at a potential near 2.8 V versus Li/Li^+.[21] Padhi *et al.*[21] attributed the increased potential to an increase in the cation-cation interactions in the ordered olivine structure resulting from the prevalence of edge sharing ochtahedra units. These interactions raise the Fe^{2+}/Fe^{3+} redox level in $LiFePO_4$ relative to other phosphate structures with significantly weaker cation interactions.[21]

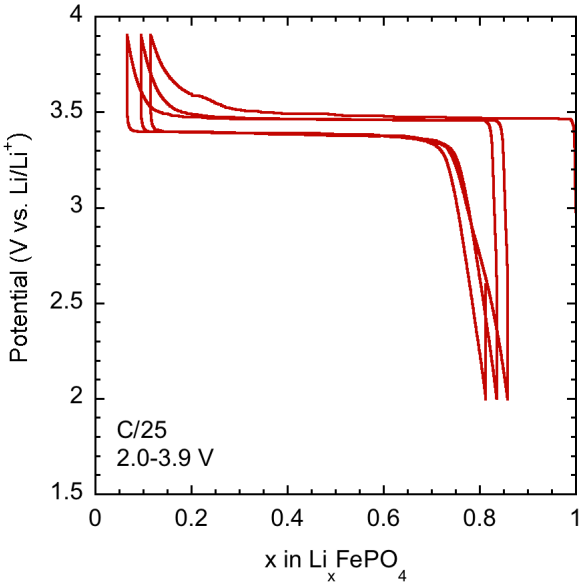

Figure 5.2: Cycling curve of a $Li/LiFePO_4$ cell showing the flat voltage plateau at ~3.4 V characteristic of the two-phase reaction. Cell was cycled between 2.0 and 3.9 V at a rate of C/25.

5.5 Synthesis

Numerous methods have been used to produce $LiFePO_4$ powders including solid-state,[1, 22] sol-gel,[23-27] hydrothermal,[28-30] microwave,[31] mechanochemical,[32] mechanical,[33] and precipitation[34] based techniques. Care must be taken in low temperature synthetic methods, such as hydrothermal, to prevent the formation of materials with mixed lithium and iron occupancy on the M1 and M2 sites. As lithium diffusion is one dimensional, any

iron residing on the M1 site effectively blocks lithium motion through the lattice, severely limiting the electrochemical activity. Additionally, the use of reducing agents, such as hydrazine or ascorbic acid, in the hydrothermal method has been shown to inhibit the formation of ferric surface films and improve performance.[30]

5.6 Stability

One of the distinct advantages of $LiFePO_4$ over layered oxide positive electrode materials is the vastly superior thermal abuse tolerance. The strongly bonded PO_4^{3-} units form a robust structural backbone that is relatively unaffected by lithium extraction. This allows the olivine structure to be maintained even at low lithium contents with no evidence of oxygen evolution or other detrimental side reactions. Differential scanning calorimetry (DSC) experiments on Li_xFePO_4 powders in contact with a variety of electrolyte salts ($LiPF_6$, $LiBF_4$, $LiAsF_6$) and solvents (ethylene carbonate/dimethyl carbonate (EC/DMC), and ethylene carbonate/propylene carbonate (PC/DMC)) at different states of charge, reveal negligible exothermic reactions below 340-400° C.[35, 36] By comparison, Li_xNiO_2 charged to 4.3 V versus Li/Li^+ shows a strong exothermic behavior at temperatures below 190° C that has been related to oxygen release from the crystal structure.[37, 38] Accelerating rate calorimetry (ARC) by Jiang *et al.* reveals an onset temperature in excess of 300° C when the fully charged material is in contact with ethylene carbonate/diethyl carbonate (EC/DEC).[39, 40] The onset temperature of self-sustaining exotherms is highly sensitive to the electrolyte salt used in the experiment. When 1 M $LiPF_6$ is added to the solution the onset temperature decreases to 190° C, but only to 240° C when in contact with 0.8 M lithium bis(oxalato)borate (LiBOB) electrolyte solutions.[39, 40] Perhaps most importantly, the thermal behavior of $LiFePO_4$ is found to be insensitive to the particle size.[39] This allows for the use of small particles to overcome kinetic and transport limitations without sacrificing the safety of the system due to an increased active material surface area.

5.7 Carbon Coating

While $LiFePO_4$ exhibits great thermal and cycling stability, its low density (3.6 g/cm^3) leads to a limited volumetric energy density (by comparison $LiCoO_2$ has a density of 5.1 g/cm^3).[41] For example, commercial layered oxide based cells have volumetric energy densities exceeding 450 Wh/L, whereas $LiFePO_4$ based cells are on the order of ~200 Wh/L.[10, 42] Amplifying this deficiency is the fact that a significant amount of carbon black and graphite must be added to the active material to achieve optimal electrochemical performance. Carbon black and graphite, with densities of 1.8 and 2.2 g/cm^3 respectively, serve to further reduce the volumetric energy densities of composite $LiFePO_4$ electrodes. In an effort to minimize the amount of carbon that has to be added to the electrode structure, a significant amount of research has focused on developing carbon coated $LiFePO_4$ powders. By directly coating the active material with a thin layer of carbon, the total amount of carbon in the cell can be reduced while maintaining a composite conductivity conducive to high power electrodes.

Numerous experimental methods have been used to create $LiFePO_4$/C composite materials. Most procedures are based on the thermal decomposition of an organic additive that is added to the $LiFePO_4$ powder before a final thermal treatment below ~700° C. The organic additives used include, but are not limited to, sucrose,[43, 44] acetylene black,[33] various organic carboxylic acids,[23, 26, 45] organic anhydrides,[46] and organic nitriles.[46] Regardless of the carbon source, care must be taken to maintain carbon loadings below 1-2 wt.% due to the negative impact of carbon coatings on the tap density.[43]

5.8 Raman Spectroscopy of Carbon Coatings

To produce composite $LiFePO_4$/C composites with high conductivity and minimum carbon content, it is of vital importance to control the underlying structure of the carbon coating. The conductivity of carbon is highly sensitive to both the local and long-range bonding structure (either crystalline or amorphous). Diamond-like carbon, is

comprised of sp^3 bonded carbon, exhibits very low electronic conductivity (~10^{-13} S/cm), and is undesirable in this application.[47] Alternatively, crystalline graphitic carbon exhibits extremely high electronic conductivities (~$10^{4\text{-}5}$ S/cm)[48] due to the unbound electron in the p_z orbital that is free to migrate in the basal plane. The morphology of the carbon film also plays a large role in determining the ultimate conductivity of the material. Carbon structures that are comprised of large graphite flakes can exhibit metallic conduction due to the high conductivity within the basal plane of graphite sheets. Carbon black, which is comprised of small graphitic domains in an amorphous carbon field, possesses lower electronic conductivity and is highly sensitive to the fraction and orientation of each phase. The amorphous carbon can be comprised of either sp^2 or sp^3 carbon and the decrease in electronic conduction has been related to charge localization.[48]

Carbon films formed at low temperature via the pyrolytic decomposition of organic moieties can have a very complex, non-homogeneous structure. Therefore, careful characterization is required in order to relate the underlying carbon structure to the composite electronic behavior. One of the best methods to characterize such films is Raman spectroscopy.[49, 50] Raman spectroscopy is based on the inelastic scattering of photons by solids or molecules. Photons of energy $\hbar\nu_0$, incident on a material can be elastically or in-elastically scattered provided they do not possess the energy to induce an electronic transition.[50] The elastically scattered photon has the same frequency of the incident beam and is termed Rayleigh scattering. Due to the interaction of photons with the vibrational modes of the structure, a small portion (on the order of 10^{-8} the intensity of the excitation beam) may be scattered at a frequency different than that of the incident beam. If the incident beam excites a molecular vibration, the scattered beam will lose an amount of energy equivalent to the energy imparted to the specimen. The frequency of the resulting photon is decreased and is termed Stokes scattering. If a molecule that is in an excited state adsorbs an incoming photon and subsequently relaxes a photon of increased frequency is emitted and is termed anti-Stokes scattering.

For single crystal graphite (space group D_{6h}^4), group factor analysis predicts two Raman active vibrational modes of E_{2g} symmetry.[50] Both modes correspond to the in-plane vibrations of carbon atoms and are observed at 42 cm^{-1} and 1580 cm^{-1}, respectively. While the mode at 42 cm^{-1} is often difficult to discern due to its close proximity to the Rayleigh band, the peak at 1580 cm^{-1} can be quite strong and is termed the G-band (Figure 5.3). The Raman spectra of other mixed graphite materials including (carbon black and amorphous carbon) include an additional peak at ~1330 cm^{-1} that is not expected from

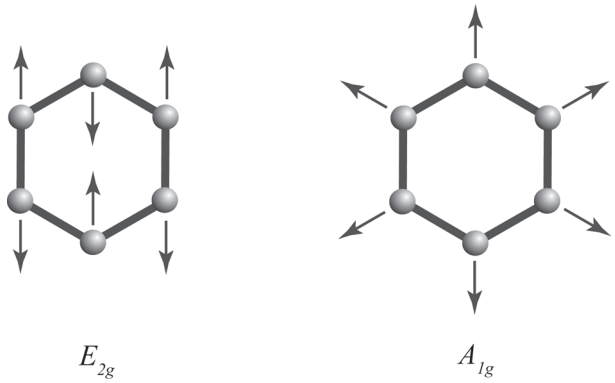

Figure 5.3: Raman active vibrational modes of graphite. The G band is associated with E_{2g} vibrational mode and the D band with the A_{1g} radial breathing mode.

group factor analysis of the infinite crystal. This band is termed the D-band and arises from the breathing mode (A_{1g} symmetry) of sp^2 bound carbon rings near edges and defects in the graphene sheet (Figure 5.3).[51] The intensity of the D-band is therefore, a measure of both the amount of disordered carbon and the graphite crystallite size.[50] In addition to the two peaks associated with graphitic sp^2 carbon, two additional bands can arise in disordered carbons resulting from the presence of sp^3-like carbon. The bands are observed in the 1000-1600 cm^{-1} region and are often very diffuse.[52, 53]

Using Raman spectroscopy the electronic conductivity of carbon films can be related to the relative ratio of the D- and G-bands of the Raman spectra. As an example

of the relationship between the D- and G-bands of the carbon spectra, and the electronic conductivity, the Raman spectra of MAG-10 graphite and acetylene black are presented in Figure 5.4. MAG-10 graphite is a highly graphitic, flaky carbon material with large graphite domains and has an electronic conductivity on the order of 1 S/cm. Accordingly, the Raman spectrum (Figure 5.4 (a)) is dominated by the G-band with a very small D-band at lower wavenumbers. On the other hand, acetylene black is composed of mixed graphite and amorphous carbon domains that contain both sp^2 and sp^3 carbon. The conductivity is several orders of magnitude lower (~10^{-4} S/cm) than in MAG-10 due to the decreased graphite domain size and phase fraction. For the same reasons, the D-band becomes the dominant feature in the Raman spectrum of acetylene black (Figure 5.4 (b)). A characteristic de-convolution of a graphite-like carbon is shown in Figure 5.5 in which both sp^2 and sp^3 carbon are accounted for. Therefore, the relative change in the graphitic character of a carbon film can be measured by either a D/G ratio, or alternatively, an sp^2/sp^3 ratio.

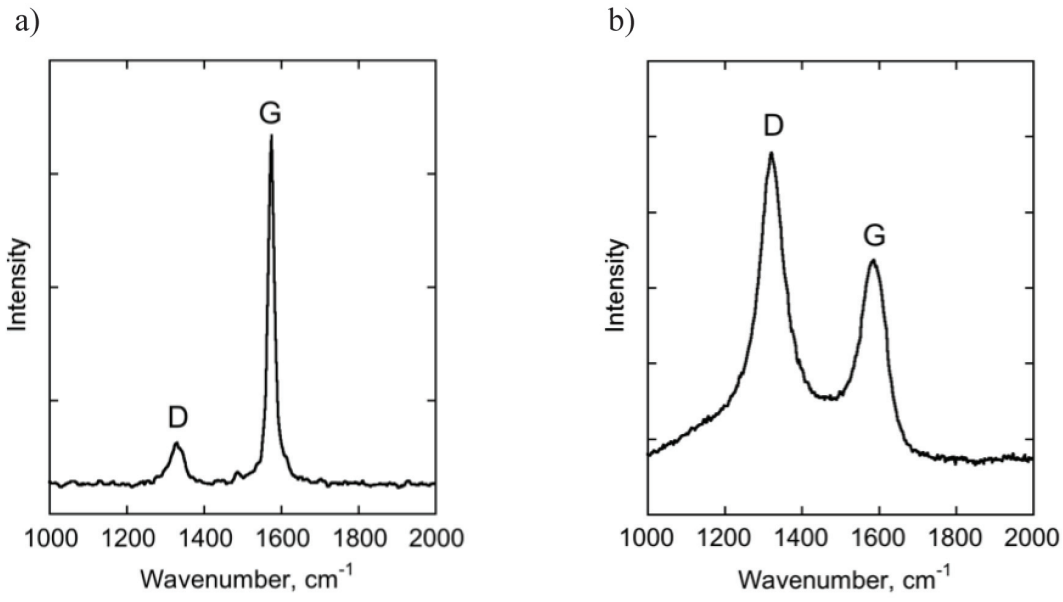

Figure 5.4: Raman spectra of (a) MAG-10 graphite and (b) acetylene black powders. (Spectra courtesy of R. Kostecki, Lawrence Berkeley National Laboratory)

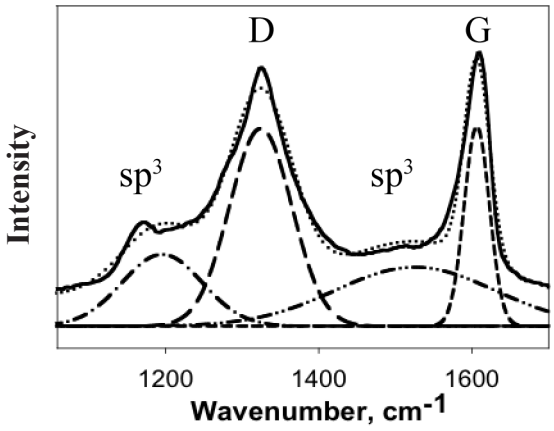

Figure 5.5: De-convoluted Raman signal of carbon film. The D and G bands of the graphtic carbon is clearly visible in addition to two peaks arising from *sp*^{3} bonded carbon.

5.9 Conclusions

$LiFePO_4$ is a very promising positive electrode material for use in future generations of lithium ion batteries because of its potential low cost and toxicity. However, the low specific density of $LiFePO_4$ limits its use to applications in which high volumetric energy densities are not required. As will be discussed in the subsequent chapters, $LiFePO_4$ can be engineered to be a high rate positive electrode material when the particle size is reduced and a high quality carbon coating is employed. The exceptional thermal abuse and cycle life properties of $LiFePO_4$ make it an ideal electrode material for many high power applications where safety is at a premium.

5.10 References

1. Padhi, A.K., K.S. Nanjundaswamy, and J.B. Goodenough, *Phospho-olivines as Positive-Electrode Materials for Rechargeable Lithium Batteries.* Journal of the Electrochemical Society, 1997. **144**(4): p. 1188-1194.

2. Ravet, N., et al., *Electroactivity of natural and synthetic triphylite.* Journal of Power Sources, 2001. **97-98**: p. 503-507.

3. Chung, S.-Y., J.T. Bloking, and Y.-M. Chiang, *Electronically conductive phospho-olivines as lithium storage electrodes.* Nat Mater, 2002. **1**(2): p. 123-128.

4. Rousse, G., et al., *Magnetic Structures of the Triphylite LiFePO(4) and of Its Delithiated Form FePO(4).* Chem. Mater., 2003. **15**(21): p. 4082-4090.

5. Andersson, A.S., et al., *Lithium extraction/insertion in LiFePO(4): an X-ray diffraction and M^ssbauer spectroscopy study.* Solid State Ionics, 2000. **130**(1-2): p. 41-52.

6. Delacourt, C., et al., *The existence of a temperature-driven solid solution in Li(x) FePO(4) for 0<x<1.* Nat Mater, 2005. **4**(3): p. 254-260.

7. Chen, G., X. Song, and T.J. Richardson, *Metastable Solid-Solution Phases in the LiFePO(4)/FePO(4) System.* Journal of the Electrochemical Society, 2007. **154**(7): p. A627-A632.

8. Yamada, A., et al., *Room-temperature miscibility gap in Li(x)FePO(4).* Nature Materials, 2006. **5**(5): p. 357-360.

9. Meethong, N., et al. *Size-dependent lithium miscibility gap in nanoscale Li(1-x) FePO(4)*. 2007: Electrochemical Soc Inc.

10. Yu, D.Y.W., et al., *Effect of Electrode Parameters on LiFePO(4) Cathodes.* Journal of the Electrochemical Society, 2006. **153**(5): p. A835-A839.

11. Nishimura, S., et al., *Experimental visualization of lithium diffusion in Li(x)FePO4.* Nature Materials, 2008. **7**(9): p. 707-711.

12. Morgan, D., A. Van der Ven, and G. Ceder, *Li Conductivity in Li(x)MPO(4) (M = Mn, Fe, Co, Ni) Olivine Materials.* Electrochemical and Solid-State Letters, 2004. **7**(2): p. A30-A32.

13. Chen, G., X. Song, and T.J. Richardson, *Electron Microscopy Study of the LiFePO(4) to FePO(4) Phase Transition.* Electrochemical and Solid-State Letters, 2006. **9**(6): p. A295-A298.

14. Delacourt, C., et al., *Toward Understanding of Electrical Limitations (Electronic, Ionic) in LiMPO(4) (M = Fe, Mn) Electrode Materials.* Journal of The Electrochemical Society, 2005. **152**(5): p. A913-A921.

15. Shi, S., et al., *Enhancement of electronic conductivity of LiFePO(4) by Cr doping and its identification by first-principles calculations.* Physical Review B, 2003. **68**(19): p. 195108.

16. Maxisch, T., F. Zhou, and G. Ceder, *Ab initio study of the migration of small polarons in olivine Li(x)FePO(4) and their association with lithium ions and vacancies.* Physical Review B (Condensed Matter and Materials Physics), 2006. **73**(10): p. 104301-6.

17. Xu, Y.-N., et al., *Electronic Structure and Electrical Conductivity of Undoped LiFePO(4).* Electrochemical and Solid-State Letters, 2004. **7**(6): p. A131-A134.

18. Ellis, B., et al., *Small Polaron Hopping in Li(x)FePO4 Solid Solutions: Coupled Lithium-Ion and Electron Mobility.* J. Am. Chem. Soc., 2006. **128**(35): p. 11416-11422.

19. Herle, P.S., et al., *Nano-network electronic conduction in iron and nickel olivine phosphates.* Nat Mater, 2004. **3**(3): p. 147-152.

20. Molenda, J., *Lithium-ion batteries - state of art Novel phospho-olivine cathode materials.* Materials Science-Poland, 2006. **24**(1): p. 61-67.

21. Padhi, A.K., et al., *Effect of structure on the Fe(3+)/Fe(2+) redox couple in iron phosphates.* Journal of the Electrochemical Society, 1997. **144**(5): p. 1609-1613.

22. Koltypin, M., et al., *More on the performance of LiFePO(4) electrodes - The effect of synthesis route, solution composition, aging, and temperature.* Journal of Power Sources, 2007. **174**(2): p. 1241-1250.

23. Doeff, M.M., et al., *Optimization of carbon coatings on LiFePO(4).* Journal of Power Sources, 2006. **163**(1): p. 180-184.

24. Gabrisch, H., J. Wilcox, and M.M. Doeff, *TEM Studies of Carbon Coated LiFePO(4) After Charge Discharge Cycling.* ECS Transactions, 2007. **3**(36): p. 29-36.

25. Gabrisch, H., J.D. Wilcox, and M.M. Doeff, *Carbon Surface Layers on a High-Rate LiFePO(4).* Electrochemical and Solid-State Letters, 2006. **9**(7): p. A360-A363.

26. Wilcox, J.D., et al., *Factors Influencing the Quality of Carbon Coatings on LiFePO(4).* Journal of The Electrochemical Society, 2007. **154**(5): p. A389-A395.

27. Doeff, M.M., et al., *Effect of Surface Carbon Structure on the Electrochemical Performance of LiFePO(4).* Electrochemical and Solid-State Letters, 2003. **6**(10): p. A207-A209.

28. Yang, S.F., et al., *Reactivity, stability and electrochemical behavior of lithium iron phosphates.* Electrochemistry Communications, 2002. **4**(3): p. 239-244.

29. Yang, S.F., P.Y. Zavalij, and M.S. Whittingham, *Hydrothermal synthesis of lithium iron phosphate cathodes.* Electrochemistry Communications, 2001. **3**(9): p. 505-508.

30. Chen, J., S. Wang, and M.S. Whittingham, *Hydrothermal synthesis of cathode materials.* Journal of Power Sources, 2007. **174**(2): p. 442-448.

31. Murugan, A.V., T. Muraliganth, and A. Manthiram, *Comparison of microwave assisted solvothermal and hydrothermal syntheses of LiFePO(4)/C nanocomposite cathodes for lithium ion batteries.* Journal of Physical Chemistry C, 2008. **112**(37): p. 14665-14671.

32. Liao, X.-Z., et al., *A Novel Synthesis Route for LiFePO(4)/C Cathode Materials for Lithium-Ion Batteries.* Electrochemical and Solid-State Letters, 2004. **7**(12): p. A522-A525.

33. Kim, J.-K., et al., *Electrochemical properties of LiFePO(4)/C composite cathode material: Carbon coating by the precursor method and direct addition.* Journal of Physics and Chemistry of Solids, 2008. **69**(5-6): p. 1257-1260.

34. Delacourt, C., et al., *Size effects on carbon-free LiFePO(4) powders.* Electrochemical and Solid State Letters, 2006. **9**(7): p. A352-A355.

35. Takahashi, M., et al., *Reaction behavior of LiFePO(4) as a cathode material for rechargeable lithium batteries.* Solid State Ionics, 2002. **148**(3-4): p. 283-289.

36. Andersson, A.S., et al., *Thermal Stability of LiFePO(4)-Based Cathodes.* Electrochemical and Solid-State Letters, 2000. **3**(2): p. 66-68.

37. Dahn, J.R., et al., *Thermal stability of Li(x)CoO(2), Li(x)NiO(2) and lambda-MnO(2) and consequences for the safety of Li-ion cells.* Solid State Ionics, 1994. **69**(3-4): p. 265-270.

38. Cho, J., Jung, H., Park, Y., Kim, G., Lim, H.S., *Electrochemical Properties and Thermal Stablility of Li(a)Ni(1-x)Co(x)O(2) Cathode Materials.* Journal of the Electrochemical Society, 2000. **147**(1): p. 15-20.

39. Jiang, J. and J.R. Dahn, *ARC studies of the reaction between Li(0)FePO(4) and LiPF(6) or LiBOB EC/DEC electrolytes.* Electrochemistry Communications, 2004. **6**(7): p. 724-728.

40. Jiang, J. and J.R. Dahn, *ARC studies of the thermal stability of three different cathode materials: LiCoO(2); LiNi(0.1)Co(0.8)Mn(0.1)O(2); and LiFePO(4), in LiPF(6) and LiBoB EC/DEC electrolytes.* Electrochemistry Communications, 2004. **6**(1): p. 39-43.

41. Yonemura, M., et al., *Comparative kinetic study of olivine Li(x)MPO(4) (M = Fe, Mn).* Journal of the Electrochemical Society, 2004. **151**(9): p. A1352-A1356.

42. Broussely, M. and G. Archdale, *Li-ion batteries and portable power source prospects for the next 5-10 years.* Journal of Power Sources, 2004. **136**(2): p. 386-394.

43. Chen, Z. and J.R. Dahn, *Reducing Carbon in LiFePO(4)/C Composite Electrodes to Maximize Specific Energy, Volumetric Energy, and Tap Density.* Journal of the Electrochemical Society, 2002. **149**(9): p. A1184-A1189.

44. Bewlay, S.L., et al., *Conductivity improvements to spray-produced LiFePO(4) by addition of a carbon source.* Materials Letters, 2004. **58**(11): p. 1788-1791.

45. Fey, G.T.K., et al. *Carboxylic acid-assisted solid-state synthesis of LiFePO(4)/C composites and their electrochemical properties as cathode materials for lithium-ion batteries*. 2008: Springer.

46. Hu, Y., et al., *Electrochemical Performance of Sol-Gel Synthesized LiFePO(4) in Lithium Batteries.* Journal of the Electrochemical Society, 2004. **151**(8): p. A1279-A1285.

47. Muto, Y., et al., *Electrical conduction in undoped diamond films prepared by chemical vapor deposition.* Applied Physics Letters, 1991. **59**(7): p. 843-845.

48. Kinoshita, K., *Carbon : electrochemical and physicochemical properties*. 1988, New York: Wiley.

49. Casiraghi, C., A.C. Ferrari, and J. Robertson, *Raman spectroscopy of hydrogenated amorphous carbons.* Physical Review B (Condensed Matter and Materials Physics), 2005. **72**(8): p. 085401-14.

50. Hardwick, L., *In Situ Raman Microscopy of Insertion Electrodes for Lithium-Ion Batteries and Supercapacitors*. 2007, Swiss Federal Institute of Technology: Zurich.

51. Tuinstra, F. and J.L. Koenig, *Raman Spectrum of Graphite.* The Journal of Chemical Physics, 1970. **53**(3): p. 1126-1130.

52. Takabayashi, S., et al., *Annealing effect on the chemical structure of diamondlike carbon.* Journal of Applied Physics, 2008. **104**(4).

53. Kostecki, R., *Personal communication*. 2007.

6. Factors Influencing the Quality of Carbon Coatings on $LiFePO_4$

6.1 Abstract

Several $LiFePO_4$/C composites were prepared and characterized electrochemically in lithium half-cells. Pressed pellet conductivities correlated well with the electrochemical performance in lithium half-cells. It was found that carbon structural factors such as sp^2/sp^3, D/G, and H/C ratios, as determined by Raman spectroscopy and elemental analysis, influenced the conductivity and rate behavior strongly. The structure of the residual carbon could be manipulated through the use of additives during $LiFePO_4$ synthesis. Increasing the pyromellitic acid (PA) content in the precursor mix prior to calcination resulted in a significant lowering of the D/G ratio and a concomitant rise in the sp^2/sp^3 ratio of the carbon. Addition of both iron nitrate and PA resulted in higher sp^2/sp^3 ratios without further lowering the D/G ratios, or increasing carbon contents. The best electrochemical results were obtained for $LiFePO_4$ processed with both ferrocene and PA. The improvement is attributed to better decomposition of the carbon sources, as evidenced by lower H/C ratios, a slight increase of the carbon content (still below 2 wt.%), and more homogeneous coverage. A discussion of the influence of carbon content vs. structural factors on the composite conductivities and, by inference, the electrochemical performance, is included.[1-4]

6.2 Introduction

Significant attention has been directed towards developing $LiFePO_4$ as a possible replacement for $LiCoO_2$ in lithium-ion batteries, after the initial report by Padhi *et al.* in 1997.[5] Low toxicity, the potential for low cost, and excellent stability during normal cycling and storage conditions make this material particularly attractive for large-scale applications such as hybrid electric vehicles (HEVs) and electric vehicles (EVs). Charge and discharge proceeds via a two-phase reaction[6] between $LiFePO_4$ and $FePO_4$, giving

a flat discharge profile at ~3.45 V vs. Li/Li^+ and a reversible theoretical specific capacity of 170 mAh/g. $LiFePO_4$, however, suffers from low intrinsic rate capability, which has been ascribed to the slow diffusion of lithium ions across the two-phase boundary and low electronic conductivity, calculated to be about 10^{-9} S cm^{-1}.[7]

Numerous approaches directed at overcoming these problems have been described in the literature. These include the mixing in of fine metal particles,[8] systematic control of reaction parameters to control particle size and morphology,[9-12] and attempts at doping with supervalent cations in the lithium site to create a *p*-type semiconductor.[13] (Recent results[14] indicate, however, that true substitution does not occur; rather a nano-network of impurity phases including iron phosphides form, which enhances the pressed pellet conductivities considerably). One of the most promising avenues is the addition of conductive carbon either post-synthesis (e.g., by co-grinding),[15] or by co-firing with organic or polymeric additives to produce coated particles.[1, 16-18] To avoid decreasing the energy density unduly, the amount of carbon should be kept low.[19] An interesting observation is that electrode performance does not always track with the amount of carbon in $LiFePO_4$/C composites.[20] The structure of the carbon, particularly the sp^2/sp^3 and D/G (disordered/graphene) ratios, strongly influences the electronic conductivity. Samples containing smaller amounts of high-quality carbon (i.e., those having high sp^2/sp^3 and low D/G ratios) can outperform those containing larger amounts of a less-conductive coating. It has also been shown that the structure of the carbon in these composites produced by co-firing depends upon the source (i.e., type of organic or polymeric precursor), as well as the processing conditions.[21] Optimization of the carbon structure should allow the amount required to overcome the conductivity limitations of $LiFePO_4$ to be minimized. This paper describes our recent experimental work directed towards this goal.

The low temperatures (typically ~600-750° C) used in the preparation of $LiFePO_4$ present a challenge for the co-production of well-ordered, graphitic carbon *in-situ*.[21] Nevertheless, it is possible to manipulate the synthesis conditions to produce carbons

with more desirable characteristics. In particular, the judicious selection of carbon sources and graphitization catalysts can result in markedly improved coatings, as will be shown below.

6.3 Experimental Procedures

$LiFePO_4$ samples were made via a sol-gel synthesis using $Fe(NO_3)_3 \cdot 9H_2O$ (iron nitrate, Sigma Aldrich 98+%), $C_2H_3O_2Li \cdot 2H_2O$ (lithium acetate, Sigma Aldrich), and H_3PO_4 (phosphoric acid, EMP, 85%). The iron nitrate and lithium acetate were combined with the phosphoric acid in a stoichiometric ratio of 1:1:1. Distilled water was then added until all the constituents were completely dissolved. The solution was then slowly combined with two stoichiometric equivalents of $HOCH_2CO_2H$ (glycolic acid, Sigma Aldrich, 70% solution in water) and the pH was adjusted to between 8.5 and 9.5 using NH_4OH (ammonium hydroxide, EMD) to form the sol. The sol was then heated on a hot plate while stirring to evaporate the water from the solution and form the gel. Samples were then fired to 500° C at a heating rate of approximately 3° C/min and held at temperature for 10 hours in a quartz tube furnace under flowing nitrogen to calcine the sample. Up to 8 wt.% pyromellitic acid ($C_6H_2(CO_2H)_4$), Sigma Aldrich, abbreviated PA from this point forward) and, optionally, iron nitrate, ferrocene ($C_{10}H_{10}Fe$, Alfa Aesar, recrystallized), or ferrocenecarboxylic acid ($C_{11}H_{10}O_2Fe$, Aldrich, 97%, abbreviated FCA from this point forward), ranging from 0.001-1 wt.% were added to the samples, and mixtures were ground using a planetary ball mill in an appropriate solvent (ethanol or acetone) for one hour. The grinding solvent was then evaporated under a flow of nitrogen and the resulting powder was thoroughly mixed and fired to 600° C for ten hours.

Phase purity was determined by XRD on the resulting powders using a Philips X'Pert diffractometer using an X'Celerator detector with Cu Kα radiation (λ = 1.54 Å). Particle size distributions were resolved by means of a Beckman Coulter particle size analyzer (model LS 230) using Darvan*C (ammonium polymethacrylate, aqueous

solution, R.T. Vanderbilt Company Inc.) as a dispersant. Particle morphology studies were conducted using a field emission-scanning electron microscope (FE-SEM, Jeol JSM-6340F). Luvak Inc. (Boylston, MA) conducted the elemental analyses (carbon and hydrogen) of several samples.

An integrated confocal Raman microscope system, "Labram," made by ISA Group Horiba was used to analyze the structure of the active materials. Raman spectroscopy measurements were carried out at room temperature in ambient atmosphere using an internal He-Ne 632 nm laser was used as the excitation source. The power of the laser beam was adjusted to 0.1 mW with neutral filters of various optical densities. The size of the laser beam at the sample was ~1.2 μm, and the average acquisition time for each spectrum was 25 seconds. The resolution of this instrument is approximately 1.7 cm^{-1}. Baseline correction and deconvolution analysis of Raman spectra were performed with a commercial software package (PeakFit, version 4.05, SPSS Inc.).

Pressed pellets for conductivity studies were fabricated by uni-axially pressing ~0.5 g of active material to 10 kpsi in a ½" stainless steel die. The pellets were then transferred into balloon holders and cold isostatically pressed to 180 kpsi achieving a final density of ~70% of the theoretical $LiFePO_4$ density (3.6 g/cm^3). Thin gold electrodes were then sputtered on to each face of the pellet using a Bal-Tec SCD 050 sputter coater. AC impedance spectra were obtained using a Solartron Instruments 1260 impedance/ gain-phase analyzer at selected temperatures between 25 and 200° C. Conductivities were derived from the touchdown of the capacitative arc in the Nyquist plots.

Electrodes were composed of 80 wt.% active material, 8 wt.% Kynar poly (vinylidene fluoride) (PVDF) (Elf Atochem North America Inc., Technical Polymers Department), 6 wt.% SFG-6 synthetic flake graphite (Timcal Ltd., Graphites and Technologies), and 6 wt.% acetylene black. Electrodes were cast as a slurry in 1-methyl-2-pyrrolidinone (Sigma Aldrich, 99%) onto aluminum current collectors and dried for 24 hours in air followed by 12-24 hours in a vacuum oven at 120 °C. Electrodes with

an area of 1.8 cm^2 were punched from the cast electrode and typically had loadings of about 1 mAh/cm^2. Assembly of lithium half-cells in 2032 coin cells was performed in a helium filled glove box using 1 M $LiPF_6$ in 1:2 ethylene carbonate/dimethylcarbonate (EC/DMC) electrolyte solution and a Celgard 3401 separator. At least two cells of the same type were tested for each material to ensure reproducibility. Electrochemical studies were undertaken galvanostatically using an Arbin BT/HSP-2043 and/or a Macpile II (Bio-Logic, S.A., Claix, France) automated cycling data recorder between 2.0 and 3.9 V at room temperature. Cells were always charged at a current density corresponding to C/25 and allowed to rest 15 minutes between half-cycles.

6.4 Results and Discussion

All powders were determined to be phase-pure by XRD analysis. The primary particle sizes found in the powders of all samples were highly variable, ranging from <100 nm to more than 1 μm. Agglomerates were larger than 2 μm in all cases, with large, bimodal size distributions observed in both the particle size and SEM studies. Individual particle morphologies varied widely as well, ranging from large smooth platelets to highly porous particles, which formed due to gas evolution during synthesis (Figure 6.1).

Our previous work[21] showed that some organic or polymeric precursors used to produce carbon coatings did not decompose completely at the low synthesis temperatures used to make $LiFePO_4$. Residual hydrogen and functional groups on carbon lower the electronic conductivity, resulting in electrode materials with poor electrochemical performance. Of the additives examined in reference 18, PA (pyromellitic acid or 1, 2, 4, 5-benzenetetracarboxylic acid) gave the best results, as it was found to decompose readily resulting in a high quality carbon coating. To examine the effect of varying the amount of PA on the carbon amount and structure in the final product, several samples were prepared for the current study. There is usually a small amount of residual (*in situ*) carbon even in materials prepared without additives, due to the decomposition of organic moieties in the

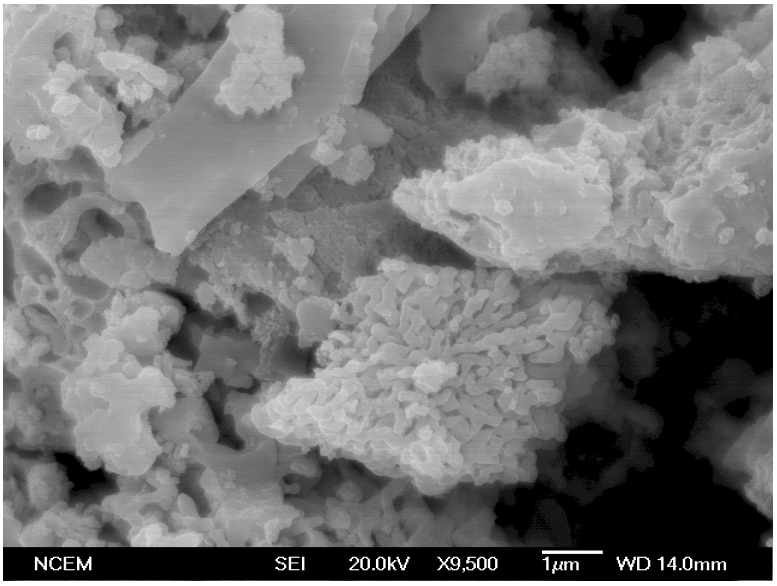

Figure 6.1: Scanning electron micrograph of a typical $LiFePO_4$/C composite.

reactants. This amount varies with processing temperature and other variables, and was 0.3 wt.% under the conditions used here. The addition of PA during synthesis results in a modest increase in the carbon content (Table 6.1) and a general decrease in the H/C ratio with some sample variation, close to that of PA itself (0.05). The latter indicates the degree of decomposition of the organic components in the synthesis mixture, and suggests that better quality carbons are produced from the additive, due, in part, to its lower hydrogen content. Also included in Table 6.1 are carbon structural parameters determined from analysis of the Raman spectra obtained on the various $LiFePO_4$ samples.

Raman spectroscopy is a particularly useful tool for characterizing the near-surface structure (i.e. disorder and crystallite formation) of carbon films because carbon is a relatively strong scatterer with two E_{2g} modes predicted to be Raman active. Figure 6.2 shows a typical Raman spectrum of a $LiFePO_4$ powder from this study. A sharp band at 953 cm^{-1} corresponds to the symmetric A_g mode (ν_1), whereas the two weaker bands at 997 and 1098 cm^{-1} are attributed to the asymmetric stretching modes (ν_3) of the $(PO_4)^{3-}$ anion.[22]

Table 6.1: Carbon contents, H/C ratios, D/G and sp^2/sp^3 ratios for selected $LiFePO_4$ samples processed with pyromellitic acid (PA), with or without graphitization catalysts as noted.

Wt.% PA	Catalyst	Wt.% C	H/C	Average D/G (S.D.)[a]	sp^2/sp^3 (S.D.)[a]
0	—	0.304	0.079	1.26 (0.013)	0.091 (0.0298)
2	—	0.423	0.048	1.19 (0.029)	0.120 (0.01)
4	—	0.714	0.045	1.12 (0.005)	0.257 (0.004)
6	—	0.764	0.054	1.10 (0.059)	0.271 (0.061)
8	—	0.843	0.037	1.11 (0.243)	0.243 (0.016)
6	0.001 wt.% $Fe(NO_3)_3$	0.711	0.056	1.11 (0.018)	0.319 (0.011)
6	0.01 wt.% $Fe(NO_3)_3$	0.594	0.056	1.06 (0.052)	0.309 (0.091)
0	1 wt.% Ferrocene	0.551	0.039	1.98 (0.056)	0.007 (0.005)
6	1 wt.% Ferrocene	1.45	0.044	1.09 (0.040)	0.183 (0.053)
6	1 wt.% FCA[b]	1.56	0.028	1.11 (0.009)	0.204 (0.009)

a) S.D.= Standard deviation. Values are relative measures obtained from analysis of Raman spectra. See text for explanation of how these were obtained.
b) FCA= Ferrocenecarboxylic acid.

Two intense broad bands located at ~1350 and 1593 cm^{-1} are assigned to the D and G bands of the residual carbon, respectively. The relative peak heights and widths of carbon bands change substantially with the pyrolysis temperature and the nature of the precursor materials. The variation of the width and intensity of the D and G bands is related to the growth and size of different carbon phases, the presence of functional groups and impurities. While most authors agree that the peak at 1590 cm^{-1} is the first order scattering from the in-plane E_{2g} mode, there are notable discrepancies in the frequency of this peak reported in the literature, depending on the type of carbon and preparation method. The G band tends to broaden and shift toward higher frequencies with decreasing intraplanar (La) and interplanar (Lc) microcrystallite dimensions. This effect has been also explained in terms of the superposition of the G band and a new D band at ~1620 cm^{-1}, which

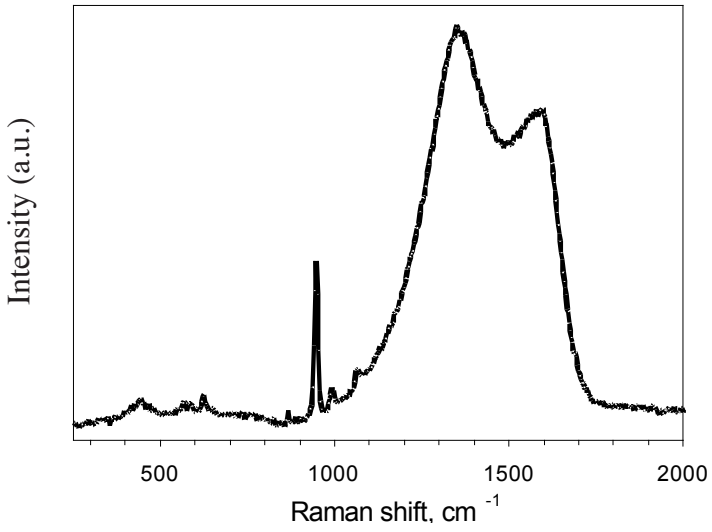

Figure 6.2: A typical Raman spectrum of a $LiFePO_4$/C composite powder.

originates from sp^2 carbon vibrations. When *La* and *Lc* decrease, a new feature at 1360 cm^{-1}, the D band, is usually observed. The origin of this band has been the subject of many controversies. It is usually assigned to the A_{1g} mode that is associated with the breakage of symmetry occurring at the edges of graphite sheets.[23, 24]

To resolve the Raman spectra of the residual carbon in the $LiFePO_4$ samples, we applied a standard peak deconvolution procedure after a polynomial background subtraction. A deconvolution of the Raman spectrum of all of the $LiFePO_4$ samples using a fit with two carbon D and G lines did not give accurate results. Four Gaussian bands were necessary to account for the observed Raman features with minimum error. Those bands are situated at ~1190, 1350, 1518 and 1590 cm^{-1}. The bands at ~1518 cm^{-1} and 1190 cm^{-1} have uncertain origins but they have already been observed in disordered carbon black and diamond like carbons.[25, 26] That could imply that short-range vibrations of sp^3 coordinated carbons contribute to the disordered spectra. As a matter of fact, carbons produced at ~700° C usually contain a significant amount of disorganized or, in other words, truly amorphous phase. Coordination of carbon atoms in this short-order phase is highly

random and varies from sp^2 and sp^3 but there are no long-order graphite- and diamond-like domains in it. Numerous HRTEM studies of carbon blacks reveal that the bulk of carbon black particles consist of a completely disorganized carbon structure whereas small (10-40 Å) graphene domains are arranged at the surface. The ratio between the "disorganized" poorly conductive phase and graphite-like phase in carbon blacks is very dependent on the pyrolysis temperature and the type of organic precursor. It is the main reason why Raman spectra of "amorphous carbons" cannot be fit with two Gaussian bands. It is also reflected by the strong temperature dependence of electronic conductivity of pyrolyzed carbon blacks. The appearance of strong sp^2 related Raman modes, and the absence of a sharp characteristic 1330 cm^{-1} diamond Raman peak in the visible Raman spectra lead to the suggestion that these pyrolyzed carbons are amorphous with a predominant sp^2 fraction.[27] However, other studies substantiated that diamond-like and/or amorphous carbons can contain a significant fraction of sp^3 bonds while the sp^2 component might be very small.[28] Raman spectroscopy is mainly sensitive to the configuration of sp^2 sites because of their higher cross section. A multi-wavelength analysis is always recommended to give reliable qualitative information about sp^2/sp^3-coordinated carbon ratios.

The D/G (disordered/graphene) and sp^2/sp^3 ratios determined in this study by the analysis of the Raman spectra (Table 6.1) do not yield the actual ratios but rather values that are correlated to these structural parameters. Thus, they are useful for comparing samples to each other but not as quantitative measures of the graphene or sp^3 contents. Based on this analysis, the data in Table 6.1 show that D/G ratios decrease and sp^2/sp^3 ratios increase as more PA is added, up to about 6 wt.%. Thus, the structure of carbon produced when PA is present during calcination is markedly different from that produced from the precursors alone.

Pressed pellet conductivities as a function of temperature were obtained for several of these materials (Figure 6.3). The room temperature conductivity of ~10^{-8} S/cm

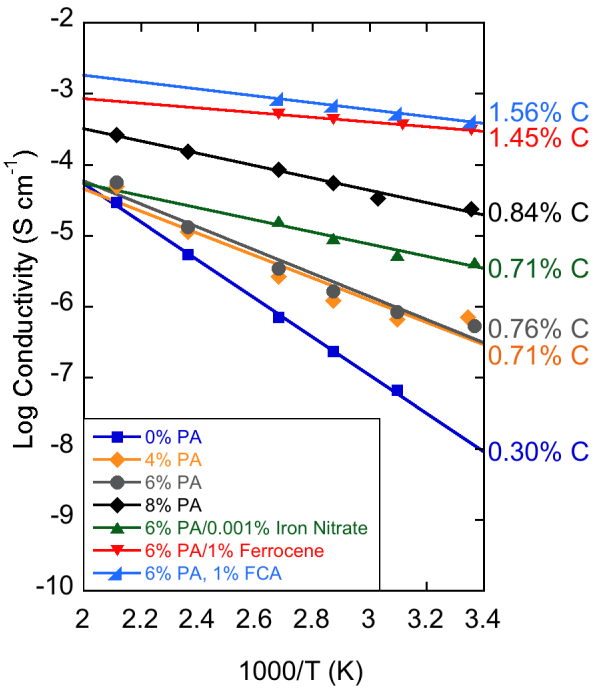

Figure 6.3: Pressed pellet conductivities as a function of temperature for several of the $LiFePO_4$/C materials prepared for this study.

extrapolated from the Arrhenius fit for the $LiFePO_4$ powder produced without PA agrees well with data previously obtained on pure $LiFePO_4$ powders,[7] despite the presence of 0.3 wt.% residual carbon from the reaction precursors. Samples prepared with 4 or 6 wt.% PA have room temperature conductivities nearly two orders of magnitude higher, although the carbon contents are increased to only about 0.7 wt.%. Further improvements are observed when 8 wt.% PA is used.

Figure 6.4 shows the capacities obtained at several discharge rates for lithium cells containing materials processed with PA and the corresponding D/G ratios. The carbon structural parameters and pressed pellet conductivities correlate well with electrochemical performance. The structure of the carbon affects the conductivity of the composite material, which also influences the rate behavior in electrochemical cells. Thus, the latter tends to track the former. The differences seen in the conductivities and electrochemical

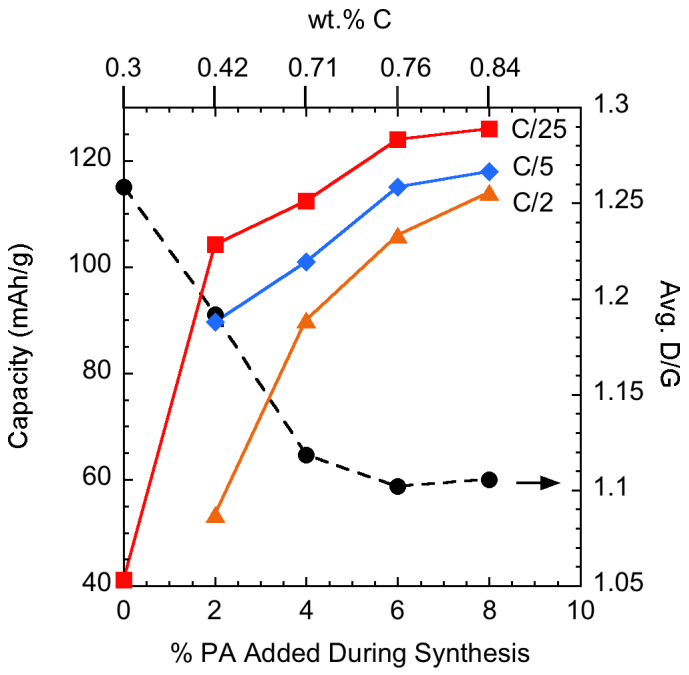

Figure 6.4: Specific capacities obtained at various discharge rates for lithium cells containing $LiFePO_4$ samples prepared with and without PA (left axis), and D/G ratios as determined by Raman microprobe spectroscopy for the same samples (right axis).

characteristics of the samples prepared with larger amounts of PA primarily shows the influence of increasing the carbon amount, as the carbon structure does not vary significantly. It is, however, interesting to note that materials previously described in reference 18, having similar carbon contents and particle morphologies, perform worse than those presented in Figure 6.4. For example, compare sample 7SG, prepared without additives, and containing 0.7 wt.% carbon, to that of the material processed with 6 wt.% PA having 0.76 wt.% carbon in the current work. The former delivers less than 100 mAh/g at C/25 while the latter gives 120 mAh/g.

While the improvement in carbon structure, pressed pellet conductivities and electrochemical performance seen in samples prepared with PA is striking, rate limitations are still evident. Improvements in the carbon structure and/or increases in the carbon content are still necessary for optimum performance.

There is considerable precedence in the carbon literature for the use of transition metal-containing compounds as low temperature (500-1000° C) catalysts for the production of graphitic carbon structures. In particular, iron nitrate,[29] ferrocene,[30, 31] and ferrocene derivatives[32] have been used extensively under conditions very similar to those used for the synthesis of $LiFePO_4$. In the case of iron nitrate catalysts, progressively more reduced iron oxides are formed during heating in a hydrocarbon rich, oxygen-controlled environment.[29] This process eventually leads to the formation of iron carbide, which acts as a nucleation site for graphite. Furthermore, the role of iron oxides in the graphitization process may explain the variability of the carbon produced in the sol-gel samples made without additives in references 20 and 21, as these are common impurities in $LiFePO_4$ preparations.

Samples calcined with small amounts of iron nitrate (0.001-0.01 wt.%) and PA gave powders with carbon contents below 1 wt.%, similar to those calcined with PA alone (Table 6.1). While the D/G ratios are not significantly changed from those of samples processed with similar amounts of PA, sp^2/sp^3 ratios are higher. This suggests that, while the graphene domain sizes are not changed from materials prepared with PA only, there is a greater proportion of carbon with a graphitic nature. It is possible to assess the effect of the increased sp^2 character on the electronic conductivity by comparing the results for two composites with identical carbon contents (0.71 wt.%), one processed with iron nitrate, and one without, in Figure 6.3. The former gives better electrochemical performance than the latter (Figure 6.5). The higher discharge capacities at given rates can be attributed to the increased composite conductivity (~10^{-5} S/cm at room temperature) due to the higher sp^2/sp^3 ratio. The conductivity of this sample exceeds that of all non-catalyst treated samples except the one made with 8 wt.% PA, which contains more carbon. Note also that the effect of a higher sp^2/sp^3 ratio can compensate for a lower carbon content in terms of electrochemical performance; in Figure 6.5, a $LiFePO_4$ material containing only 0.59 wt.% carbon (processed with both PA and iron nitrate) is superior to the one containing

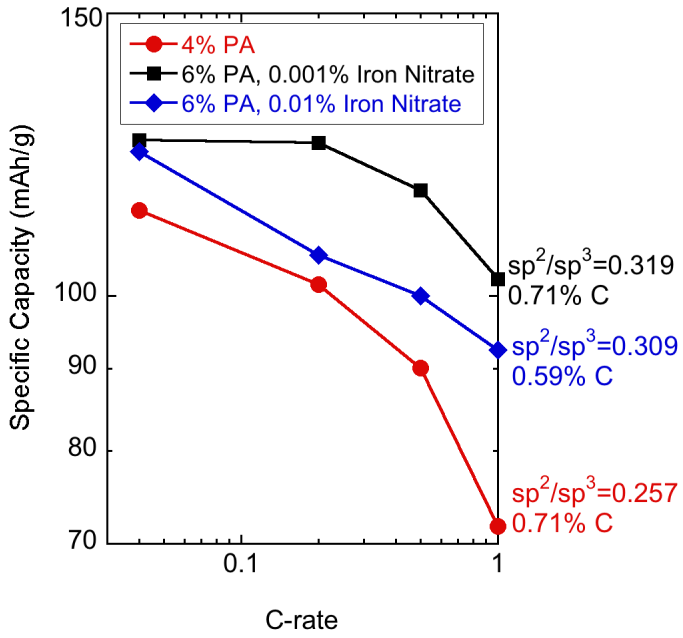

Figure 6.5: Specific capacities as a function of discharge rate for lithium cells containing three different samples of $LiFePO_4$, one processed with 4 wt.% PA alone, one with 0.001 wt.% iron nitrate and 6 wt.% PA, and one with 8 wt.% PA and 0.01 wt.% iron nitrate.

0.71 wt.% carbon, (processed with only PA) which has a lower sp^2/sp^3 ratio.

$LiFePO_4$ processed with PA and higher concentrations of iron nitrate performed worse than the materials made with 0.01 wt.% iron nitrate or less listed in Table 6.1. For graphitization to occur, iron nitrate (or the oxides that form from thermal decomposition) must be located in carbon-rich areas on the surfaces of the powders. Excessive iron nitrate results in an overabundance of resistive iron oxide, which adversely affects the electrochemical performance. Conversely, carbon-rich areas not in contact with the catalyst will not graphitize at the relatively low temperatures used to synthesis $LiFePO_4$. A low concentration of iron nitrate is preferable to prevent excessive formation of iron oxide, but it must be dispersed homogeneously with the carbon source for ideal results. For some materials processed with PA and iron nitrate, considerable spot-to-spot variation in the Raman spectra were observed, indicating that the quality of the carbon was not uniform throughout the powder. Consequently, these materials did not show any appreciable

improvement in the electrochemical performance and are not further considered here.

Ferrocene and its derivatives have advantages over iron nitrate as they contain both catalyst centers and carbon sources within the same molecules, ensuring close contact between the two entities. They have been used extensively in the synthesis of nano-structured carbon materials,[30-32] and as soot control agents for cleaner burning fuels.[33] A composite prepared with 1 wt.% ferrocene, however, has a low carbon content (Table 6.1), only slightly higher than that of $LiFePO_4$ prepared without any additives. Ferrocene sublimes at about 175°C,[34] so much of it is lost during calcination under the conditions used here. The quality of carbon is poor, judging from the structural factors listed in Table 6.1, although its thorough decomposition is evidenced by a low H/C ratio. In contrast, $LiFePO_4$ prepared with either ferrocene or FCA as well as PA has significantly higher carbon contents than materials prepared with the same amount of PA alone (Table 6.1), although the final amount is still less than 2 wt.%. This suggests an interaction between the ferrocene and PA occurs upon heating, which results in improved retention of elemental carbon. The H/C ratios of these composites are lower than that of the starting materials, ferrocene (0.08) and FCA (0.075) themselves, indicating nearly complete thermal decomposition. The carbon structural factors, as determined by Raman spectroscopy, are similar to that of composites made with PA alone, although the sp^2/sp^3 ratios are less than that of the materials processed with iron nitrate. Thus, the several orders of magnitude increase in conductivity of a ferrocene/PA-treated $LiFePO_4$ pressed pellet compared to the others in Figure 6.3, is mainly attributable to the increase in carbon content, rather than to any improvements in carbon structure over composites made with PA alone.

Additional peaks at low wave numbers were observed in the Raman spectra of several samples processed with ferrocene and PA (Figure 6.6), some of which match those reported for Fe_3C.[35-37] A similar Raman spectrum is observed for the thermal decomposition products of ferrocene alone in a sealed tube, under conditions much like those used to

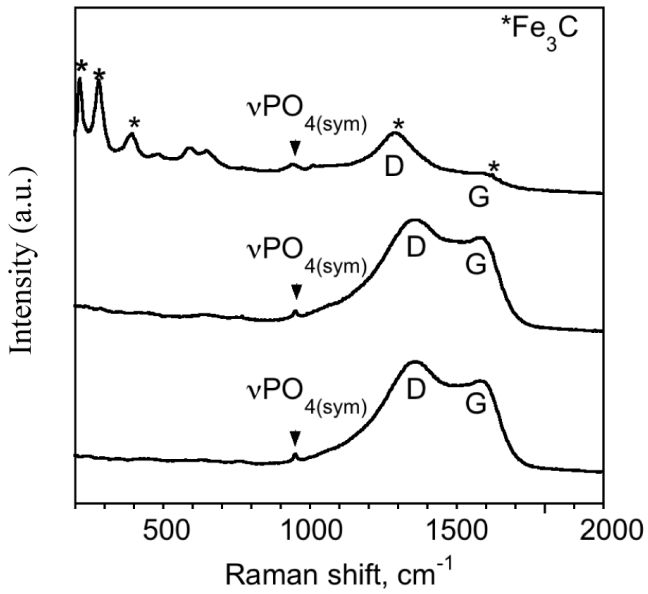

Figure 6.6: Raman spectra taken on several spots of a $LiFePO_4$ powder processed with 0.5 wt.% ferrocene and 6 wt.% PA (this sample is not included in Table 6.1). The top and bottom spectrum show the normal peaks attributable to $LiFePO_4$ and carbon (see text). In the middle spectrum, peaks from iron carbide overlap the D-band of carbon. Iron carbide and carbon nanotube peaks also appear at low wavenumbers.

produce $LiFePO_4$ in this study. In addition to Fe_3C and other forms of carbon, numerous carbon nanotubes with diameters of about 5 nm were observed in the transmission electron micrographs of the ferrocene thermal decomposition products.[38] Ferrocene is commonly used as a catalyst precursor for the production of either single-walled[33] or multi-walled[39, 40] carbon nanotubes at moderate temperatures. Deposition of nanotubes (and the related process of metal dusting corrosion) takes place via the intermediate Fe_3C,[41] which is formed as carbon diffuses through the metal nanoparticles formed during decomposition.

The presence of Fe_3C and, possibly, carbon nanotubes in some of the ferrocene/PA-treated $LiFePO_4$ composites complicates the interpretation of the Raman spectra, as some of the peaks overlap with the D and G bands of carbon itself. Additionally, Fe_3C is metallic and even small amounts can be expected to influence the pressed pellet conductivities. For these reasons, these samples have been omitted from the present discussion, although they will be the subjects of a future publication.

Figure 6.7 shows the specific capacity as a function of current density for lithium cells containing $LiFePO_4$ samples treated with ferrocene or FCA and PA. Results for a cell containing material treated with ferrocene alone and another with PA alone are also included, for comparison. The best high rate behavior seen in this study was obtained for cells containing $LiFePO_4$ processed with 1 wt.% ferrocene and 6 wt.% PA, in accordance with the high pressed pellet conductivities seen in Figure 6.3. Because the structural characteristics of the carbon do not vary much for these samples (with the exception of the poorly performing material treated with ferrocene alone), the differences in the electrochemical performance shown in Figure 6.7 can be attributed mainly to the changes in carbon content. The material containing 1.56 wt.% carbon (processed with FCA and PA), however, performs somewhat worse at C-rate than the one treated with ferrocene and PA, which has a marginally lower carbon content of 1.45 wt.% and slightly lower pressed pellet conductivities. As with some of the materials calcined with iron nitrate, considerable spot-to-spot variation was seen in the Raman spectra of the FCA-treated material, indicating non-homogeneity of the carbon coating. (The structural factors in Table 6.1 derived from these spectra are averages taken from 10 spectra.) The non-homogeneity is less likely to have an impact on pressed pellet conductivities, in which a percolation threshold is easier to achieve, than in a porous composite electrode containing the same material, used to obtain the electrochemical data. In contrast, much better homogeneity in the Raman spectra was observed for materials processed with ferrocene. FCA does not sublime like ferrocene does, but undergoes a two-step thermal decomposition at 250°C and 410°C.[32] The volatility of ferrocene may be beneficial in that it promotes a more even distribution of carbon compared to FCA. A recent transmission electron microscopy study of $LiFePO_4$ treated with 6 wt.% PA and 1 wt.% ferrocene showed that carbon is located on all the surfaces of primary particles, even those fused into agglomerates like those shown in Figure 6.1.[3]

The results presented here show that the composite conductivity, and therefore,

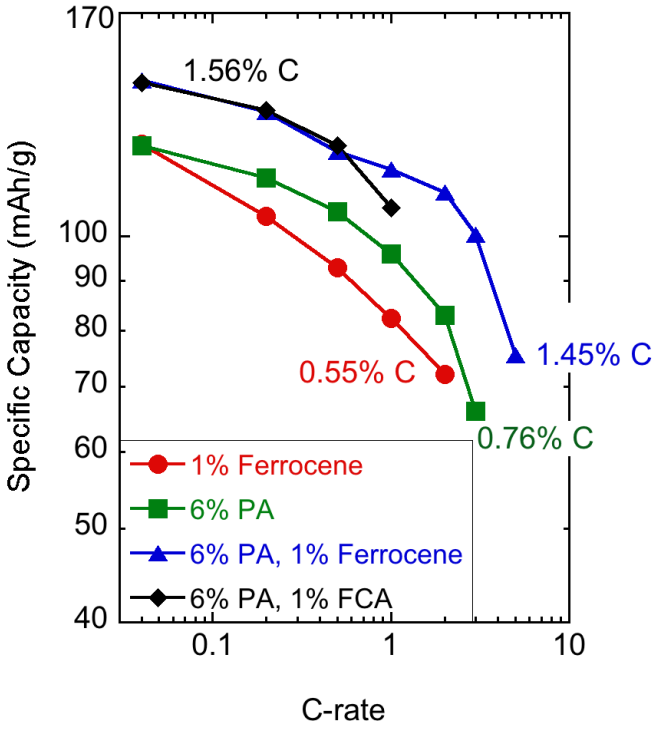

Figure 6.7: Specific capacities as a function of discharge rate for lithium cells containing $LiFePO_4$ samples processed with ferrocene or FCA, with or without PA, as noted.

the electrochemical performance, is related to the amount, structure, and distribution of the carbon in the coatings on the $LiFePO_4$ particles. In some cases, composites containing less carbon are more conductive than those with more, due to a higher sp^2 character. This translates directly into improved electrochemical performance. The best results in this study, however, were obtained for composites with carbon contents above 1 wt.%. This may be due, in part, to the fact that it is easier to obtain complete coverage over particle surfaces when more carbon is present. Provided that a relatively homogeneous coating can be produced by, for example, better mixing prior to calcination, what is the lowest carbon content needed to produce a high-rate $LiFePO_4$? How much improvement in the carbon structure is necessary to allow a substantial decrease in the content? The pressed pellet conductivity data, although fairly limited, offers some insights into these questions. In Figure 6.8, the logs of the room temperature pressed pellet conductivities of three

samples with similar carbon contents (~0.7 wt.%) are plotted vs. the sp^2/sp^3 ratios. D/G and H/C ratios of the carbons in these composites are fairly similar, so that the data mainly show the effect of increasing the sp^2 character. Data for two other materials with higher carbon contents (~1.5 wt.%) are also plotted; these points fall on a line roughly parallel to the low-carbon sample line. Presumably, conductivity data for samples with intermediate carbon contents would fall on other parallels between these two lines, provided that the details of coverage were similar and the other structural characteristics of the carbons were not significantly different than for these two sets of samples. The dotted tie lines show that an sp^2/sp^3 ratio close to 0.45 (i.e., requiring more than double the sp^2 character) is needed for ~0.7 wt.% C carbon composites to achieve conductivities (and, by inference, electrochemical performances) similar to that of $LiFePO_4$ composites with ~1.5 wt.% carbon in them.

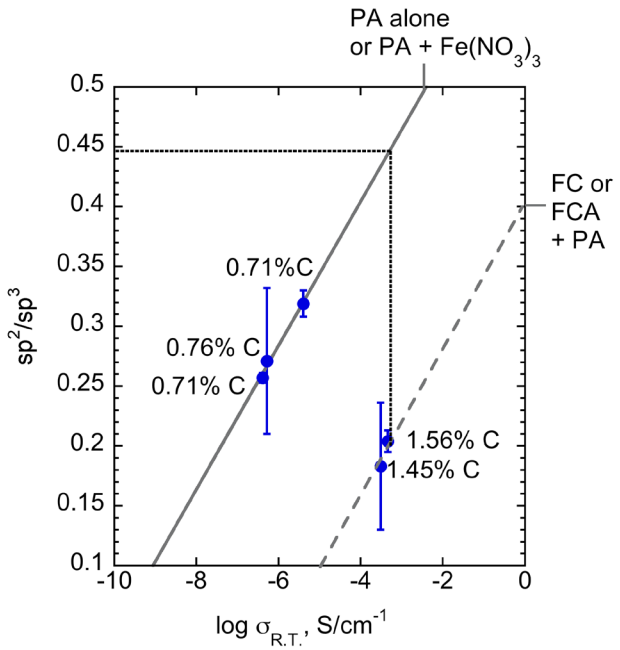

Figure 6.8: Pressed pellet conductivities as a function of sp^2/sp^3 ratio for two different sets of composite $LiFePO_4$ samples having similar carbon contents. The solid gray line shows a linear fit to the data for composites with 0.71-0.76 wt.% carbon. The dashed gray line parallels this fit and connects the data for composites with higher carbon contents. Dotted black lines show the improvement needed in sp^2/sp^3 ratio in the low carbon samples to achieve conductivities similar to those found in the high carbon samples. FC=ferrocene and other abbreviations are as explained in the text.

An alternative approach is presented in Figure 6.9. Here, $LiFePO_4$/C composite conductivities are calculated using an equation derived from the simple bricklayer model described by Maier.[42] In this model, mono-sized cubic grains of the major phase having a bulk conductivity, σ_{bulk}, are considered to be uniformly surrounded by a secondary grain boundary phase with conductivities defined in the parallel ($\sigma_{gb}^{\parallel}$) and perpendicular ($\sigma_{gb}^{\perp}$) directions. For a situation where the secondary phase is more conductive than the bulk and the thickness of the grain boundary (δ_{gb}) is much smaller than that of grains in the bulk (d_{grain}), $\sigma_{gb}^{\perp}$ can be ignored, and the measured composite conductivity (σ_m) is given by Equation 6.1.[43] For $\sigma_{bulk} = 10^{-9}$ S/cm, the curves shown in Figure 6.9, showing the effect of varying the grain boundary conductivity and thickness of the carbon layer, are produced. An 'x' marks the estimated grain boundary conductivity of about 0.1 S/cm for the $LiFePO_4$ sample processed with 1 wt.% ferrocene and 6 wt.% PA (1.45 wt.% C), using the room temperature

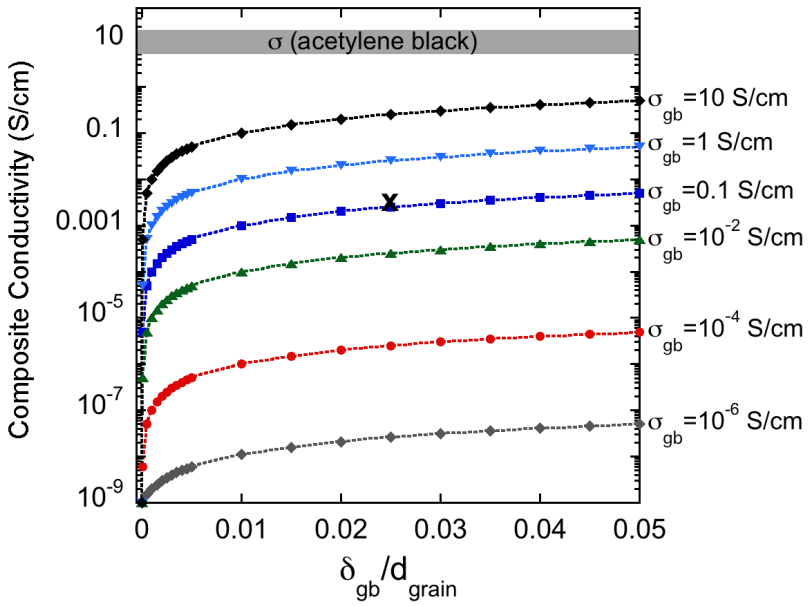

Figure 6.9: Relationship between composite conductivities and volume fraction of carbon for given coating conductivities, calculated using the bricklayer model, as described in the text. The bulk conductivity of $LiFePO_4$ was taken as 10^{-9} S/cm for the calculations. The point marked with an 'x' indicates the estimated composite conductivity for a sample processed with 6 wt.% PA and 1 wt.% ferrocene, containing 1.45 wt.% carbon, based on data from Figure 6.3 and reference 3.

$$\sigma_m = (1 + \frac{\sigma_{gb}^{\parallel}}{\sigma_{bulk}} \frac{\delta_{gb}}{d_{grain}})\sigma_{bulk} \qquad \text{Eq. 6.1}$$

composite conductivity data from Figure 6.3 and estimating an average δ_{gb} of 5 nm and grain size, d_{grain}, of 200 nm from the TEM results.[3]

The samples in this study deviate markedly from the ideal of mono-sized grains evenly coated with a secondary phase, necessitating considerable caution[44] when attempting to determine the carbon coating conductivities using this model. Still, a careful examination of the composite conductivity behavior as a function of carbon coating thickness in an ideal system is instructive for the purpose of designing high-rate $LiFePO_4$ electrodes. It is clear that increasing the carbon amount (or decreasing the grain size) has the greatest effect on composite conductivities at low values of δ_{gb}/d_{grain}, and improves most dramatically when $\sigma_{gb}^{\parallel}/\sigma_{bulk} > 10^3$. Increasing the coating thickness past a certain point results in rapidly diminishing returns, especially if it is poorly conducting. It is much more effective to improve the grain boundary conductivity instead. The strategies employed in this study may be used to achieve this goal.

6.5 Conclusions

Several synthetic additives were used to improve the carbon coatings on $LiFePO_4$ electrode materials. PA added prior to calcination decreases the D/G ratios of the carbon produced *in situ*, while the use of both iron nitrate and PA results in increased sp^2 character without further improving D/G ratios. Thus, a greater fraction of the carbon has graphitic character although domain sizes are not increased. The production of more graphitic carbon coatings results in higher pressed pellet conductivities of the $LiFePO_4$/C composites and improved electrochemical performance of cells containing these materials, although the carbon content is not necessarily increased. The combination of both ferrocene and PA used during $LiFePO_4$ synthesis causes more carbon to be retained, although the structural

characteristics are similar to that produced from the same amount of PA alone.

6.6 Acknowledgments

This work was supported by the Assistant Secretary for Energy Efficiency and Renewable Energy, Office of FreedomCAR and Vehicle Technologies of the U.S. Department of Energy under contract no. DE-AC02-05CH11231. The authors would also like to thank Heike Gabrisch (University of New Orleans) for her assistance with the TEM characterization of the powders as well as Robert Kostecki and Marek Marcinek (Lawrence Berkeley National Laboratory) for the Raman analysis of the carbon coatings and their useful discussions on the diagnostics of carbon films.

6.7 References

1. Doeff, M.M., et al., *Optimization of carbon coatings on LiFePO(4).* Journal of Power Sources, 2006. 163(1): p. 180-184.

2. Gabrisch, H., J. Wilcox, and M.M. Doeff, *TEM Studies of Carbon Coated LiFePO(4) After Charge Discharge Cycling.* ECS Transactions, 2007. 3(36): p. 29-36.

3. Gabrisch, H., J.D. Wilcox, and M.M. Doeff, *Carbon Surface Layers on a High-Rate LiFePO(4).* Electrochemical and Solid-State Letters, 2006. 9(7): p. A360-A363.

4. Wilcox, J.D., et al., *Factors Influencing the Quality of Carbon Coatings on LiFePO(4).* Journal of The Electrochemical Society, 2007. 154(5): p. A389-A395.

5. Padhi, A.K., K.S. Nanjundaswamy, and J.B. Goodenough, *Phospho-olivines as Positive-Electrode Materials for Rechargeable Lithium Batteries.* Journal of the Electrochemical Society, 1997. 144(4): p. 1188-1194.

6. Andersson, A.S., et al., *Lithium extraction/insertion in LiFePO(4): an X-ray diffraction and M˜ssbauer spectroscopy study.* Solid State Ionics, 2000. 130(1-2): p. 41-52.

7. Shi, S., et al., *Enhancement of electronic conductivity of LiFePO(4) by Cr doping and its identification by first-principles calculations.* Physical Review B, 2003. 68(19): p. 195108.

8. Croce, F., et al., *A Novel Concept for the Synthesis of an Improved LiFePO(4) Lithium Battery Cathode.* Electrochemical and Solid-State Letters, 2002. 5(3): p. A47-A50.

9. Yamada, A., S.C. Chung, and K. Hinokuma, *Optimized LiFePO(4) for lithium battery cathodes.* Journal of the Electrochemical Society, 2001. 148(3): p. A224-A229.

10. Takahashi, M., et al., *Characterization of LiFePO(4) as the cathode material for rechargeable lithium batteries.* Journal of Power Sources, 2001. 97-98: p. 508-511.

11. Prosini, P.P., et al., *A New Synthetic Route for Preparing LiFePO(4) with Enhanced Electrochemical Performance.* Journal of the Electrochemical Society, 2002. 149(7): p. A886-A890.

12. Dominko, R., et al., *Impact of LiFePO(4)/C Composites Porosity on Their Electrochemical Performance.* Journal of the Electrochemical Society, 2005. 152(5): p. A858-A863.

13. Chung, S.-Y., J.T. Bloking, and Y.-M. Chiang, *Electronically conductive phospho-olivines as lithium storage electrodes.* Nat Mater, 2002. 1(2): p. 123-128.

14. Herle, P.S., et al., *Nano-network electronic conduction in iron and nickel olivine phosphates.* Nat Mater, 2004. 3(3): p. 147-152.

15. Wurm, C., et al., *World Patent, CNRS-UMICORE*. 2002.

16. Ravet, N., et al., *Electroactivity of natural and synthetic triphylite.* Journal of Power Sources, 2001. 97-98: p. 503-507.

17. Huang, H., S.C. Yin, and L.F. Nazar, *Approaching Theoretical Capacity of LiFePO(4) at Room Temperature at High Rates.* Electrochemical and Solid-State Letters, 2001. 4(10): p. A170-A172.

18. Bewlay, S.L., et al., *Conductivity improvements to spray-produced LiFePO(4) by addition of a carbon source.* Materials Letters, 2004. 58(11): p. 1788-1791.

19. Chen, Z. and J.R. Dahn, *Reducing Carbon in LiFePO(4)/C Composite Electrodes to Maximize Specific Energy, Volumetric Energy, and Tap Density.* Journal of the Electrochemical Society, 2002. 149(9): p. A1184-A1189.

20. Doeff, M.M., et al., *Effect of Surface Carbon Structure on the Electrochemical Performance of LiFePO(4).* Electrochemical and Solid-State Letters, 2003. 6(10): p. A207-A209.

21. Hu, Y., et al., *Electrochemical Performance of Sol-Gel Synthesized LiFePO(4) in Lithium Batteries.* Journal of the Electrochemical Society, 2004. 151(8): p. A1279-A1285.

22. Burba, C.M. and R. Frech, *Raman and FTIR Spectroscopic Study of Li(x)FePO(4) (0<x<1).* Journal of the Electrochemical Society, 2004. 151(7): p. A1032-A1038.

23. Matthews, M.J., et al., *Origin of dispersive effects of the Raman D band in carbon materials.* Physical Review B, 1999. 59(10): p. R6585.

24. Thomsen, C. and S. Reich, *Double Resonant Raman Scattering in Graphite.* Physical Review Letters, 2000. 85(24): p. 5214.

25. Rouzaud, J.N., A. Oberlin, and C. Beny-Bassez, *Carbon films: Structure and microtexture (optical and electron microscopy, Raman spectroscopy).* Thin Solid Films, 1983. 105(1): p. 75-96.

26. Bonhomme, F., J.C. Lassegues, and L. Servant, *Raman Spectroelectrochemistry of a Carbon Supercapacitor.* Journal of the Electrochemical Society, 2001. 148(11): p. E450-E458.

27. Salah, A.A., et al., *Reduction Fe(3+) of Impurities in LiFePO(4) from Pyrolysis of Organic Precursor Used for Carbon Deposition.* Journal of the Electrochemical Society, 2006. 153(9): p. A1692-A1701.

28. Casiraghi, C., A.C. Ferrari, and J. Robertson, *Raman spectroscopy of hydrogenated amorphous carbons.* Physical Review B (Condensed Matter and Materials Physics), 2005. 72(8): p. 085401-14.

29. Emmenegger, C., et al., *Synthesis of carbon nanotubes over Fe catalyst on aluminium and suggested growth mechanism.* Carbon, 2003. 41(3): p. 539-547.

30. Kuwana, K. and K. Saito, *Modeling CVD synthesis of carbon nanotubes: Nanoparticle formation from ferrocene.* Carbon, 2005. 43(10): p. 2088-2095.

31. Liu, S. and R.J. Wehmschulte, *A novel hybrid of carbon nanotubes/iron nanoparticles: iron-filled nodule-containing carbon nanotubes.* Carbon, 2005. 43(7): p. 1550-1555.

32. Keller, T.M. and S.B. Qadri, *Ferrocenylethynylbenzenes as Precursors to in Situ Synthesis of Carbon Nanotube and Fe Nanoparticle Compositions.* Chem. Mater., 2004. 16(6): p. 1091-1097.

33. Vander Wal, R.L. and L.J. Hall, *Ferrocene as a precursor reagent for metal-catalyzed carbon nanotubes: competing effects.* Combustion and Flame, 2002. 130(1-2): p. 27-36.

34. de Souza, A., A. Pires, and V. Soldi, *Thermal stability of ferrocene derivatives and ferrocene-containing polyamides.* Journal of Thermal Analysis and Calorimetry, 2002. 70(2): p. 405-414.

35. Lee, C.T., M.S. Odziemkowski, and D.W. Shoesmith, *An In Situ Raman-Electrochemical Investigation of Carbon Steel Corrosion in Na(2)CO(3)/ NaHCO(3), Na(2)SO(4), and NaCl Solutions.* Journal of the Electrochemical Society, 2006. 153(2): p. B33-B41.

36. Bi, X.-X., et al., *Nanocrystalline alpha-Fe, Fe(3)C, and Fe(7)C(3) produced via CO(2) laser pyrolysis.* J. Mater. Res., 1993. 8(7): p. 1666-1674.

37. Stanghellini, P.L., et al., *Vibrational frequencies associated with the carbide ligand in iron butterfly clusters.* Inorg. Chem., 1987. 26(18): p. 2950-2954.

38. Wilcox, J. and M. Doeff, *Unpublished results.*

39. Andrews, R., et al., *Continuous production of aligned carbon nanotubes: a step closer to commercial realization.* Chemical Physics Letters, 1999. 303(5-6): p. 467-474.

40. Lee, Y.T., et al., *Temperature-dependent growth of carbon nanotubes by pyrolysis of ferrocene and acetylene in the range between 700 and 1000 °C.* Chemical Physics Letters, 2003. 372(5-6): p. 853-859.

41. Zeng, Z. and K. Natesan, *Relationship between the growth of carbon nanofilaments and metal dusting corrosion.* Chem. Mater., 2005. 17(14): p. 3794-3801.

42. Maier, J., *Defect chemistry and ion transport in nanostructured materials: Part II. Aspects of nanoionics.* Solid State Ionics, 2003. 157(1-4): p. 327-334.

43. Guo, X. and Y. Ding, *Grain Boundary Space Charge Effect in Zirconia.* Journal of the Electrochemical Society, 2004. 151(1): p. J1-J7.

44. Fleig, J., *The influence of non-ideal microstructures on the analysis of grain boundary impedances.* Solid State Ionics, 2000. 131(1-2): p. 117-127.

7. Combustion Synthesis of Transition Metal Phosphates: A Novel Synthetic Approach

7.1 Abstract

Several preliminary experiments on the combustion synthesis of lithium transition metal phosphates are described. This is a new synthetic approach that results in the formation of a superior quality carbon coating on nanoparticle surfaces. Production of primary particles with nanoscale dimensions is key to the use of the transition metal olivines as cathode materials in high power cells. The potential for the co-synthesis of freestanding conductive carbon elements such as carbon nanotubes and fibers is also briefly addressed.

7.2 Introduction

The process of coating $LiFePO_4$, with a thin, highly conductive, coherent film of carbon is inherently difficult due to the limitations imposed by the thermal stability limits of $LiFePO_4$. In the presence of carbon, $LiFePO_4$ can be reduced to iron phosphide (Fe_2P) and/or iron phospocarbide (e.g. $Fe_{75}P_{15}C_{10}$) with the concurrent production of CO/CO_2. Experimentally, these reactions are observed to occur above 800° C in the $LiFePO_4$ system although other common impurity phases such as $Fe_2P_2O_7$ may be reduced at even lower temperatures.[1] The existence of interconnected nano-networks of these reduced species, as observed by electron energy loss spectroscopy (EELS), have been used to explain the anomalously high conductivities of doped $Li_{1-x}Zr_xFePO_4$ materials. The reduced species have conductivities (~10^{-1} S/cm) significantly higher than that of $LiFePO_4$ (~10^{-9} S/cm) and can dramatically increase the composite electronic conductivity.[1, 2]

The upper thermal limit of 800° C, or perhaps even lower depending on the sintering environment,[3] posses a significant barrier to the production of highly conductive carbon films. The pyrolytic production of graphitic carbons initiates at temperatures as

low as 600° C, at which point a distinctive band gap of approximately 300 meV begins to form.[4] At temperatures approaching 1300° C the valence and conduction band begin to overlap, resulting in a dramatically increased electronic conductivity.[4, 5] Conductivity in disordered materials such as carbon black, is significantly more complicated due to the presence of both crystalline and non-crystalline domains. The random nature of the non-crystalline domains, which may be composed of both sp^2 (graphite-like) and sp^3 (diamond-like) carbon centers, induces a localization of charge carriers that is highly dependent on the exact structure of the particle. However, as observed in graphitic carbons, increasing the heat treatment temperature leads to a strong decrease in electrical resistivity. This is largely attributed to the loss of volatile surface functional groups, and if processed correctly, the activation energy in such carbons can approach zero at temperatures as low as 1000° C.[4, 5]

Combustion based synthetic techniques are unique in that the initial heating event may be very intense and extremely rapid. These techniques rely on the exothermic reactions between metal salts and an organic fuel to produce high surface area powders.[6] Due to the rapid nature of the combustion event a homogeneous distribution of chemical components can be obtained. This can be a profound advantage over other synthetic methods such as precipitation when attempting to synthesize new materials containing components of varying chemical reactivities (see Chapters 3 and 4). The resulting powder can be crystalline or amorphous depending on the chemical composition and the fuel to oxidizer ratio, which determines the flame temperature.[7] Numerous organic fuels have been described in the literature, with glycine,[8] carbohydrazide,[9] citric acid,[10] and urea[6] being common. The choice of fuel is also important in achieving a homogeneous distribution of components as they often act as chelating agents for dissolved metal ions, inhibiting agglomeration during the initial dehydration process.[8]

The combustion synthesis of lithium transition metal phosphates offers the opportunity to produce active material powders with nanometer sized primary particles

in a quick and inexpensive fashion. Due to the extremely low intrinsic lithium diffusion coefficients of phosphate based cathode materials ($<10^{-13}$ cm^2/s),[11, 12] reduction of the diffusion distance is a key condition to be met in achieving optimal high-power performance.[13] Furthermore, the combustion technique offers a unique ability to create highly conductive carbon coatings on the surface of materials with low thermal stability limits. The carbon coating is primarily formed during the initial combustion process at temperatures that exceed the stability limit of the lithium transition metal phosphates against reduction. However, because the combustion reaction occurs very rapidly, these deleterious processes do not have time to occur. Subsequent heat treatment of the powder at a lower temperature allows for the formation of the desired crystal structure. The formation of a "high" temperature carbon film on a low temperature phase, such as $LiFePO_4$, allows for further minimization of carbon content, maximizing the available energy and power densities.

Additionally, combustion processes may be tuned to form freestanding carbon structures in addition to carbon coatings. These structures, such as fibers, sheets, and nanotubes, have long been explored as possible additives to battery electrode composites as a means of improving electronic conductivity with minimal amounts of carbon.[14-17] Issues such as cost and difficulties in dispersing the additives throughout the electrode matrix have presently precluded their use in commercial systems. A synthetic pathway based on the proper control of the combustion environment may allow for the co-synthesis of dispersed one dimensional carbon entities at the same time as small, carbon coated particles. Such an optimized material may require a minimum amount of conductive carbon added post synthesis, further improving the energy and power density.

7.3 Experimental Methods

To synthesize $LiFePO_4$ powders, stoichiometric mixtures of $LiNO_3$ (Mallinckrodt), $Fe(NO_3)_3 \cdot 9H_2O$ (98% EMD), and either $NH_4H_2PO_4$ (98+%, Sigma Aldrich) or H_3PO_4

(85%, EMD) were dissolved in a minimum volume of distilled water. Other olivine materials such as $LiCoPO_4$, $LiMnPO_4$, and $LiNiPO_4$ can be synthesized by substituting the proper metal nitrate. An organic fuel, either glycine (98.5+%, Sigma Aldrich) or citric acid (99.5+%, Alfa Aesar), was added to the solution and the pH was adjusted with HNO_3 (68-70%, BDH) to dissolve any precipitates. A variety of fuel to nitrate ratios were utilized throughout the study with common values being in the range of 0.5 to 1.5. Small (20 ml) batches of solution were condensed on a hot plate in a specially milled stainless steel combustion chamber until auto-ignition occurred. The resulting powders were collected, dispersed in acetone, and planetary ball milled for 1-2 hours. After removal of the acetone under flowing nitrogen the dried powders were heat treated at 500 to 600 °C for 2-4 hours (4° C/min ramp rate), depending on the sample, in a 4% H_2/N_2 gas stream.

Phase purity of the resulting powders was examined by X-ray diffraction (XRD) using a Philips X'Pert diffractometer with an X'Celerator detector using Cu Kα radiation (λ = 1.54 Å). Particle morphology studies were conducted on a field emission-scanning electron microscope (FESEM, Jeol JSM-6340F). Examination of the primary particles was accomplished via transmission electron microscopy (TEM) on a Phillips CM200FEG (field emission gun) at an accelerating voltage of 200 kV. To prepare samples for TEM, powders were ground in a mortar and pestle in acetone and transferred to a holey carbon grid. Luvak Inc. (Boylston, MA) conducted the elemental analyses (carbon and hydrogen).

An integrated confocal Raman microscope system, "Labram," made by ISA Group Horiba was used to analyze the structure of the active materials. Raman spectroscopy measurements were carried out at room temperature in ambient atmosphere using an internal He-Ne 632 nm laser as the excitation source. The power of the laser beam was adjusted to 0.1 mW with neutral filters of various optical densities. The size of the laser beam at the sample was ~1.2 μm, and the average acquisition time for each spectrum was 25 seconds. The resolution of this instrument is approximately 1.7 cm^{-1}.

Electrodes were composed of 80 wt% active material ($LiFePO_4$), 8 wt.% Kynar poly(vinylidene fluoride) (PVDF) (Elf Atochem North America Inc., Technical Polymers Department), 6 wt.% SFG-6 synthetic flake graphite (Timcal Ltd., Graphites and Technologies), and 6 wt.% acetylene black. Slurries prepared in 1-methyl-2-pyrrolidinone (Sigma Aldrich, 99%) were cast onto carbon coated aluminum current collectors (Intelicoat Technologies) by automated doctor blade. Electrodes were dried for 24 hours in air followed by 12-24 hours in a vacuum oven at 120° C. Cathodes with an area of 1.8 cm^2 were punched from the cast electrodes and typically had loadings of about 1 mAh/cm^2. Assembly of lithium half-cells in 2032 coin cells was performed in a helium filled glove box using 1 M $LiPF_6$ in 1:2 ethylene carbonate/dimethylcarbonate (EC/DMC) electrolyte solution and a Celgard 3401 separator. At least two cells of the same type were tested for each material to ensure reproducibility. Electrochemical studies were undertaken galvanostatically using an Arbin BT/HSP-2043 automated cycling data recorder between 2.0 and 3.9 V at room temperature. Cells were always charged at a current density corresponding to C/25 and allowed to rest 15 minutes between half-cycles.

7.4 Results and Discussion

Producing single phase, transition metal olivine powders via the combustion method requires great control over the experimental conditions. A typical XRD pattern is presented in Figure 7.1. No major second phase impurities can be detected and all peaks can be indexed in the *Pnmb* space group. TEM images of similarly produced $LiMnPO_4$ powders clearly show a primary particle size of approximately 30 nm (Figure 7.2), which agrees well with the particle size as estimated using the Scherrer equation (30 nm). Also evident is a continuous 2-3 nm thick amorphous carbon coating encapsulating the particle. In the case of $LiFePO_4$, particle agglomeration occurs after briefly firing to 600° C. The secondary particles range in size from 200-300 nm as clearly seen in the SEM micrograph of Figure 7.3. Depending on the experimental conditions, highly curved and branched

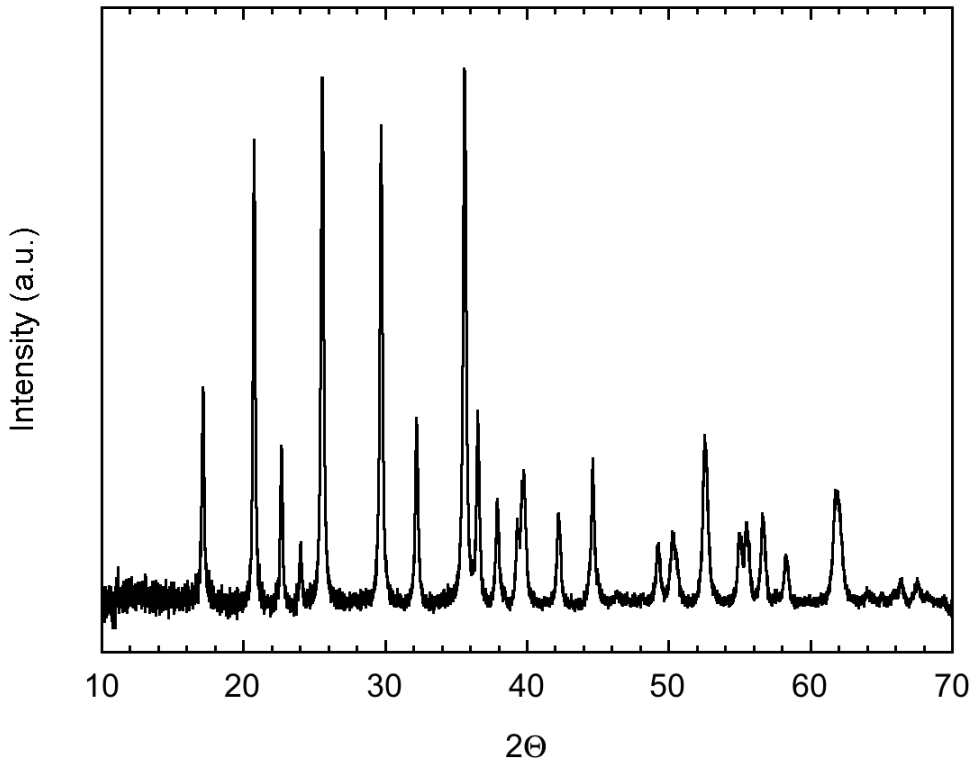

Figure 7.1: Powder XRD pattern of $LiFePO_4$ made by combustion synthesis. All of the peaks can be indexed in the *Pnmb* space group with no detectable impurity phases.

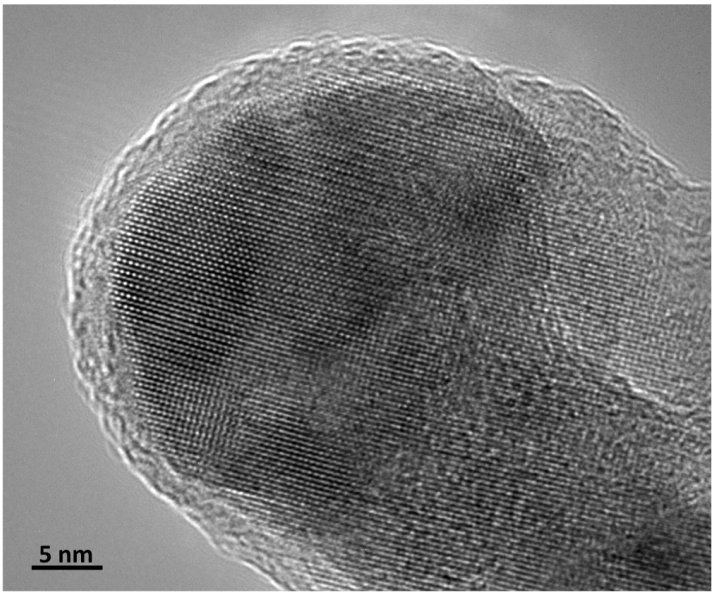

Figure 7.2: TEM image of $LiMnPO_4$ particle with continuous coating of amorphous carbon. Scale bar is 5 nm (Image courtesy of Jack Chen and Ruigang Wang, Lawrence Berkeley National Laboratory).

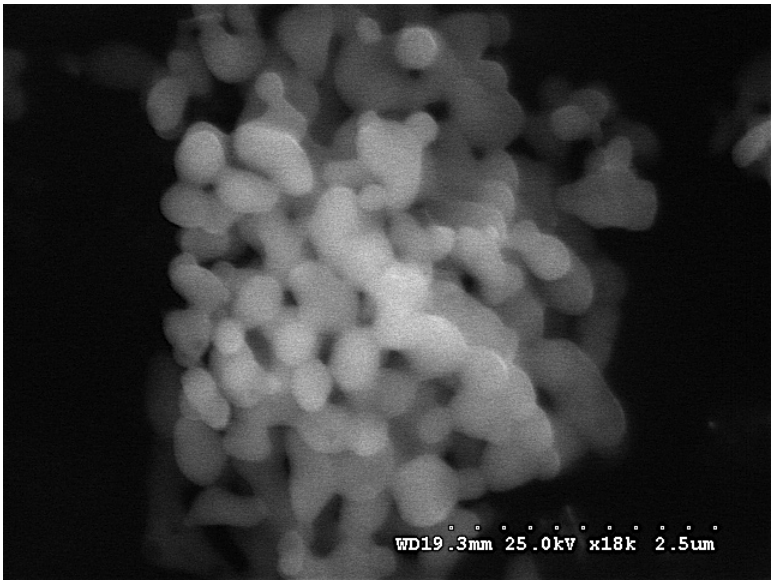

Figure 7.3: SEM image of $LiFePO_4$ powder made via the glycine nitrate combustion method. Secondary particles with a diameters in the range of 200-300 nm are comprised of ~30 nm primary particles.

carbon filaments and nanotubes (Figure 7.4) can often be observed in SEM micrographs in addition to the active material. The nanotubes are multi-walled and have an average diameter of approximately 20 nm. Dispersed throughout the nanotubes are nodules of iron or iron carbide, consistent with observations made on carbon coated nano materials formed by pyrolysis reported in the literature.[18] In hydrocarbon rich environments, iron particles can act as catalysts for the breakdown of volatile organic species. The carbon produced in the reaction diffuses into the iron particles and forms a supersaturated iron carbide phase, whereupon carbon filaments can be extruded to form various carbon morphologies.[19] Further TEM experiments have confirmed that the filaments are comprised of carbon from the analysis of the energy loss near edge structure (ELNES).

By adjusting the fuel to nitrate ratio in the solution, it is possible to tune the flame temperature to as high as 1350° C.[8] Because the carbon coating is formed during the combustion step, and not on the subsequent heat treatment at lower temperatures, carbon films with an improved graphitic character can be formed. Carbon contents appear to vary with the amount and type of fuel, as well as calcining conditions. The Raman

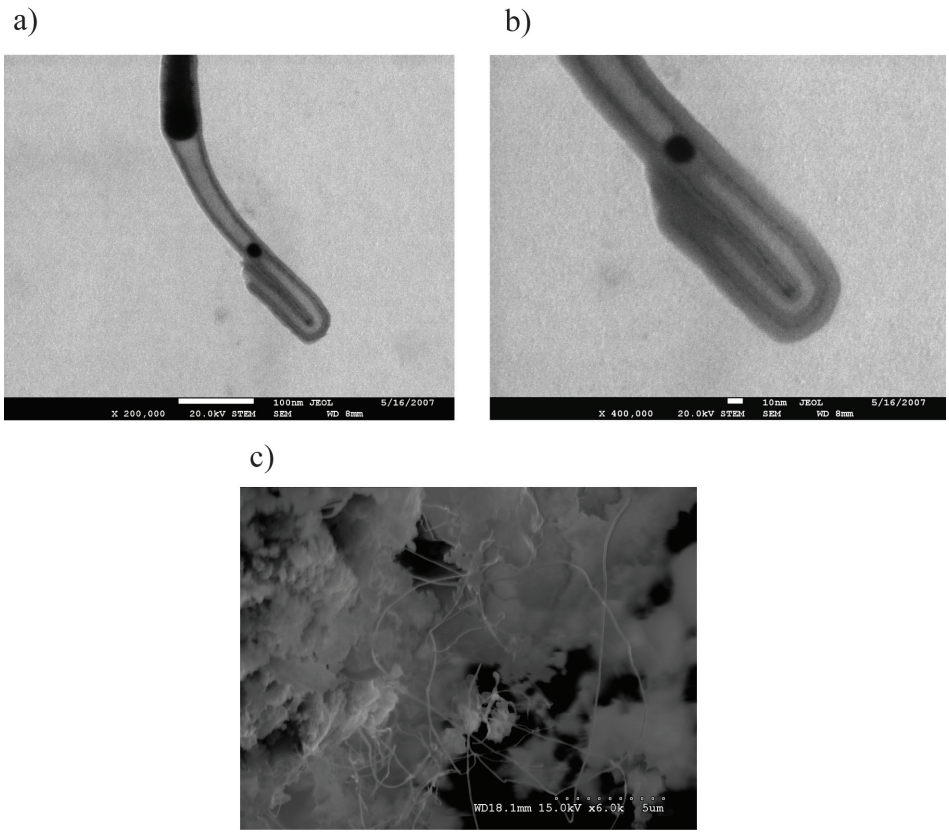

Figure 7.4: SEM images of carbon microstructures showing (a,b) multi-walled carbon nanotubes with iron carbide inclusions and (c) highly branched carbon fiber-like entities produced during the combustion reaction. TEM experiments using ELNES have determined that the carbon fibers are made up of amorphous carbon.

spectroscopic response of carbon coated particles formed by the catalytic decomposition of organics and combustion synthesis is presented in Figure 7.5. The D-band and the G-band of carbon at ~1350 cm^{-1} and ~1590 cm^{-1}, respectively, are present in the spectra of all of the materials. The PO_4 symmetric breathing mode of $LiFePO_4$ at 940 cm^{-1} can also be observed in the ferrocene and iron nitrate catalyzed samples. The Raman signal of carbon coatings formed by combustion (curve (c)) shows a significantly more resolved D and G band and a smaller relative D/G ratio as compared to materials produced via iron nitrate (curve (b)) and ferrocene (curve (a)) catalysts. As a first approximation, this is indicative of a carbon film with an improved graphitic nature, lower sp^3 carbon content,

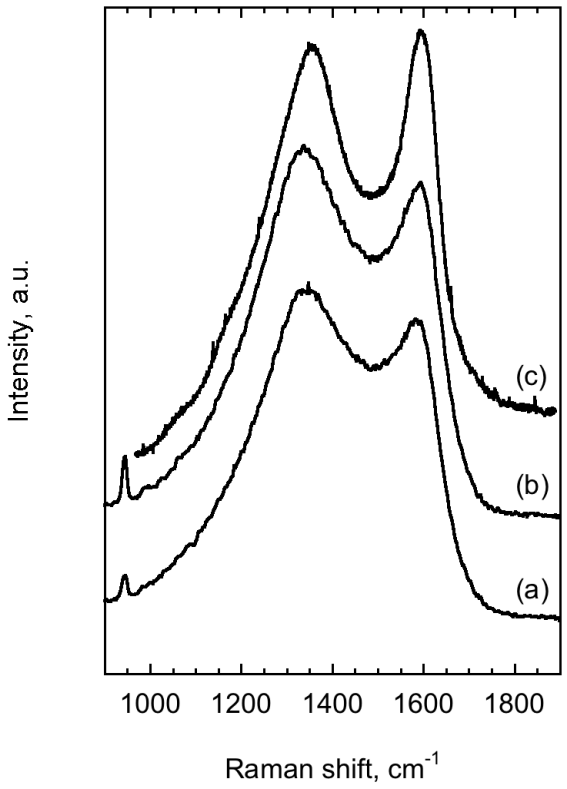

Figure 7.5: Raman spectra of $LiFePO_4$/C composite materials produced using (a) ferrocene catalysts, (b) iron nitrate catalysts, (c) and combustion. The material made by combustion shows a significantly improved carbon structure with an improved D/G ratio and decreased sp^3 carbon content.

and improved electronic conductivity (see Chapter 5). As all of these materials were heat treated to 600° C, the improvement in the structure reveals that the carbon coating was in fact formed during the initial high temperature combustion process.

Preliminary electrochemical rate studies on $LiFePO_4$/C composites made using the combustion process are presented in Figure 7.6. At low rates (C/25, curve (a)) the voltage plateau characteristic of the $LiFePO_4/FePO_4$ reaction can be observed at 3.45 V versus Li/Li^+. The discharge capacity decreases from 137 mAh/g at C/25 to 62 mAh/g upon increasing the discharge rate to 5C, indicating that there is significant room for improvement in the processing of these materials. The origin of the sloping potential profile at the end of discharge is also unknown at the present time. Possible mechanisms to explain this phenomenon include an increased single phase solubility of lithium due

to the small primary particle size or a widely dispersed, non-homogeneous particle size distribution.[20]

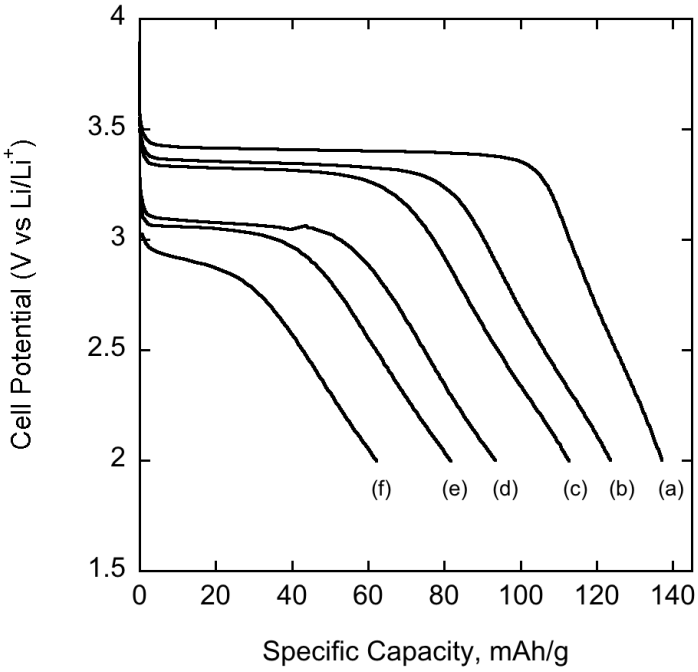

Figure 7.6: Discharge curves of Li/$LiFePO_4$ coin cells at (a) C/25, (b) C/5, (c) C/2, (d) C, (e) 3C, and (f) 5C rates. Cells were cycled between 2.0 and 3.9 V and all charge cycles were performed at C/25 independent of discharge rate. The sloping profile at the end of discharge may be related to the reduced particle size of materials produced using the combustion method.

7.5 Conclusions

These results indicate that combustion based synthetic techniques can be applied to create olivine/carbon composite materials. This novel synthetic route has the advantage of forming very small primary particles coated with a high quality carbon coating. By virtue of the fast kinetics of the combustion process, the thermal limitation of $LiFePO_4$ can be overcome, allowing the formation of coatings with a graphitic quality typical of carbons formed at temperature well above the normal sintering temperatures of $LiFePO_4$. The concurrent synthesis of carbon structures, such as fibers and nanotubes, may allow for the formation of high performance electrodes with minimal carbon contents. Initial

electrochemical results indicate, that with further optimization and careful experimental control, a high rate material can be synthesized using these techniques. Furthermore, the combustion method can be extended to synthesize other olivine transition metal phosphates such as $LiMnPO_4$, $LiNiPO_4$, and $LiCoPO_4$ or even lithium transition metal silicates such as $LiFeSiO_2$ and Li_2FeSiO_4 in rapid fashion with minimum waste and heat treatment.[21, 22]

7.6 Acknowledgments

The authors would like to thank Rong Yu for his expertise in the TEM analysis of the combusted materials and Jack Chen and Ruigang Wang for the image of the carbon coated $LiMnPO_4$ particle. JEOL of Pleasanton, Inc. provided images of nanotubes found in some of the combusted samples. The authors would also like to thank Robert Kostecki and Marek Marcinek for the Raman analysis of the carbon coatings and their useful discussions on the diagnostics of carbon films.

7.7 References

1. Herle, P.S., et al., *Nano-network electronic conduction in iron and nickel olivine phosphates.* Nat Mater, 2004. **3**(3): p. 147-152.

2. Chung, S.-Y., J.T. Bloking, and Y.-M. Chiang, *Electronically conductive phospho-olivines as lithium storage electrodes.* Nat Mater, 2002. **1**(2): p. 123-128.

3. Kang, H.C., et al., *Optimized solid-state synthesis of LiFePO(4) cathode materials using ball-milling.* Journal of Power Sources, 2008. **179**(1): p. 340-346.

4. Kinoshita, K., *Carbon : electrochemical and physicochemical properties*. 1988, New York: Wiley.

5. Stacy, W.O., G.R. Imperial, and P.L. Walker, *Chlorine fixation on anthracites and carbon blacks and its effect on electrical resistivity.* Carbon, 1966. **4**(3): p. 343.

6. Franco, A., et al., *Synthesis of nanoparticles of Co(x)Fe(3-x)O(4) by combustion reaction method.* Journal of Magnetism and Magnetic Materials, 2007. **308**(2): p. 198-202.

7. Jain, S.R., K.C. Adiga, and V.R. Pai Verneker, *A new approach to thermochemical calculations of condensed fuel-oxidizer mixtures.* Combustion and Flame, 1981. **40**: p. 71-79.

8. Chick, L.A., et al., *Glycine-nitrate combustion synthesis of oxide ceramic powders.* Materials Letters, 1990. **10**(1-2): p. 6-12.

9. Abraham, D.P., S. Kawauchi, and D.W. Dees, *Modeling the impedance versus voltage characteristics of LiNi(0.8)Co(0.15)Al(0.05)O(2).* Electrochimica Acta, 2008. **53**(5): p. 2121-2129.

10. Kumar, H.P., et al., *Characterization and sintering of BaZrO(3) nanoparticles synthesized through a single-step combustion process.* Journal of Alloys and Compounds, 2008. **458**(1-2): p. 528-531.

11. Whittingham, M.S., et al., *Some transition metal (oxy)phosphates and vanadium oxides for lithium batteries.* Journal of Materials Chemistry, 2005. **15**(33): p. 3362-3379.

12. Prosini, P.P., et al., *Determination of the chemical diffusion coefficient of lithium in LiFePO(4).* Solid State Ionics, 2002. **148**(1-2): p. 45-51.

13. Delacourt, C., et al., *Toward Understanding of Electrical Limitations (Electronic, Ionic) in LiMPO(4) (M = Fe, Mn) Electrode Materials.* Journal of The Electrochemical Society, 2005. **152**(5): p. A913-A921.

14. Thorat, I.V., et al., *Performance of carbon-fiber-containing LiFePO(4) cathodes for high-power applications.* Journal of Power Sources, 2006. **162**(1): p. 673-678.

15. Ahn, S., *High Capacity, High Rate Lithium-Ion Battery Electrodes Utilizing Fibrous Conductive Additives.* Electrochemical and Solid-State Letters, 1998. **1**(3): p. 111-113.

16. Wang, C.W., K.A. Cook, and A.M. Sastry, *Conduction in Multiphase Particulate/ Fibrous Networks.* Journal of the Electrochemical Society, 2003. **150**(3): p. A385-A397.

17. Lin, Q. and J.N. Harb, *Implementation of a Thick-Film Composite Li-Ion Microcathode Using Carbon Nanotubes as the Conductive Filler.* Journal of the Electrochemical Society, 2004. **151**(8): p. A1115-A1119.

18. Panchakarla, L.S. and A. Govindaraj, *Carbon nanostructures and graphite-coated metal nanostructures obtained by pyrolysis of ruthenocene and ruthenocene-ferrocene mixtures.* Bull. Mater. Sci., 2007. **30**(1): p. 23-29.

19. Mauron, P., et al., *Synthesis of oriented nanotube films by chemical vapor deposition.* Carbon, 2002. **40**(8): p. 1339-1344.

20. Meethong, N., et al. *Size-dependent lithium miscibility gap in nanoscale Li(1-x) FePO(4)*. 2007: Electrochemical Soc Inc.

21. Zhou, F., et al., *The Li intercalation potential of LiMPO(4) and LiMSiO(4) olivines with M = Fe, Mn, Co, Ni.* Electrochemistry Communications, 2004. **6**(11): p. 1144-1148.

22. Dominko, R., et al., *Structure and electrochemical performance of Li(2)MnSiO(4) and Li(2)FeSiO(4) as potential Li-battery cathode materials.* Electrochemistry Communications, 2006. **8**(2): p. 217-222.

8. Future Work

8.1 Layered Transition Metal Oxides

While it is clear that substitution of cobalt with aluminum can create high-rate, low cost positive materials, numerous questions persist as to the mechanism of the improvement. To this end, several new experiments and collaborations are either on-going or in the process of being established. In conjunction with the background provided in this dissertation, these experiments are expected to yield insight into the effect of aluminum (or aluminum-like) substitution on the structural and electrochemical behavior of complex layered transition metal oxides.

The primary question that remains to be addressed is the refinement of the structural model based on the combined neutron and X-ray diffraction results. As discussed in Chapter 4, there is an almost linear degradation in the Bragg factor (R_B) with increasing aluminum content (y). Assuming a well behaved background function and stable diffraction conditions, this indicates that the assumed structural model, that of a solid solution distribution of cations within the transition metal plane, may not accurately reflect the experimentally observed data. To address this issue, a collaboration with Los Alamos National Laboratory/University of California, Santa Barbara has been established to explore more detailed structural models. The potential model variations include local cation clustering, variable aluminum coordination, and strain effects resulting from the mixing of ions with disparate ionic radii. This collaboration is intended to also conduct pair distribution function (PDF) analysis on data that was simultaneously collected during the neutron diffraction experiments. When combined with reverse Monte Carlo simulations, PDF analysis allows for the mapping of elemental species as a function of coordination sphere in the transition metal plane. This analysis will, therefore, aid in the creation of a more refined structural model for the analysis of the diffraction data.[1]

The magnetic response of layered transition metal oxides has long been used to study

the local cation arrangements and anti-site mixing.[2] Due to strong 180° antiferromagnetic coupling between transition metal layers in the presence of a Ni^{2+} anti-site defect, the magnetization and magnetic susceptibility are highly sensitive to the amount of nickel residing in the lithium plane.[3] Recently, Ma *et al.* have studied the magnetic behavior of $LiNi_{0.4}Co_{0.2}Mn_{0.4}O_2$ and found a pronounced hysteresis consistent with the mixing of nickel between the *3a* and *3b* sites.[4] This method could easily be extended to the $LiNi_zCo_{0.2-y-2z}Al_yMn_zO_2$ material system. It should be noted that this technique is not quantitative at the present time, though it can yield information about the relative increase or decrease in anti-site mixing upon substitution.

Another area that needs to be addressed is the increased polarization at high states of charge in aluminum-substituted materials (Figure 4.13). Working with Profesor Elton Cairns (Chemical Engineering, University of California Berkeley) and Aniruddha Deb (Assistant Research Scientist, University of Michigan) *in-situ* X-ray Adsorption Near-Edge Spectroscopy (XANES) and Extended X-ray Adsorption Fine Structure (EXAFS) experiments have recently been conducted at Argonne National Laboratory on $LiNi_{0.4}Co_{0.15}Al_{0.05}Mn_{0.4}O_2$ materials. The analysis of the XANES spectra taken as a function of lithium content will allow for the determination of the electrochemically active species at various states of charge. Additionally, the local environment of the X-ray absorbing atom can be probed using EXAFS, yielding information about the characteristic radial coordination as a function of distance.[5, 6] In EXAFS the distance over which the coordination sphere can be examined is limited compared to PDF analysis. However, the ability to collect data at various states of charge is of tremendous advantage. If the source of increased polarization is the migration of a metal ion (presumably either aluminum or nickel) to either the lithium plane or an intermediate tetrahedral site at low lithium contents, it should be detectable by EXAFS analysis. To further examine the potential for structural reorganization at high states of charge, a joint project at the SLAC National Accelerator Laboratory is being pursued with Michael Toney for high resolution XRD as

a function of state of charge.

If a superstructural cation arrangement can be derived for the atoms residing in the transition metal plane, it may become possible to pursue the modeling of the lithium transport process using *ab initio* methods. The diffusion pathway in materials crystallizing in the α-$NaFeO_2$ structure has been well established using density functional theory.[7] However, the activation energy as a function of local metal coordination in highly substituted layered oxides has not been explored to the author's knowledge. The identification of potential low energy diffusion pathways in the vicinity of specific local environments may allow for the design and optimization of future cathode materials. First principle modeling of materials at low lithium content can also yield insights into the structural stability of $Li_xNi_zCo_{1-y-2z}Al_yMn_zO_2$ and any shifts in electronic properties during cycling.

Finally, to overcome the apparent noise in the GITT analysis presented in Chapter 4, the production of dense, thin film electrodes is being pursued. In principle, thin film electrodes can exhibit a more uniform reaction distribution provided the current densities are maintained at a low enough level. This will improve the stability of the potential signal as a function of time and allow for more accurate measurements of the chemical diffusion coefficient. [8]

8.2 Transition Metal Phosphates

Future work concerning the transition metal phosphates will focus on defining and controlling the experimental parameters required for the formation of optimized powders by combustion methods. The identification of the proper fuel, fuel to oxidizer ratio, phosphate source, and heat treatment parameters is required to make a material with adequate electrochemical properties. The characterization of the carbon coating, as a function of carbon source and processing conditions, will also be of utmost importance in making high rate materials.

Preliminary results indicate that the combustion method can be extended to the synthesis of transition metal phosphates based on cobalt, nickel, and manganese. The production of powders with small particle dimensions may prove vital to the operation of such materials as they also exhibit extremely poor transport properties. The combustion method may also allow for the synthesis of materials with an intimate mixture of metals on the M2 site. For example, the substitution of even small amounts of magnesium has been shown to improve the cycling behavior of $LiMnPO_4$, increasing the reaction kinetics and stabilizing the delithiated phase with respect to hydration.[9]

8.4 References

1. Breger, J., et al., *NMR, PDF and RMC study of the positive electrode material LiNi(0.5) Mn(0.5)O(2) synthesized by ion-exchange methods.* Journal of Materials Chemistry, 2007. **17**(30): p. 3167-3174.

2. Rougier, A., C. Delmas, and G. Chouteau, *Magnetism of Li(1-z)Ni(1+z)O(2): A powerful tool for structure determination.* Journal of Physics and Chemistry of Solids, 1996. **57**(6-8): p. 1101-1103.

3. Chernova, N.A., et al., *Layered Li(x)Ni(y)Mn(y)Co(1-2y)O(2) Cathodes for Lithium Ion Batteries: Understanding Local Structure via Magnetic Properties.* Chem. Mater., 2007. **19**(19): p. 4682-4693.

4. Ma, M., et al., *Structural and electrochemical behavior of LiMn(0.4)Ni(0.4)Co(0.2) O(2).* Journal of Power Sources, 2007. **165**(2): p. 517-534.

5. Tsai, Y.W., et al., *In-situ X-ray absorption spectroscopic study on variation of electronic transitions and local structure of LiNi(1/3)Co(1/3)Mn(1/3)O(2) cathode material during electrochemical cycling.* Chemistry of Materials, 2005. **17**(12): p. 3191-3199.

6. Deb, A., et al., *In situ X-ray absorption spectroscopic study of Li(1.05)Ni(0.35) Co(0.25)Mn(0.4)O(2) cathode material coated with LiCoO(2).* Journal of the Electrochemical Society, 2007. **154**(6): p. A534-A541.

7. Kang, K. and G. Ceder, *Factors that affect Li mobility in layered lithium transition metal oxides.* Physical Review B (Condensed Matter and Materials Physics), 2006. **74**(9): p. 094105-7.

8. Wen, C.J., et al., *Thermodynamic and Mass Transport Properties of ``LiAl''.* Journal of The Electrochemical Society, 1979. **126**(12): p. 2258-2266.

9. Chen, G.Y., J.D. Wilcox, and T.J. Richardson, *Improving the performance of lithium manganese phosphate through divalent cation substitution.* Electrochemical and Solid State Letters, 2008. **11**(11): p. A190-A194.